RESISTIVE MHD SIMULATIONS OF LAMINAR ROUND JETS WITH APPLICATION TO MAGNETIC NOZZLE FLOWS

A Thesis

by

DANIEL BORSODI ARAYA

Submitted to the Office of Graduate Studies of
Texas A&M University
in partial fulfillment of the requirements for the degree of

MASTER OF SCIENCE

December 2011

Major Subject: Aerospace Engineering

RESISTIVE MHD SIMULATIONS OF LAMINAR ROUND JETS WITH APPLICATION TO MAGNETIC NOZZLE FLOWS

A Thesis

by

DANIEL BORSODI ARAYA

Submitted to the Office of Graduate Studies of
Texas A&M University
in partial fulfillment of the requirements for the degree of

MASTER OF SCIENCE

Approved by:

Chair of Committee,	Sharath Girimaji
Committee Members,	David Staack
	John Shebalin
	Alfonso Tarditi
	Jacques Richard
Head of Department,	Dimitris Lagoudas

December 2011

Major Subject: Aerospace Engineering

ABSTRACT

Resistive MHD Simulations of Laminar Round Jets with Application to Magnetic Nozzle Flows. (December 2011)

Daniel Borsodi Araya, B.S. Texas A&M University

Chair of Advisory Committee: Dr. Sharath Girimaji

This thesis investigates fundamental flows of resistive magnetohydrodynamics (MHD) by a new numerical tool based on the gas-kinetic method. The motivation for this work stems from the need to analyze the mechanisms of plasma detachment in the exhaust plume of the magnetoplasma rocket known as VASIMR®. This rocket has great potential for reducing the travel time for deep space exploration missions. However, it is very difficult to investigate detachment in ground-based experiments because this large-scale device can fully function only in a vacuum. This difficulty makes computational analysis and modeling an important part of the design and testing process. A parallelized Boltzmann-BGK continuum flow solver is expanded to include resistive MHD physics. This new code is validated against known solutions to MHD channel flows and new results are presented for simulations of a laminar round jet subject to a constant applied magnetic field as well as the diverging magnetic field of a current loop. Additionally, a parametric map is presented that outlines appropriate conditions required when using a fluid model for magnetic nozzle flows. The work of this thesis serves as an introductory step to developing a robust numerical flow solver capable of simulating magnetic nozzle flows and other plasmas that cannot be easily replicated in ground facilities.

To my parents.

Thanks for sacrificing so much to get me started off right in life.

ACKNOWLEDGMENTS

I would like to thank my advisor, Dr. Sharath Girimaji, for taking me to be his student when I was faced with a difficult decision two years ago. I admire his ability to balance having a wonderful family with his esteemed research contributions, and I appreciate him making me feel like I have good ideas sometimes.

I would also like to thank my other committee members for their support. I thank Dr. John Shebalin for access to his encyclopedic knowledge of plasma physics and for pointing me to so many good reference texts. I'm very grateful to Dr. Alfonso Tarditi for dedicating so many hours of his time to meet with me and to troubleshoot with me when I had problems. I also thank Drs. David Staack and Jacques Richard for their useful comments that made this manuscript much better than it was when I first wrote it.

This work would also not have been possible without the people of the Ad Astra Rocket Company. I am especially thankful to Dr. Franklin Chang-Diaz for supporting my interest in space propulsion from the start and for encouraging me to join NASA's co-op program. I would also like to thank Drs. Mark Carter and Andrew Ilin for their many insightful technical suggestions and also to Chris Olsen for his hard work to post-process all of the VX-200 raw data.

I also feel very lucky to have had such a great group of fellow grad students to work with. I'd like to thank Jacob Cooper, my officemate from the beginning, for being good company and being patient with me, especially with the lights. Maybe it was annoying to be in half darkness all the time, but he never showed it. I'd also like to thank Zhimin Xie for taking me fishing and for checking my math in the conference paper when nobody else would. A big thanks also goes to Frans Ebersohn for checking the math in Chapter IV, and for catching that pesky energy problem.

I'm also indebted to Gaurav Kumar for solving the symmetry problem, and for his all-around genius suggestions. I also thank him for the many thoughtful discussions, and for the bottomless drawer full of snacks.

I would also like to thank Karen Knabe and Colleen Leathermann for all of their administrative wisdom and impeccable efficiency. I'm convinced that they are the real people that run the Aerospace Engineering Department. I also thank Dr. William Saric for suggesting Caltech to me and for giving me the best bang for my buck by his lectures at Texas A&M. Also thanks goes to Dr. Ruth Schemmer for her careful editing of this manuscript on such short notice.

Finally, and above all, I am most thankful to my beautiful wife, Carolina. Without her, my life would be permanently underdamped. I am grateful for her wisdom, for her planning, and especially for her sharing the trials of grad school with me.

TABLE OF CONTENTS

CHAPTER Page

LIST OF TABLES

LIST OF FIGURES

FIGURE Page

FIGURE Page

FIGURE Page

CHAPTER I

INTRODUCTION

A. Challenges for Space Exploration

The idea of humans traveling deep into space beyond the Earth and moon is not new. Far from novel, this idea has inspired decades of science fiction and science in earnest to advance our understanding of the universe in which we live. With exploring a new environment always comes new and sometimes unexpected challenges. During NASA's manned Apollo missions, the journey to the moon took about 3 days. Using today's conventional chemical rockets, a manned mission to Mars could take about 9 months for a one-way trip. For this kind of extended mission, there is real concern about astronaut health; reducing the travel time is essential. Reaching further than Mars is presently unthinkable for manned missions and even robotic missions are restricted by the vast distances to other bodies in our solar system. For example, NASA's New Horizons probe will take about 10 years to reach its target of Pluto in 2015. Reducing travel time is critical for continuing to explore deeper into space, especially for future manned missions. To achieve this goal, it is clear that there must be significant advances in space propulsion technology.

Plasma propulsion systems that harness electromagnetic energy are a promising alternative to chemical systems. This point is made clear in the simplified rocket equation given by Jahn [1], which is the following:

$$\frac{m_f}{m_0} = e^{-\triangle v/u_e} \tag{1.1}$$

The journal model is *IEEE Transactions on Automatic Control.*

where m_f is the final mass of the rocket, m_0 is the initial mass, $\triangle v$ is the magnitude of the velocity achieved impulsively, and u_e is the exhaust velocity. This equation shows that an exponential increase in mass is required for more distant missions (i.e. higher required $\triangle v$). However, a linear increase in exhaust velocity can result in an exponential decrease in initial required mass, which is illustrated in Figure 1.

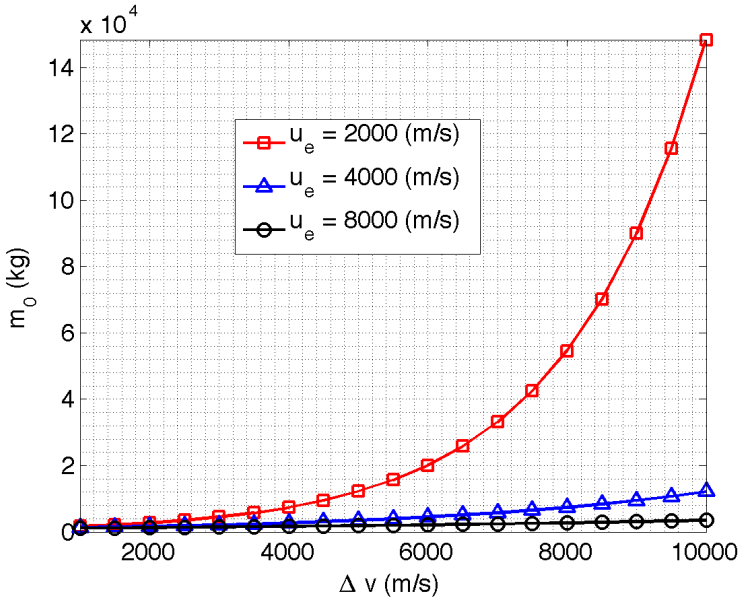

Fig. 1. Variation of m_0 for different $\triangle v$ and u_e.

Chemical propulsion systems are limited in the exhaust velocity they can achieve, but electric propulsion devices are not. A typical range of exhaust velocities are shown in Figure 2 for a variety of different propulsion systems. Typically, this exhaust velocity performance is given as the specific impulse, defined as $I = u_e/g_0$, where g_0 is the acceleration due to gravity at sea level. Solid rockets and liquid propellant engines have relatively low specific impulse, low engine weight, and very high thrust, making them best suited for takeoff, landing and escaping Earth's gravitational field. Conversely, electric propulsion (EP) devices can achieve very high specific impulse,

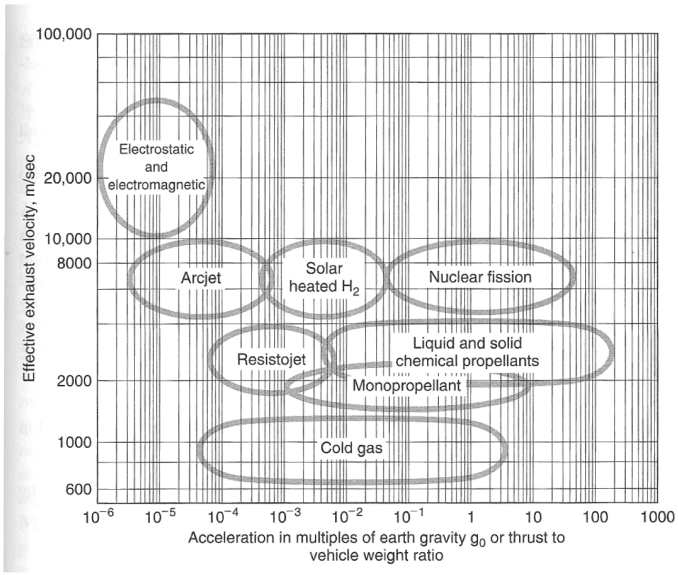

Fig. 2. Typical exhaust velocities for chemical and electric propulsion systems [2].

produce low thrust, and typically have heavy electrical power sources. This makes EP devices unsuitable for takeoff and landing, but ideally suited for interplanetary space flight missions [2].

As EP devices for in-space propulsion can fully function only in a vacuum, it is very difficult to test large scale devices in ground-based experiments. This difficulty makes computational analysis and modeling an important part of the design development and testing process. The motivation for this work stems from the need to analyze the mechanisms of plasma detachment in the exhaust plume of a magneto-plasma rocket called VASIMR® [3]. The VASIMR® concept dates back to the early 1980's and several references detail its design progression over the years [4, 3, 5, 6]. The major components of VASIMR® are shown in Figure 3, with the magnetic nozzle section being of particular interest in this thesis.

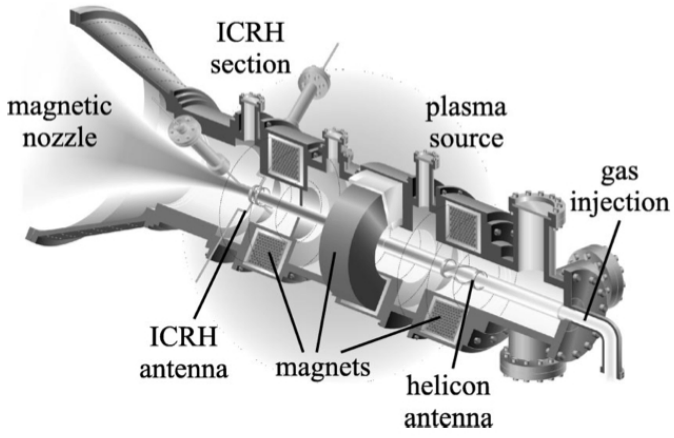

Fig. 3. VASIMR® schematic. [3]

B. Magnetic Nozzle Detachment

The magnetic nozzle harnesses ion thermal energy (TE) by converting it into directed ion kinetic energy (KE) via electromagnetic forces. In many respects, the magnetic nozzle is analogous to the conventional de Laval nozzle [2] in which potential (internal) energy is converted into directed KE, resulting in thrust. An important distinction in the magnetic nozzle, however, is the presence of magnetic field lines encompassing the propulsion device as illustrated in Figure 4. This magnetic field directs the azimuthal TE of the ions into axial KE. In order to produce net thrust, the plasma bearing the axial KE must detach from the propulsion device. However, the same magnetic field that directs the energy also has the detrimental effect of inhibiting the detachment of the exiting plasma flow. Furthermore, the detachment process itself may interrupt the conversion of TE into directed KE, which may further inhibit the effectiveness of the magnetic nozzle. If one considers detachment with regards to rarefied single magnetized particle motions, the conversion of TE to KE is interrupted by necessity of the particles becoming demagnetized. If, instead, one considers fluid mechanical type

detachment, the conversion of TE to KE is also interrupted, but the understanding of this process is not clear. Inherently, there is a tradeoff between the conversion of TE to KE and the detachment of the flow, but addressing this in a real system is not simple, which necessitates the development of modeling tools.

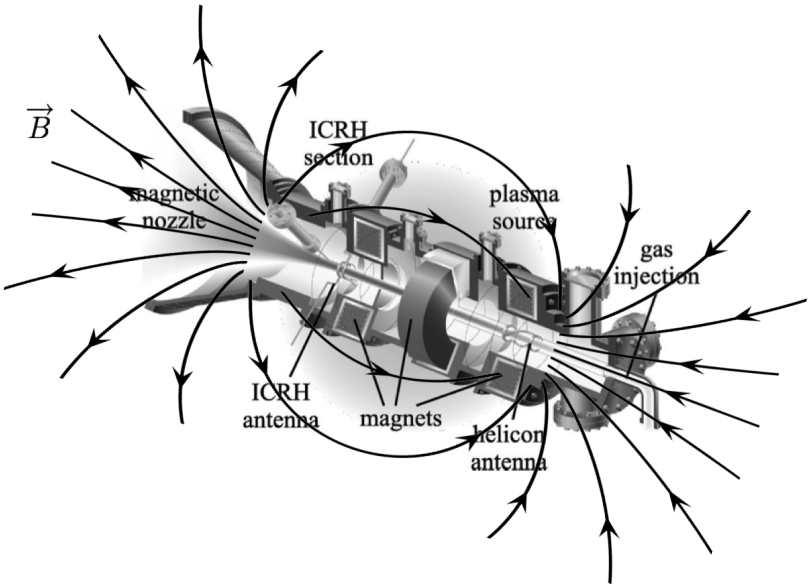

Fig. 4. VASIMR® schematic [3] with sketched (not to scale) magnetic field lines.

Several authors have contributed to investigating the physics of plasma detachment analytically [7, 8, 9, 10, 11], computationally, [12, 13, 14, 15, 16] and experimentally [17, 18, 19, 20]. However, few studies have looked at computational simulations of detachment within the scope of a fluid or magnetohydrodynamics (MHD) approach. Furthermore, only two published works at this present writing have made efforts in MHD simulations of detachment specifically for the VASIMR® configuration. Breizman and Arefiev[16] showed that even within the limits of a perfectly conducting plasma, an essential assumption of ideal MHD, a sufficiently energetic plasma can detach. Under their assumptions, the sufficient condition for detachment to occur is

when $\beta > 1$, where β is the ratio of fluid to magnetic pressure. This condition can also be interpreted to mean that the plasma detaches when it transitions from sub to super-Alfvénic flow. Tarditi et al. [15] began to investigate detachment in the VASIMR® plume with the non-ideal MHD code NIMROD [21]. They investigated the possibility of early detachment, closer to the exit of the rocket, prior to the attainment of $\beta > 1$ condition. The authors suggest that plasma resistivity and other non-ideal effects could cause early detachment, which may or may not be beneficial to the overall performance of the magnetic nozzle.

It is postulated that detachment could occur in a manner similar to a solar flare during which magnetic field lines reconnect and ionized particles are ejected from the sun into outer space. This reconnection is due to plasma currents aligning in such a way as to form a separatrix with the background magnetic field, which creates a natural boundary between attached and detached exiting plasma. If reconnection is observed in the VASIMR® plume, it would possibly be observed as a shedding of "plasmoids" caused by rapid fluctuations in the magnetic field, and is still under investigation. Properly understanding plasma detachment is important for an EP application because it directly influences thrust efficiency and it also affects plume-spacecraft interaction. The challenge is to develop a predictive tool that captures enough physics to study the uncertain phenomenon, yet remains computationally tractable.

C. Kinetic Theory-Based MHD Simulations

In order to simulate the plasma of interest numerically, a robust computational tool is necessary. One of the available tools for this work is a direct numerical solver of the three-dimensional compressible Navier-Stokes equations called the Gas-Kinetic

Method (GKM) code. This tool is a finite volume numerical scheme that is a hybrid of fluid and kinetic methods. It is different from other Navier-Stokes schemes in that it calculates fluxes from single-point particle distribution functions rather than from any constitutive relation. The scheme was originally devised by K. Xu for shock capturing in high Mach number flows [22] but has since been shown to be very effective even at weakly compressible limits [23]. It is currently being used for Direct Numerical Simulations (DNS) of compressible turbulence with High Performance Computing (HPC) resources at Texas A&M University. A more detailed description of how the numerical scheme works is given by Xu [22] and partly summarized in Chapter IV.

Recently, the gas-kinetic method has been extended to successfully solve the three-dimensional ideal MHD equations [24]. However, this scheme is based on earlier work by Xu, who notes that "different from the BGK scheme for the Euler and Navier-Stokes equations, there is no direct way to extend the [Gas-kinetic flux splitting method for ideal MHD] to solve dissipative MHD equations (including resistivity and dispersive effects) due to the lack of microscopic transport equations [25]." Xu then goes on to suggest that "the dissipative terms can be regarded as additional source terms" in the equations. In recent years, other gas-kinetic resistive MHD simulations have been published by the Texas A&M research group [26, 27] using a Lattice Boltzmann Method (LBM). However, the LBM is restricted to incompressible flows and the magnetic nozzle flows of interest will require a compressible scheme. Thus far, no work has been published extending the gas-kinetic method proposed by Xu to solve non-ideal MHD equations. It is worth noting, though, that a recent preprint by Tian [28] does attempt to extend the gas-kinetic method for resistive magnetic flows, but by a different method than the one proposed in this thesis.

The gas-kinetic method has also been shown to be viable for the problem of expanding a gas into a vacuum [29], which is an essential part of realistic in-space

magnetic nozzle simulations. For the problem of expanding a plasma into a vacuum, the plasma density tends toward zero very rapidly and traditional CFD methods are known to fail. An MHD simulation of this rapid expansion may lead to numerical instability, which Shebalin has shown can be avoided by the use of a natural logarithm formulation of the governing equations [30]. Physically, however, one potential drawback in using a standard MHD model for simulating this type of plasma flow is the assumption of a continuum, which could break down if the density decreases too quickly. The gas-kinetic method proposed by Xu for multicomponent flow is an effective alternative scheme for this type of problem as it has been shown to be robust in handling the rapid transition to a rarefied regime for a neutral gas [29]. The current version of the Texas A&M University GKM code supports only single-component flow, but work is under way to expand the code to have multicomponent flow capability.

D. Research Contributions

This thesis serves as the introductory component to a multi-year goal to develop a robust tool for simulating magnetic nozzle flows. This high-fidelity numerical tool will aid in the exploration of physics in flow conditions that cannot be easily replicated in ground facilities, including detachment. A direct contribution of this research to magnetic nozzle flows is to provide a parametric map that outlines appropriate conditions required when using a fluid model for nozzle simulations.

Another contribution of this research is to expand the current single-component GKM code to incorporate resistive MHD effects. This work follows a form similar to the work of Fuchs et al. [31], where the ideal MHD equations were split into a hydrodynamic part and a magnetic induction part and solved by different numerical

schemes. Similarly, the approach of this thesis is to modify the GKM continuum flow solver by adding magnetic source terms as well as an evolution equation for the magnetic field using central-differences. This splitting technique is flexible enough to incorporate other numerical methods for solving the magnetic terms and can be expanded to include the Hall effect or an even higher fidelity"two-fluid" model later.

Understanding the physics of a plasma moving through a static background magnetic field is not limited to space propulsion applications. There is great interest in magnetized plasmas for studying astrophysical flows, such as solar wind impinging on the Earth's magnetosphere, fusion reactor technology, liquid metal processing, and microfabrication to name a few. Therefore, another contribution of this work is to test the GKM-MHD code for fundamental resistive MHD channel flows. These flows have known analytical solutions and serve as a benchmark of the code for 2-D, weakly-compressible flow simulations.

Finally, simulations of laminar round jets subject to two different applied magnetic field geometries complete the contributions of this thesis. Theoretical work by Davidson [32] for low magnetic Reynolds number MHD jets serves as a benchmark for the round jet simulations subject to a constant applied field. Then, new results are shown for a round jet subject to an applied field generated by a current loop. These MHD jet simulations are unique and the simple geometry allows insight into the nature of three-dimensional MHD physics.

E. Thesis Organization

The remainder of this thesis is organized as follows. Chapter II gives some background on the physics of modeling a plasma, including discussions of particle, kinetic, and fluid methods. Chapter III follows a technique for parameterizing MHD flow physics

to analyze the magnetic nozzle flow characteristics of the current VASIMR® VX-200 rocket. Chapter IV gives the details of the numerical scheme used in the Texas A&M GKM code, as well as changes to the code for resistive MHD flow simulations. Chapter V examines MHD channel flows and compares analytical solutions with the new GKM-MHD numerical results. Chapter VI presents results for 3-D MHD jet simulations with a constant applied magnetic field and also for an applied field generated by a current loop. Finally, Chapter VII summarizes the conclusions from this work and presents a discussion of potential future work.

CHAPTER II

METHODS FOR PLASMA MODELING

An often quoted statistic is that plasmas make up approximately 99% of the matter in the visible universe. This number may seem high, but the ubiquitous nature of plasmas can be attributed to the enormous range of density and temperature scales in which they exist, with only a relatively few examples found in everyday life on Earth. An example of this range is shown in Figure 5. For comparison, room temperature (300 K) air has a density of about 2.5×10^{25} $particles/m^3$ and, as shown in Chapter III, the current VASIMR® VX-200 rocket plume has a density of approximately $10^{16} - 10^{19}$ $particles/m^3$ and an ion temperature of about $10^5 - 10^6$ K.

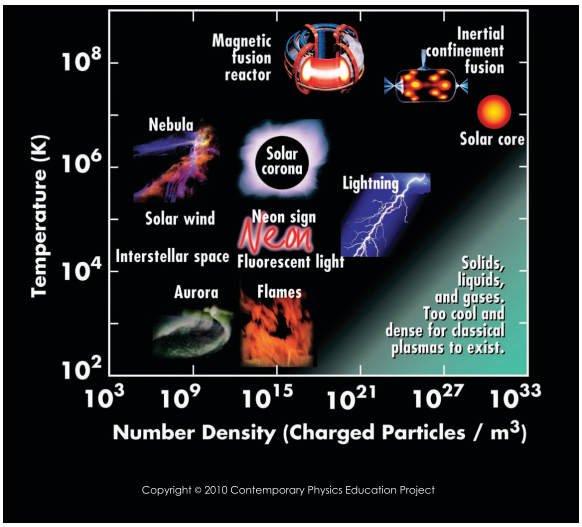

Fig. 5. Range of scales for plasmas ($http://FusEdWeb.llnl.gov/CPEP/$).

This wide range of scales makes for an interesting challenge when trying to model the dynamics of a plasma with a numerical simulation on a computer. One key benefit is that all plasmas obey the same fundamental governing equations; therefore, they share common behaviors. However, the major difficulty that arises for simulations of

plasmas is the extreme stiffness of the equations, as explained later in this chapter.

A. Plasma Parameters

Plasmas are sometimes called the "4th state of matter" because they can be formed by adding a substantial amount of energy to relatively cool gases. However, to be precise, they are not simply ionized gases. The more strict definition, as given by Chen, is that "*a plasma is a quasineutral gas of charged particles which exhibits collective behavior*" [33]. A neutral gas can be thought of in two ways: one, as composed of only charge neutral molecules, or two, as having an exact balance of charged particles (e.g. $n_e = n_i$) such that no net electromagnetic force can be exerted on it. A plasma is said to be a quasineutral gas because it is assumed to be neutral enough to say that $n_e \approx n_i \approx n$, where n is called the plasma density, but not so neutral that all the net electromagnetic forces may be neglected. In addition to the particle collisions that are dominant in neutral gases, plasmas have local electric and magnetic fields created by the motion of the charged particles, as illustrated in Figure 6. "Collective behavior" of plasmas means that the motion of the particles depends on both local collisions and long range electromagnetic interactions.

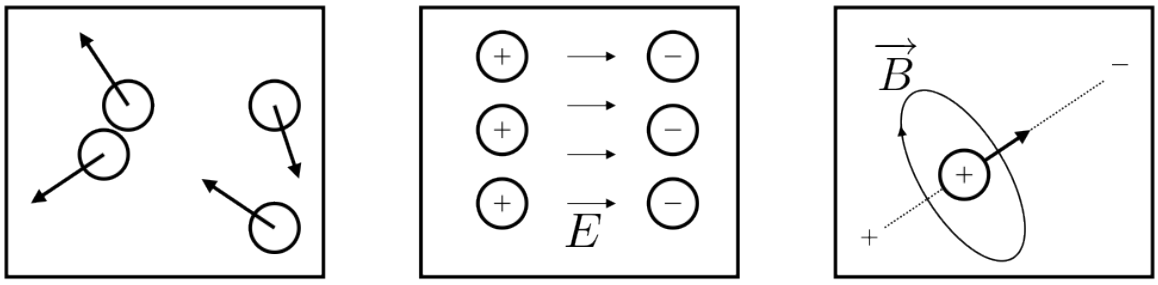

(a) (b) (c)

Fig. 6. Neutral collisions (a), local electric field (b), local magnetic field (c).

Temperature is another important concept when discussing plasmas. A gas in thermal equilibrium has particles of all velocities. The most probable distribution of these velocities is called the Maxwellian velocity distribution, which is illustrated in Figure 7. Temperature is characterized by the width of a Maxwellian distribution. The wider the distribution, the more high speed particles are present, and the higher the gas's temperature is. The convention in plasma physics is to denote the temperature of a plasma by the energy corresponding to K_BT (where K_B is Boltzmann's constant, and T is temperature), which is related to the average kinetic energy of the plasma particles. A useful temperature conversion factor is $1eV \approx 11,600K$.

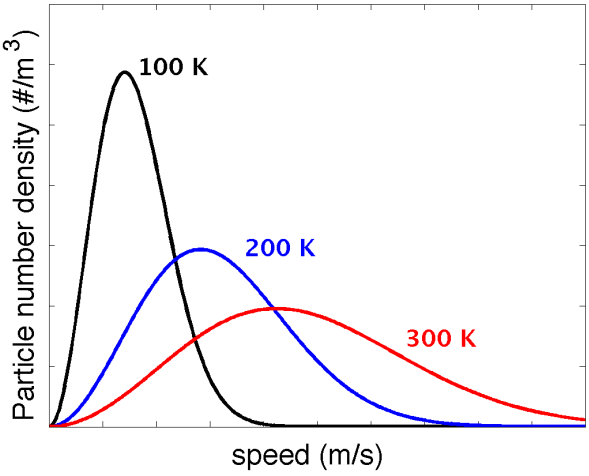

Fig. 7. Maxwellian velocity distributions for different temperatures.

Sometimes the literature also refers to ion or electron temperatures because, in plasmas, the ions and electrons often have separate Maxwellian distributions. In the presence of a strong magnetic field, even a single species (ions or electrons) can have different temperatures because the components of velocity perpendicular and parallel to this field may also belong to different Maxwellian distributions. Additionally, it is important to note that each species is not restricted to only Maxwellian distributions,

but could instead belong to non-Maxwellian distribution functions, for which the concept of temperature becomes much more vague.

Finally, there are three conditions that an ionized gas must satisfy to be called a plasma. These conditions are called the "plasma criteria," and are discussed in the remainder of this section, following Chen [33].

1. 1^{st} Plasma Criterion: $\lambda_D << L$

Consider the following thought experiment: A box of characteristic length L containing an equal number of positive ions and electrons has an electric field applied to it by a battery, as shown in Figure 8. It is assumed that no ions or electrons recombine with the charge from the battery. In the ideal case, the particles attract to the leads of the battery until they exactly balance the charge of each lead, thus exactly canceling the effect of the applied electric field. This effect is what is known as plasma shielding or Debye shielding, and it is an important static property of plasmas.

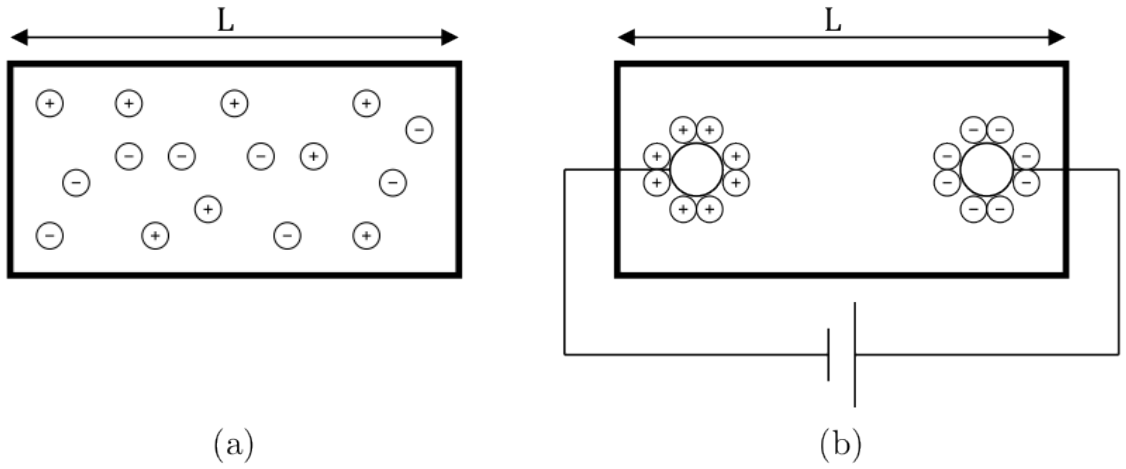

Fig. 8. Box of charged particles (a), box of charged particles with electric potential applied (b).

Real plasmas cannot perfectly shield out electric fields because the kinetic energy

(i.e. temperature) of the plasma particles is finite. This means that some particles will escape the influence of the leads and cause a finite electric field to exist in the plasma, as shown in Figure 9. The first order approximation for the thickness of the charge cloud (sometimes called a "sheath") surrounding the leads is known as the Debye length, λ_D. An ionized gas must be sufficiently dense enough, or the system large enough, such that $\lambda_D << L$ in order for it to be considered a plasma.

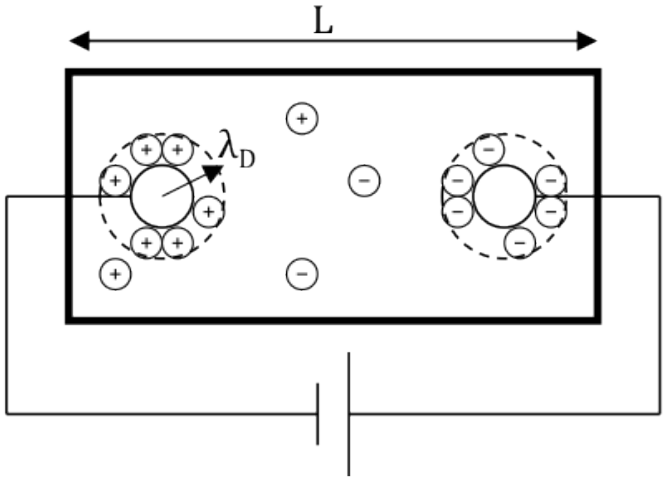

Fig. 9. Debye shielding in real plasmas.

2. 2^{nd} Plasma Criterion: $N_D >> 1$

N_D is sometimes called the "plasma parameter," and it is the number of particles in a Debye sphere for some particular medium. A Debye sphere is simply a sphere with a radius equal to the Debye length. Therefore, the plasma parameter is written as:

$$N_D = \frac{4}{3} n \pi \lambda_D^3$$

This second criterion is necessary for collective behavior to dominate over collisions and only when N_D is much, much greater than unity can the medium be considered a plasma.

3. 3^{rd} Plasma Criterion: $\omega\tau > 1$

The plasma frequency, ω, is a measure of typical oscillations in a plasma. These typical oscillations are also called Langmuir waves, and are characterized by the rapid oscillation of the electron density in a plasma. An illustrative example is shown in Figure 10. In part A of the figure, a high density cloud of electrons with relatively few ions is shown. Initially the repulsive force between electrons dominates. The electrons disperse, but overshoot the electric potential equilibrium and are drawn back toward the positive ions as shown in part B. The frequency of these electron oscillations in a plasma is the plasma frequency. The average time between electron collisions with neutral atoms is τ. The 3^{rd} and final plasma criterion basically states that in order for an ionized gas to be considered a plasma, the frequency of electron collisions with neutral atoms must be less than the plasma frequency.

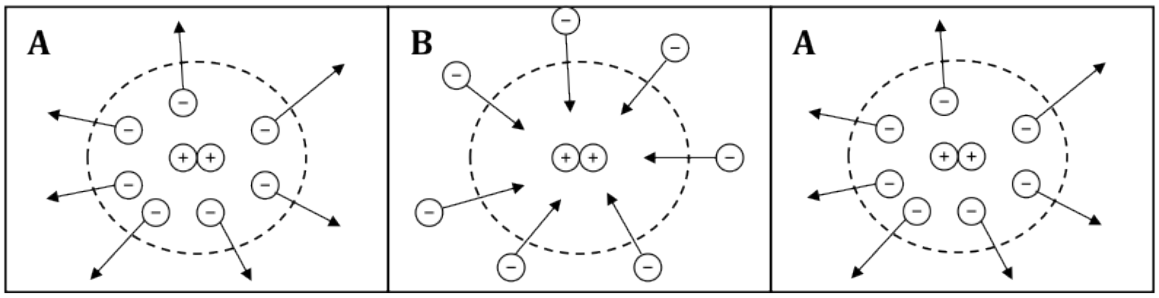

Fig. 10. Electron density oscillations (potential equilibrium represented by dotted line).

B. Particle Model

Conceptually, the simplest approach to modeling a plasma is to consider the ions and electrons as individual particles. The (non-relativistic) particle dynamics are governed by a simple equation, which is Newton's second law, $\mathbf{F} = m\mathbf{a}$. Neglecting

gravity, the dominant force is the Lorentz force, which gives the following equation of motion for each particle:

$$m_i \frac{d\mathbf{v}_i}{dt} = q_i[\mathbf{E} + \mathbf{v}_i \times \mathbf{B}] \tag{2.1}$$

where m is the mass of particle i, q is the charge of the particle, $\mathbf{v}$ is the particle velocity, and $\mathbf{E}$ and $\mathbf{B}$ are the total electric and magnetic fields at the particle's current position. The electric field, $\mathbf{E}$, and magnetic field, $\mathbf{B}$, are also time dependent and coupled to the motion of the particles. These fields obey Maxwell's laws, which are given as the following:

$$\nabla \cdot \mathbf{B} = 0 \tag{2.2}$$

$$\nabla \cdot \mathbf{E} = \frac{1}{\epsilon_0} \sum_i n_i q_i \tag{2.3}$$

$$\nabla \times \mathbf{B} = \mu_0 \sum_i n_i q_i \mathbf{v}_i + \mu_0 \epsilon_0 \frac{\partial \mathbf{E}}{\partial t} \tag{2.4}$$

$$\nabla \times \mathbf{E} = -\frac{\partial \mathbf{B}}{\partial t} \tag{2.5}$$

The particle description of a plasma is very useful for gaining intuition about certain plasma concepts, such as particle orbits and drifts, as shown in Figures 11(a) & 11(b). However, the particle description is also the most impractical to apply directly for full-scale computer simulations. For example, if a $1m^3$ cloud of plasma has a number density of $10^{16}/m^3$, then at least 2×10^{16} equations must be solved simultaneously. On a computer, storing 3 velocities and 3 positions for all the particles requires about 10^{17} bytes of memory using double precision. Even one of the most powerful computers in the world today, NASA's Pleiades Supercomputer, has only about 10^{14} bytes of memory, which is 1000 times less than needed for simulating this plasma cloud. Besides memory, the other major constraint is the large difference in

mass between ions and electrons. Single ionized Argon, for example, has an ion to electron mass ratio of about 72,000. This large mass ratio means that the electrons are much more mobile than the ions, and numerically this leads to stiffness in the equations due to the large difference in time scales for the motion of ions and electrons.

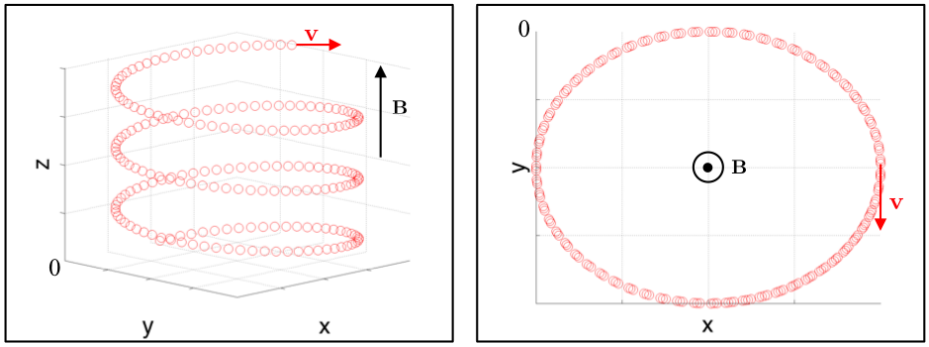

(a) Single ion particle orbit with constant applied **B** field.

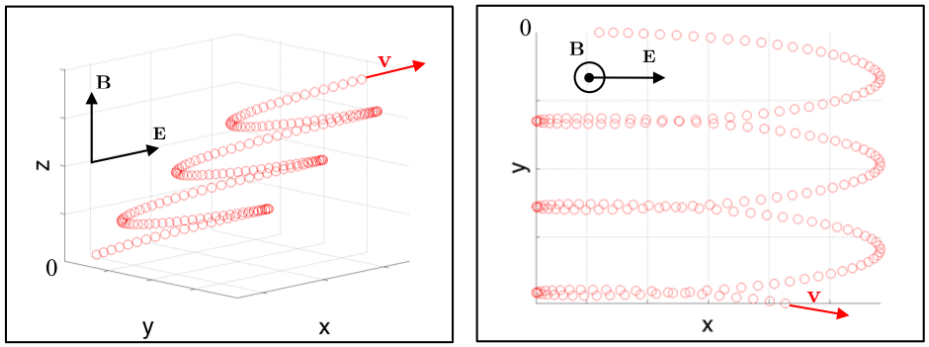

(b) Single ion particle drift with constant applied **E**&**B** fields.

Fig. 11. Example of particle dynamics with constant applied fields.

However, there are numerical "tricks" that can be used to make a particle simulation much more feasible than what has been described here. Birdsall and Langdon were some of the first pioneers in employing methods for particle simulations of plasmas and their text [34] is a good point of reference on the subject.

C. Kinetic Model

Another approach to modeling a plasma is based on the kinetic theory of gases. In the kinetic description, individual particle trajectories are described statistically by a particle distribution function, f. The dimensional quantity, f, is the number density of particles at time, t, in a six-dimensional phase space (x, y, z, u, v, w). The integral of f over all of velocity space gives the number density of particles, n, in physical space at time, t. This is written as follows:

$$n = \int_{-\infty}^{\infty} \int_{-\infty}^{\infty} \int_{-\infty}^{\infty} f du dv dw \tag{2.6}$$

In SI units, n has units of number of particles/m^3. The rate of change of f with respect to physical space, time, and velocity space, is given by Boltzmann's equation. In its most general form, Boltzmann's equation is written as:

$$\frac{\partial f}{\partial t} + \mathbf{v} \cdot \nabla_{\mathbf{x}} f + \mathbf{a} \cdot \nabla_{\mathbf{v}} f = \left(\frac{\partial f}{\partial t} \right)_{collisions} \tag{2.7}$$

This equation equates the net influx of particles into a region of six-dimensional (6-D) phase space to the accumulation of particles in this region. The particle velocity, $\mathbf{v}$, and acceleration, $\mathbf{a}$, are in a laboratory reference frame, and the gradient with respect to physical and velocity space are represented by $\nabla_{\mathbf{x}}$ and $\nabla_{\mathbf{v}}$, respectively. The right-hand-side is a general representation of the collision operator, which accounts for particle interactions. For a single ionized gas, the general form of the Boltzmann equation for both the ion and electron species is written as the following:

$$\frac{\partial f_e}{\partial t} + \mathbf{v_e} \cdot \nabla_{\mathbf{x}} f_e + \frac{q_e}{m_e} \left(\mathbf{E} + \mathbf{v_e} \times \mathbf{B} \right) \cdot \nabla_{\mathbf{v}} f_e = \left(\frac{\partial f_e}{\partial t} \right)_{collisions} \tag{2.8}$$

$$\frac{\partial f_i}{\partial t} + \mathbf{v_i} \cdot \nabla_{\mathbf{x}} f_i + \frac{q_i}{m_i} (\mathbf{E} + \mathbf{v_i} \times \mathbf{B}) \cdot \nabla_{\mathbf{v}} f_i = \left(\frac{\partial f_i}{\partial t} \right)_{collisions} \tag{2.9}$$

where the acceleration due to the Lorentz force has been included. To illustrate this concept more clearly, consider the following 1-D example from Bellan [35]: The position of a group of particles in 1-D physical space is represented by $x_i = x_i(t)$, where the subscript refers to each individual particle. Similarly, the velocity of the particles in 1-D velocity space is $u_i = u_i(t)$. A plot of the 2-D phase space for one instant in time is shown in Figure 12. Each blue dot represents an individual particle trajectory. The particle distribution function, $f = f(x, u, t)$, describes the distribution of the blue dots in the 2-D phase-space. In Figure 12, $f dx du$ is the number of particles at time t within the black box.

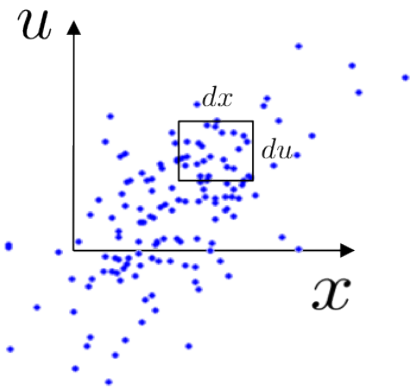

Fig. 12. 2-D phase space.

It is important to emphasize that the evolution of f does not keep track of individual particle trajectories. Instead, it characterizes groups of particles having the same position and velocity. This kinetic description of a plasma is less detailed than following individual particles, but it is still very difficult to use in 3-D numerical simulations.

D. Fluid Model

From the kinetic description, a fluid or continuum model for a plasma can be derived by taking "moments" of the particle distribution function. Bellan [35] gives a nice physical interpretation of this moment taking as follows. The number of particles in the shaded region shown in Figure 13 is the number of blue dots between x and $x+dx$. An equivalent definition is to define $n(x)$ as the density of particles at position x and then the number of particles in the shaded region is just $n(x)dx$. From the last section, it was shown that $n(x) = \int f(x,u)du$. Therefore, the transition from a kinetic to a continuum description, where only position is an independent variable, involves "integrating out" the velocity dependence. Other macroscopic quantities, such as the average velocity or energy of all the particles, can also be derived by multiplying f by powers of u and integrating over the velocity space. This procedure is what is meant by "taking moments" of the distribution function.

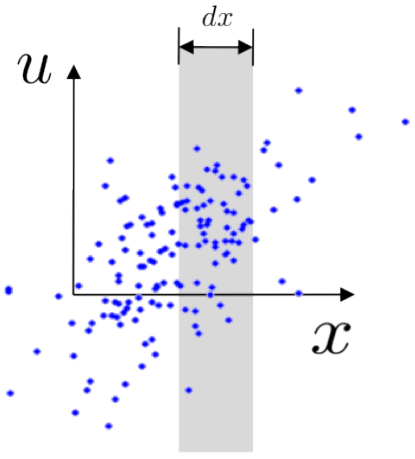

Fig. 13. *"Moments give weighted averages of the particles in the shaded vertical strip." [35]*

1. Two-Fluid Equations

Following this procedure of taking moments, equations 2.8 and 2.9 can be integrated to give what are called the "two-fluid" equations. For simplicity, it is assumed that the plasma is fully ionized, so that no equations are needed for the neutral particles. Taking the "zeroth moment," i.e. multiplying equations 2.8 and 2.9 by $\mathbf{v}^0$ and integrating, gives the continuity equation for both electrons and ions:

$$\frac{\partial n_e}{\partial t} + \nabla \cdot (n_e \mathbf{u_e}) = 0 \tag{2.10}$$

$$\frac{\partial n_i}{\partial t} + \nabla \cdot (n_i \mathbf{u_i}) = 0 \tag{2.11}$$

here $\mathbf{u}$ is now the mean velocity vector and $\mathbf{v}$ is the particle velocity. To clarify the new notation, in the 1-D example of the previous subsection, $\mathbf{v} = [u, 0, 0]$, and now $\mathbf{v} = [u, v, w]$. Now multiplying equations 2.8 and 2.9 by $\mathbf{v}^1$ and integrating over velocity, i.e. taking the "first moment," gives the equation of motion for each species:

$$n_e m_e \left(\frac{\partial \mathbf{u}_e}{\partial t} + \mathbf{u}_e \cdot \nabla \mathbf{u}_e \right) = n_e q_e \left(\mathbf{E} + \mathbf{u}_e \times \mathbf{B} \right) - \nabla \cdot \underline{\mathbf{P}}_e - \mathbf{R}_{ei} \tag{2.12}$$

$$n_i m_i \left(\frac{\partial \mathbf{u}_i}{\partial t} + \mathbf{u}_i \cdot \nabla \mathbf{u}_i \right) = n_i q_i \left(\mathbf{E} + \mathbf{u}_i \times \mathbf{B} \right) - \nabla \cdot \underline{\mathbf{P}}_i - \mathbf{R}_{ie} \tag{2.13}$$

where $\underline{\mathbf{P}}$ is the pressure tensor and $\mathbf{R}_{ei}$ is the net frictional drag force due to collisions of electrons with ions, and vice versa for $\mathbf{R}_{ie}$. It is not written here, but the second moment is similarly obtained by multiplying the ion and electron Boltzmann equations by $m\mathbf{v}^2/2$, and this gives the energy evolution equation for each species. This process of taking moments can go on forever and does not lead to a closed system of equations. For the zeroth moment, an equation for density results, but velocity

appears. To obtain an equation for velocity, the first moment is taken, but then pressure appears. Then for the second moment, an equation for pressure results, but heat flux appears, etc. Therefore, some form of "closure model" is always needed for the fluid equations to terminate this moment taking process. Typically, moments are terminated after obtaining the energy equation and an equation relating pressure to other thermodynamic properties such as density and temperature is used to close the system.

2. Single-Fluid Equations

From the two-fluid system, two new velocity-like variables can be introduced that are a linear combination of $\mathbf{u}_e$ and $\mathbf{u}_i$. These new variables are the current density, $\mathbf{J}$, and the center-of-mass velocity, $\mathbf{U}$, which are expressed as the following:

$$\mathbf{J} = \sum_s n_s q_s \mathbf{u}_s$$

$$\mathbf{U} = \frac{1}{\rho} \sum_s m_s n_s \mathbf{u}_s$$

and

$$\rho = \sum_s m_s n_s$$

is the total mass density. The summation is taken over all of the species, s. To obtain single-fluid equations for a plasma, equations 2.10-2.13, as well as the energy equation, are multiplied by m_s and summed over all of the species, s. The single-fluid equations are more traditionally known as the Magnetohydrodynamic (MHD) equations and are primarily concerned with low-frequency, long-wavelength, magnetic behavior of a plasma [35]. One form of the resulting conservation equations is given as follows.

Conservation of mass:

$$\frac{\partial \rho}{\partial t} = -\nabla \cdot (\rho \mathbf{U}) \tag{2.14}$$

Conservation of linear momentum:

$$\rho \frac{\partial \mathbf{U}}{\partial t} = -\rho(\mathbf{U} \cdot \nabla)\mathbf{U} - \nabla p + \Psi_{viscous} + \mathbf{J} \times \mathbf{B} \tag{2.15}$$

Conservation of energy:

$$\rho \frac{\partial e}{\partial t} = -\rho(\mathbf{v} \cdot \nabla)e - p\nabla \cdot \mathbf{v} + \Phi_{viscous} + \nabla \cdot (k\nabla T) + \frac{\mathbf{J}^2}{\sigma} \tag{2.16}$$

Besides Maxwell's laws and the required equations of state, there is still one last equation needed to relate the current density to the other field quantities. The electron equation of motion, equation 2.12, can be rewritten as the following:

$$m_e \frac{d\mathbf{u}_e}{\partial t} = -e\left(\mathbf{E} + \mathbf{u}_e \times \mathbf{B}\right) - \frac{1}{n_e}\nabla\left(n_e k T_e\right) - \nu_{ei} m_e \left(\mathbf{u}_e - \mathbf{u}_i\right) \tag{2.17}$$

where a scalar pressure has been substituted and ν_{ei} is the rate at which electron momentum is destroyed by collisions with ions. Typically, the electron inertia term is neglected because the physical phenomenon being studied happens on a time-scale that is long compared to the electron cyclotron motion. Also, due to the large mass of ions relative to electrons, a good approximation is $\mathbf{U} \approx \mathbf{u_i}$. Finally, using the definition of current density, the electron equation of motion reduces to the generalized Ohm's law:

$$\mathbf{E} + \mathbf{U} \times \mathbf{B} - \frac{1}{n_e e}\mathbf{J} \times \mathbf{B} + \frac{1}{n_e e}\nabla\left(n_e k T_e\right) = \eta \mathbf{J} \tag{2.18}$$

where $\eta = m_e \nu_{ei}/n_e e^2 = 1/\sigma$ is the electrical resistivity. The curl of equation 2.18 gives the induction equation, which is the time evolution of the magnetic field and is

written as:

$$\frac{\partial \mathbf{B}}{\partial t} = \nabla \times (\mathbf{U} \times \mathbf{B}) - \frac{1}{\mu_0} \nabla \times \frac{\nabla \times \mathbf{B}}{\sigma} - \nabla \times \left[\frac{1}{n_e e \mu_0} (\nabla \times \mathbf{B}) \times \mathbf{B} \right] - \frac{1}{n_e e} \nabla n_e \times \nabla k T_e \tag{2.19}$$

where the pre-Maxwell, Ampere's law has been substituted for $\mathbf{J}$. The first term on the right hand side of equation 2.19 is the convective term, the second is the resistive term, the third is the Hall term, and the fourth is the electron pressure gradient term. Under certain conditions, neglecting as many as three of the terms on the right hand side of equation 2.19 is appropriate, and leads to different systems of MHD equations. The single-fluid MHD equations are an attractive model for numerical analysis because they are much more computationally tractable than kinetic or single particle descriptions. The MHD model is used in this thesis for numerical plasma simulations, and the range of validity in using this model is addressed in the next chapter, specifically for magnetic nozzle simulations.

E. Chapter Summary

In this chapter, the fundamental methods for modeling a plasma were introduced. The particle method was shown to be useful for its educational value, but overly restrictive for large scale computer simulations. The kinetic method was also restrictive for computations, but is an essential part to understanding more numerically tractable fluid equations. The two-fluid equations were derived by directly taking moments of the kinetic equations for each plasma species, and the single-fluid, or MHD equations were shown to be a linear combination of the two-fluid equations. The next chapter examines the parameter space of these fluid equations in order to determine the appropriate assumptions for magnetic nozzle flows.

CHAPTER III

PARAMETRIC ANALYSIS FOR MHD SIMULATIONS

As mentioned in the last chapter, MHD is an attractive model for analyzing the physics of plasmas due to its computational tractability, but also because of the large body of supporting literature that has been accumulated over many decades of research. The term "MHD" itself in the literature is sometimes subject to different interpretations. Depending on the level of complexity desired, the set of MHD equations can vary widely from describing a perfectly conducting, inviscid fluid (ideal MHD), to including finite resistivity (resistive MHD), the Hall effect (Hall MHD), or even displacement current (relativistic MHD). A more comprehensive term for what MHD actually represents is a fluid model for a plasma, as discussed in the previous chapter. In Chapter II, it was noted that the fluid equations are derived from taking moments of Boltzmann's equation. It is the closure of the Boltzmann moments where a majority of plasma physics is either included or neglected in the fluid model. Determining the appropriate terms to neglect depends on their relative ordering and the physical problem being studied, and care must be taken to ensure that the ordering is self-consistent and reasonably realistic.

With the goal in mind of conducting magnetic nozzle simulations using a fluid model, this chapter examines the parameter regimes of a single, fully-ionized Argon plasma and determines the appropriate assumptions required. The analysis follows directly from the work of Kantrowitz et al. [36], which looks directly at the relative order of magnitude of the terms in the electron and ion Boltzmann equations based on characteristic length scales. The theoretical analysis is then applied to examine the flow characteristics of the latest VASIMR® experimental rocket, the VX-200 [37], being developed by the Ad Astra Rocket Company in Houston, TX. This system uses

a magnetic nozzle to accelerate an Argon plasma to produce thrust. An estimate of typical nozzle flow conditions from experimental data is also presented. Additionally, the work presented in this chapter is taken directly from a recent paper presented at the AIAA 2011 Hawaii Summer Conferences [38].

A. Parametric Analysis of Boltzmann's Equation

The starting point for the parametric analysis is the general form of Boltzmann's equation for a single-ionized gas, which is written for both the ion and electron species as the following:

$$\frac{\partial f_e}{\partial t} + \mathbf{v_e} \cdot \nabla_{\mathbf{x}} f_e + \frac{q_e}{m_e} (\mathbf{E} + \mathbf{v_e} \times \mathbf{B}) \cdot \nabla_{\mathbf{v}} f_e = \left(\frac{\partial f_e}{\partial t} \right)_{collisions} \tag{3.1}$$

$$\frac{\partial f_i}{\partial t} + \mathbf{v_i} \cdot \nabla_{\mathbf{x}} f_i + \frac{q_i}{m_i} (\mathbf{E} + \mathbf{v_i} \times \mathbf{B}) \cdot \nabla_{\mathbf{v}} f_i = \left(\frac{\partial f_i}{\partial t} \right)_{collisions} \tag{3.2}$$

where the acceleration due to the Lorentz force has been included. The parametric analysis of equations 3.1 and 3.2 follows directly from Kantrowitz et al. [36]. The first step is to first invoke the Bhatnager-Gross-Krook (BGK) approximation for the collision operator and propose the standard scaling for relaxation time, τ:

$$\left(\frac{\partial f}{\partial t} \right)_{collisions} = \frac{f_0 - f}{\tau}; \qquad \tau \approx \frac{\lambda}{v_{th}}$$

where λ is the electron mean free path (mfp), v_{th} is the thermal velocity, and f_0 is the Maxwellian particle distribution function.

$$\lambda \approx \left[8.1 n_e \left(\frac{e^2}{(3kT)(4\pi\epsilon_0)} \right)^2 ln \left(\frac{d(4\pi\epsilon_0)(3kT)}{e^2} \right) \right]^{-1} \tag{3.3}$$

$$v_{th} = \sqrt{\frac{8kT}{\pi m}}; \qquad d = \sqrt{\frac{\epsilon_0 kT}{2n_e e^2}}$$

Also, in the definition of λ the Debye length, d, was introduced, which is a measure of the separation distance between ions and electrons in a plasma. Next, the Boltzmann equation is rewritten with the BGK collision operator as follows:

$$\frac{\partial f}{\partial t} + \mathbf{v} \cdot \nabla_{\mathbf{x}} f + \frac{q}{m} (\mathbf{E} + \mathbf{v} \times \mathbf{B}) \cdot \nabla_{\mathbf{v}} f = \frac{(f_0 - f) v_{th}}{\lambda} \tag{3.4}$$

Now a characteristic length, l_0, is selected to nondimensionalize the above equation:

$$\frac{l_0}{v_{th} f} = \frac{t_0}{f}$$

which yields the following equation:

$$\frac{t_0}{f}\frac{\partial f}{\partial t} + \frac{l_0}{v_{th} f}\mathbf{v} \cdot \nabla_{\mathbf{x}} f \pm \frac{e l_0}{m v_{th} f} (\mathbf{E} + \mathbf{v} \times \mathbf{B}) \cdot \nabla_{\mathbf{v}} f = \frac{l_0 (f_0 - f) v_{th}}{v_{th} f \lambda}$$

$$t_0 \frac{\partial}{\partial t}(lnf) + \frac{\mathbf{v}}{v_{th}} \cdot l_0 \nabla_{\mathbf{x}}(lnf) \pm \frac{e l_0}{m v_{th}} (\mathbf{E} + (\mathbf{v_{th}} + \mathbf{v_g}) \times \mathbf{B}) \cdot \nabla_{\mathbf{v}}(lnf) = \frac{l_0}{\lambda}\left(\frac{f_0}{f} - 1\right) \tag{3.5}$$

Here the total particle velocity, $\mathbf{v}$, is defined to be the sum of the gas velocity, $\mathbf{v_g}$, and the particle thermal velocity. Further, $\mathbf{E}'$ is the electric field in the coordinate frame moving with the gas velocity and r_L is the Larmor radius:

$$\mathbf{E}' = \mathbf{E} + \mathbf{v_g} \times \mathbf{B}; \qquad r_L = \frac{m v_\perp}{eB} \approx \frac{m v_{th}}{eB}$$

After substituting $\mathbf{E}'$ and r_L, equation 3.5 reduces to the final nondimensional form:

$$t_0\frac{\partial}{\partial t}(lnf)+\frac{\mathbf{v}}{v_{th}}\cdot l_0\nabla_{\mathbf{x}}(lnf)\pm\frac{el_0}{mv_{th}^2}\mathbf{E}'\cdot v_{th}\nabla_{\mathbf{v}}(lnf)\pm\frac{l_0}{r_L}\left(\hat{\mathbf{v}}_{\mathbf{th}}\times\hat{\mathbf{B}}\right)\cdot v_{th}\nabla_{\mathbf{v}}(lnf)=\frac{l_0}{\lambda}\left(\frac{f_0}{f}-1\right) \tag{3.6}$$

where $\hat{\mathbf{v}}_{\mathbf{th}}$ and $\hat{\mathbf{B}}$ are both unit vectors. Upon normalization, it is reasonable to assume that the following terms are of order unity:

$$t_0\frac{\partial}{\partial t}(lnf)=O(1);\qquad l_0\nabla_{\mathbf{x}}(lnf)=O(1);\qquad v_{th}\nabla_{\mathbf{v}}(lnf)=O(1)$$

Owing to charge neutrality, another reasonable assumption is that the local electric field maintains roughly equal and opposite forces for both ions and electrons:

$$n_e e\mathbf{E}'\approx\rho\left(\frac{\partial\mathbf{v}}{\partial t}+\mathbf{v}\cdot\nabla\mathbf{v}\right)=O\left(\frac{\rho v_{th}^2}{l_0}\right)\qquad\frac{el_0}{mv_{th}^2}\mathbf{E}'=O(1)$$

Subject to these simplifications, the balance in equation 3.6 can be written in terms of characteristic length scales as follows:

$$O_E(1)+O_B\left(\frac{l_0}{r_L}\right)=O_C\left(\frac{l_0}{\lambda}\right) \tag{3.7}$$

In equation 3.7, O_E represents the first three terms in equation 3.6; O_B represents the magnetic field effects, and O_C represents the collisional effects. Next, using equation 3.7, the different parametric regimes of MHD physics are classified following the arguments of Kantrowitz et al. The classification based on temperature and electron density is graphed in the figure on page 34.

1. S: Scalar Region

In this region, the Larmor radius of both the ions and electrons is greater than the electron mean free path, which is assumed to be much smaller than the characteristic

length.

$$r_{Le} > \lambda$$

$$r_{Li} > \lambda$$

$$\epsilon = \frac{\lambda}{l_0} << 1$$

Multiplying equation 3.7 by ϵ for both the ions and electrons gives:

$$O_E(\epsilon) + O_B\left(\frac{\lambda}{r_{Li}}\right) = O_C(1) \tag{3.8}$$

$$O_E(\epsilon) + O_B\left(\frac{\lambda}{r_{Le}}\right) = O_C(1) \tag{3.9}$$

Equations 3.8 and 3.9 imply that the collision term is dominant in this region for both ions and electrons. When collisions are dominant, the distribution function will be close to a Maxwell distribution. Physically, this means that the electrons and ions tend to drift through the gas similar to diffusion in a neutral gas. The region is labeled as scalar because the electrical conductivity, σ, is scalar in this domain.

2. T: Tensor Region

This region is the same as the scalar region except that now the Larmor radius of the electrons is smaller than the mean free path.

$$r_{Le} < \lambda$$

$$r_{Li} > \lambda$$

$$\epsilon_e = \frac{r_{Le}}{l_0} << 1$$

$$\epsilon_i = \frac{\lambda}{l_0} << 1$$

Again multiply equation 3.7 by ϵ_i for the ions and ϵ_e for the electrons to give:

$$O_E(\epsilon_i) + O_B\left(\frac{\lambda}{r_{Li}}\right) = O_C(1) \tag{3.10}$$

$$O_E(\epsilon_e) + O_B(1) = O_C\left(\frac{r_{Le}}{\lambda}\right) \tag{3.11}$$

Equation 3.10 shows that the collision term is still dominant for the ions, but equation 3.11 implies that the magnetic field term is dominant for the electrons. The ions dictate much of the fluid-like properties because of their much greater relative mass compared to the electrons. However, Ohm's law, and thus the conductivity of the gas, is derived from the electron equation of motion. When the magnetic term becomes dominant in the electron equation of motion, the current is no longer purely parallel to an applied electric field in the presence of an applied magnetic field. Therefore, the electrical conductivity is in general no longer scalar, and this region is labeled as tensor.

3. M: Magnetic Region

In this region, now both the ion and electron Larmor radii are smaller than the mean free path and are also assumed to be much smaller than the characteristic length scale.

$$\lambda > r_{Le}$$

$$\lambda > r_{Li}$$

$$\epsilon_e = \frac{r_{Le}}{l_0} << 1$$

$$\epsilon_i = \frac{r_{Li}}{l_0} << 1$$

Again multiply equation 3.7 by ϵ_i for the ions and ϵ_e for the electrons to give:

$$O_E(\epsilon_i) + O_B(1) = O_C\left(\frac{r_{Li}}{\lambda}\right) \tag{3.12}$$

$$O_E(\epsilon_e) + O_B(1) = O_C\left(\frac{r_{Le}}{\lambda}\right) \tag{3.13}$$

Now, both the ion and electron Boltzmann equations, and hence all transport properties, are dominated by the magnetic field terms. However, collisions are still important to some degree because the magnetic field only restricts motion perpendicular to the field lines.

4. EM: Electromagnetic Region

In this region, both the ion Larmor radius and the mean free path become greater than the characteristic length of the system. Also, the electron Larmor radius is assumed to be much smaller than the characteristic length.

$$\lambda > l_0$$

$$r_{Li} > l_0$$

$$\epsilon_e = \frac{r_{Le}}{l_0} << 1$$

Now multiply equation 3.7 by ϵ_e for the electrons this time and simply rewrite it for the ions as follows:

$$O_E(1) + O_B\left(\frac{l_0}{r_{Li}}\right) = O_C\left(\frac{l_0}{\lambda}\right) \tag{3.14}$$

$$O_E(\epsilon_e) + O_B(1) = O_C\left(\frac{r_{Le}}{\lambda}\right) \tag{3.15}$$

Equation 3.15 shows that the electron equation is still dominated by magnetic terms. However, more interestingly, equation 3.14 shows that the ion equation is no longer dominated by the magnetic field terms. Instead, it is the local electric field ($\mathbf{E}'$) which becomes important in this region. Physically, the picture is that the ions are no longer bound by the magnetic field, but are still subject to the electric fields which maintain plasma quasineutrality. Alternatively, this can be interpreted as the breakdown of the so-called "guiding center approximation" for the ions gyrating about the magnetic field. This approximation states that the rate of change of any field quantity and its gradient, measured in the guiding-center system, should be small during a gyration period [39].

5. E: Electric Region

Finally, when the electron Larmor radius becomes larger than the characteristic length, and the mean free path is much larger than characteristic length, the following equations result:

$$r_{Le} > l_0$$

$$r_{Li} > l_0$$

$$\epsilon = \frac{l_0}{\lambda} << 1$$

$$O_E(1) + O_B\left(\frac{l_0}{r_{Li}}\right) = O_C(\epsilon) \tag{3.16}$$

$$O_E(1) + O_B\left(\frac{l_0}{r_{Le}}\right) = O_C(\epsilon) \tag{3.17}$$

In this region, collisions are negligible and, to a lesser degree, so are the magnetic field terms when compared to the local electrical forces.

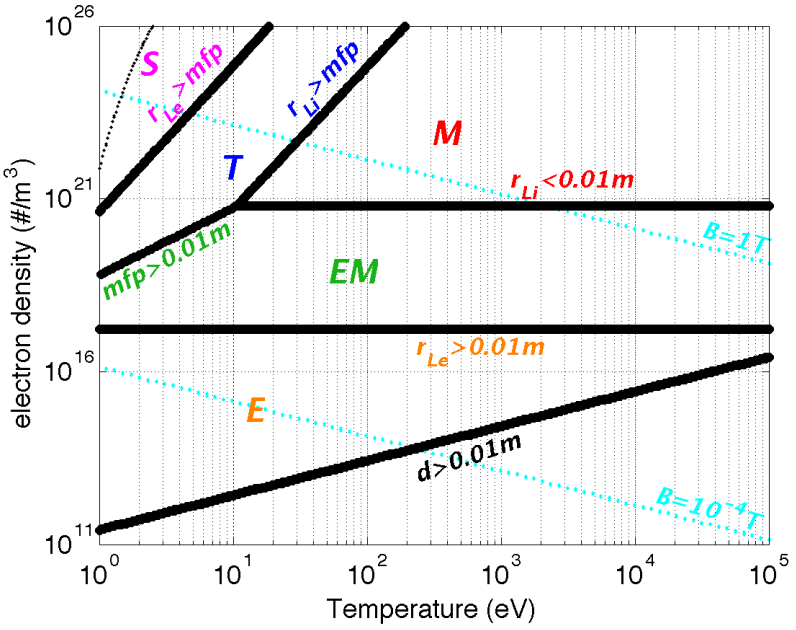

Fig. 14. Single ionized Deuterium, $\beta = 1$, thermal equilibrium.

All the regions are summarized in Figure 14, which is a reproduction from Kantrowitz (and also given in Sutton [40]) for Deuterium gas with a characteristic length of $l_0 = 0.01m$. The major assumptions of this figure are that the plasma is quasineutral, i.e. $n_i \approx n_e$, single-ionized, and in thermal equilibrium. Also, in order to emphasize the coupling between gas pressure and electromagnetic stress on the transfer of momentum and energy in the plasma, it is assumed that magnetic pressure, $B^2/2\mu_0$, is equal to the gas pressure, $2n_ekT$, everywhere. This is equivalent to presuming that $\beta = 1$ at every point in the figure. The dotted light blue lines show the points where the magnitude of the magnetic field is equal to $1T$ and $10^{-4}T$. The solid black lines are labeled according to the relevant length scales that divide the regions. It is important to note, however, that the solid black lines do not make

the regions mutually exclusive. For example, tensorial resistivity is still important in the M region, but additionally other transport properties are dominated by the effect of the magnetic field. Also, the region to the right of the curved dotted black line represents greater than 50% ionization, which is calculated by the Saha equation [33]. Figure 14 gives some insight into the appropriate set of fluid equations to use for a given range of temperature and density. As an example, consider the transition between the S and T regions. In the S region, it is appropriate to use resistive, single-fluid MHD equations and to take resistivity as a scalar quantity. However, in the T region, resistivity must be considered tensorial, and depending on the characteristic frequency of the phenomenon being studied, the Hall effect may become important as well.

It is evident from the above analysis that the physics and consequently model equations governing a plasma flow depend critically upon the nondimensional flow parameters. For a given device, it is important to revisit the above analysis for the specific operating conditions to determine applicable model equations. In the next section, the above analysis is applied to the VX-200 operating conditions.

B. Magnetic Nozzle Parameterization

To characterize "typical" flow parameters in the VX-200 plume, existing data that was taken from recent VX-200 experiments is examined.

1. VX-200 Data

The experimental data presented in this section is taken from several different test firings of the VX-200 rocket at a total power of approximately $170kW$. Only measurements taken along the centerline of the nozzle are presented here. Figure 15 illustrates

representative axial locations of two different data points in the plume with the corresponding data given in Table I. The instruments used during the experiment are fixed to a translational stage that moves in the horizontal (yz) plane with the nozzle centerline aligned with the z axis. More details about the instrumentation and experimental setup are given by Bering et al. [37]. The exit plane where the magnetic nozzle is assumed to start is at $z = 2.61m$, meaning that data point 1 is about $0.18m$ downstream of what is termed the nozzle "throat."

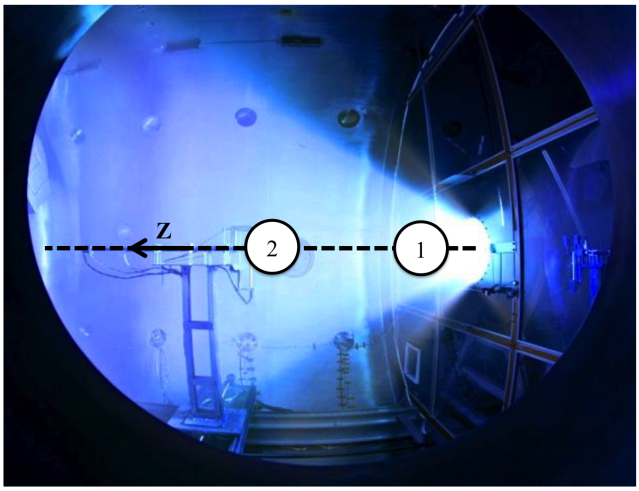

Fig. 15. VX-200 plume with Argon plasma.

Table I. Typical flow parameters for the VX-200 rocket.

Location	1	2
Chamber coordinate z (m)	2.79	3.59
Distance from "throat" (m)	0.18	0.98
Plasma density ($\#/m^3$)	$\sim 10^{17} - 10^{19}$	$\sim 10^{16} - 10^{18}$
Magnetic field magnitude (T)	~ 0.055	~ 0.008
Electron temperature (eV)	~ 6	~ 5
$\perp$ Ion temperature (eV)	$\sim 10^{1} - 10^{2}$	$\sim 10^{0} - 10^{1}$

The electrons are assumed to be in thermal equilibrium throughout the plume

due to their high mobility and the effects of "line-tying." Therefore, it is reasonable to assume that the electron temperature is representative of a Maxwellian distribution both parallel and perpendicular to the applied magnetic field. The ions, however, are flowing at a speed greater than the ion thermal speed, meaning that they are supersonic. Therefore, they cannot equilibrate to a Maxwellian distribution in the parallel or perpendicular direction, which makes it very difficult to quantify a measure of ion temperature. The current technique [37] used to infer parallel ion temperature is to fit a least squares approximation of a drifting Maxwellian distribution to data from a Retarding Potential Analyzer (RPA), which measures ion energy. However, even this ion temperature is only representative of the parallel direction; to apply the Boltzmann analysis, we need to know something about the perpendicular direction. Currently, there is no experimental RPA data to measure perpendicular ion energy in the VX-200 plume, and thus no representative measure of ion temperature perpendicular to the magnetic field. Therefore, the ion perpendicular temperature given in Table I is an educated guess based on the experimental experience of Ad Astra engineers.

2. Parametric Space of VX-200

From the analysis presented in Section A, a parameter map can be constructed for Argon as was done for Deuterium, and this is shown in Figure 16. In this figure, a characteristic length of $l_0 = 0.2m$ is assumed, which is an estimate of the plume half-width diameter at the nozzle throat. Figure 16 also assumes again that $\beta = 1$ and that the plasma is in thermal equilibrium. The Debye length of the plasma throughout the plume is on the order of about $10^{-4}m$, and thus plasma quasineutrality, i.e. $n_e \approx n_i$, is a good approximation. Also present in the figure is a superposed grey box that outlines the parameter range between data points 1 and 2 in the magnetic nozzle

section of the VX-200. While it is true that $\beta = 1$ and thermal equilibrium are not very good assumptions for the entire plume, it is shown that even in more extreme cases, the regions do not shift enough to change the physical picture illustrated in Figure 16.

Consider the following two pertinent extreme cases: (1) $\beta = 0.2$, and $T_{i\perp}/T_{e\perp} = 10$ and (2) $\beta = 2$, and $T_{i\perp}/T_{e\perp} = 2$. Cases 1 and 2 are shown in Figures 17 and 18, respectively. In Figure 17, the grey box corresponds to the bounds of data point 1 from Table I. Similarly, in Figure 18, the grey box corresponds to the bounds of data point 2 from Table I. In comparing these two figures, it is clear that they encompass generally the same regions outlined in Figure 16. This result gives some confidence in drawing conclusions from the original assumptions of complete thermal equilibrium and $\beta = 1$ for order of magnitude estimates.

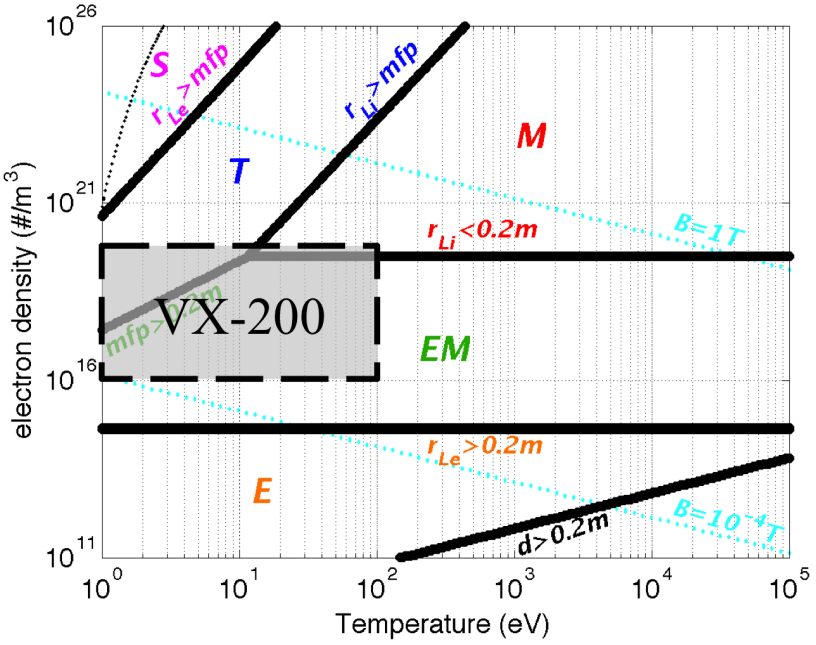

Fig. 16. Single ionized Argon, $\beta = 1$, thermal equilibrium.

From Figures 16- 18, it is seen that near the throat of the magnetic nozzle, the

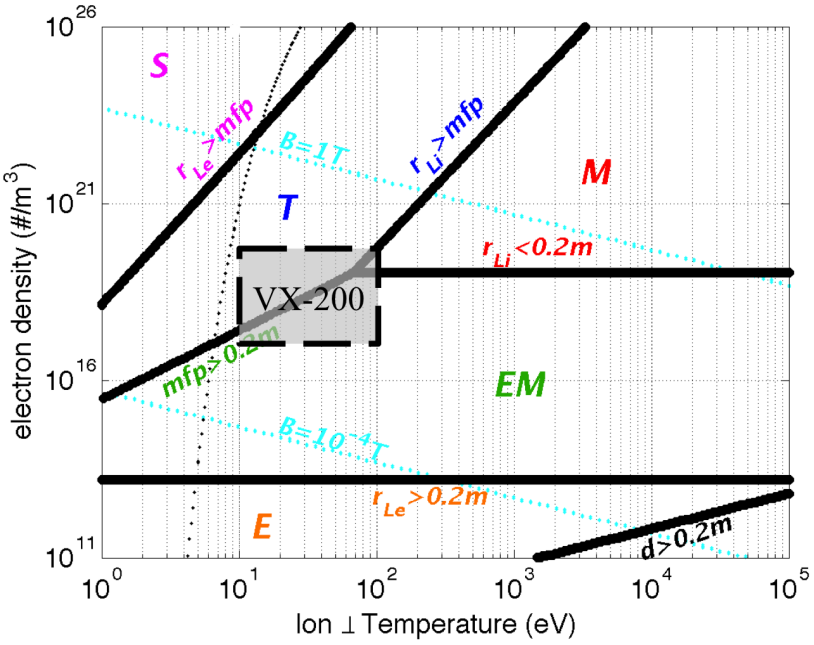

Fig. 17. Case 1: Single ionized Argon, $\beta = 0.2$, thermal nonequilibrium ($T_{i\perp}/T_{e\perp} = 10$).

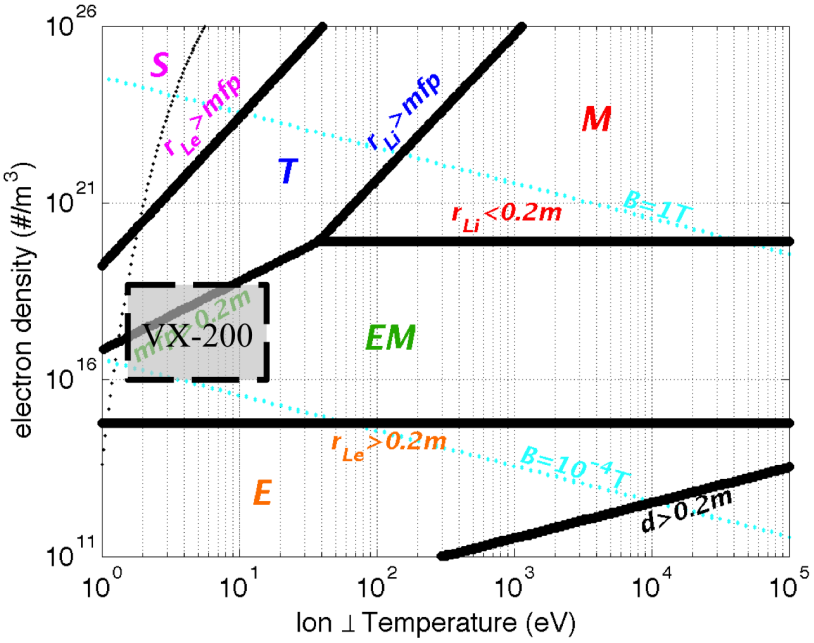

Fig. 18. Case 2: Single ionized Argon, $\beta = 2$, thermal nonequilibrium ($T_{i\perp}/T_{e\perp} = 2$).

plasma is characterized by a combination of the regions T, M, and EM and then shifts toward the EM region further downstream. This shift toward the EM region implies that the ions tend to behave more as free particles while the electrons remain bound to their cyclotron orbits downstream, and both still maintain quasineutrality. The most important conclusion from these results, however, is that a fluid approach is viable for magnetic nozzle simulations so long as care is taken to include at least tensorial resisitivity near the nozzle throat and local electric field effects further downstream.

In a fluid model, the local electric field effects are incorporated in the generalized Ohm's law, which is derived from taking moments of the electron Boltzmann equation. As mentioned in the beginning of this chapter, it is the closure of the Boltzmann moments where a majority of plasma physics is either included or neglected. In the EM region, where local electric fields become important, the Hall effect and electron pressure gradient effect are no longer negligible in general for a single fluid MHD model. Electron inertia may also be important, which leads to a "two-fluid" model, one for the ions and one for the electrons. For detachment physics, it is unknown if the characteristic frequency of the phenomenon is negligible compared to the ion cyclotron frequency, so the Hall effect cannot be ruled out immediately. More simulation and experimental work is needed to determine which effects should be included. For the current simulation work, this analysis suggests that a two-fluid model would be the most comprehensive for capturing the physics in the VX-200 plume, though still not as accurate as a fully kinetic description. Also, a single-fluid model including tensorial resistivity could perhaps be sufficient.

C. Chapter Summary

In this chapter, the parameter regimes of a fluid model for a single, fully-ionized Argon plasma were examined. The purpose of this analysis was to evaluate the appropriate fluid assumptions required for a magnetic nozzle simulation. For preliminary VX-200 nozzle analysis, this work suggests that a single-fluid MHD model including tensorial resistivity is an acceptable first approach. It was also shown that local electric field effects tend to become dominant further downstream in the VX-200 nozzle. It is known that in order to produce thrust, the plasma bearing the axial kinetic energy must eventually detach from the VX-200 device. However, a comprehensive understanding of the detachment process is lacking. Due to this uncertainty and the importance of local electric field effects, it was concluded that a two-fluid model would be the most appropriate fluid approach for capturing the physics in the VX-200 plume. The next chapter details the new GKM-MHD numerical tool that will eventually be applied to study magnetic nozzle flows, such as those of the VX-200.

CHAPTER IV

GAS-KINETIC METHOD FOR RESISTIVE MHD

The Gas-Kinetic Method (GKM) is a finite volume numerical scheme for solving the Navier-Stokes equations. It is a hybrid of fluid and kinetic methods originally developed by Xu [22] for shock capturing in high Mach number flows, but has since been shown to be very effective even at weakly compressible limits [23]. The "fluid" part of the method comes from the fact that the macroscopic properties (i.e. mass, momentum, energy) are cell-volume-averaged quantities that are evolved in time by computing fluxes at cell interfaces. The "kinetic" part of the method comes from how these fluxes are calculated, by explicitly taking moments of a particle distribution function. This chapter details the specifics of the gas-kinetic method for solving the Navier-Stokes equations and then explains how the method is extended for single-fluid MHD. The current scheme has been benchmarked with the inclusion of scalar plasma resistivity, but is flexible enough to later include other non-ideal MHD effects such as Hall physics, electron pressure, and eventually, multi-species physics.

A. Boltzmann-BGK Navier-Stokes Solver

The derivation of the numerical scheme for solving the Navier-Stokes equations by the gas-kinetic method follows the arguments given by Xu [22]. The Boltzmann BGK (BBGK) equation with no external forces or other source terms is the starting point for the derivation, and for simplicity is 1-D. The kinetic description of a gas was introduced in Section C of Chapter II, and the BGK approximation is defined in Section A of Chapter III. The BBGK equation is rewritten here for clarity:

$$\frac{\partial f}{\partial t} + u\frac{\partial f}{\partial x} = \frac{g - f}{\tau} \tag{4.1}$$

The relation between the macroscopic variables and the particle distribution function is the following:

$$\begin{pmatrix} \rho \\ \rho U \\ E \end{pmatrix} = \int_{-\infty}^{\infty} \begin{pmatrix} 1 \\ u \\ \frac{1}{2}(u^2 + \xi^2) \end{pmatrix} f \, d\Xi \tag{4.2}$$

- ρ is the mass density (NOTE: f here has units of $\frac{kg\ s^3}{m^6}$)
- U is the macroscopic fluid velocity, and u is the microscopic particle velocity.
- $E = \frac{1}{2}\rho(u^2 + \frac{N+3}{2\lambda})$ is the total energy density (sum of kinetic and thermal energy densities). $N = \frac{5-3\gamma}{\gamma-1}$, where γ is the ratio of specific heats. $\lambda = \frac{m}{2kT}$.
- ξ is an internal variable that has K total degrees of freedom and N internal degrees of freedom (such as from rotation and vibration). For 1D flow $K = N + 2$, 2D flow $K = N + 1$, and 3D flow $K = N$.
- $\xi^2 = \xi_1^2 + \xi_2^2 + ... + \xi_K^2$
- $d\Xi = du d\xi$ is the volume element in phase space with $d\xi = d\xi_1 d\xi_2 ... d\xi_K$.

The nonequilibrium distribution function f can be approximated by the Chapman-Enskog expansion. The Chapman-Enskog expansion is a Taylor series expansion of a particle distribution function that is slightly perturbed from a Maxwellian distribution, with the small parameter being the collisional relaxation time τ. To first order, the expansion is given as the following:

$$f = g - \tau \left(\frac{\partial g}{\partial t} + u \frac{\partial g}{\partial x} \right) \tag{4.3}$$

Substituting equation 4.3 into equation 4.1 gives the following:

$$\left(\frac{\partial g}{\partial t} - \tau \left[\frac{\partial^2 g}{\partial t^2} + u \frac{\partial^2 g}{\partial t \partial x} \right] \right) + u \left(\frac{\partial g}{\partial x} - \tau \left[\frac{\partial^2 g}{\partial t \partial x} + u \frac{\partial^2 g}{\partial x^2} \right] \right) = \frac{g - f}{\tau} \tag{4.4}$$

Upon rearranging and defining $\psi \equiv [1, u, \frac{1}{2}(u^2 + \xi^2)]^T$, the moments of equation 4.4 are given as:

$$\int \left(\frac{\partial g}{\partial t} + u \frac{\partial g}{\partial x} \right) \psi \, d\Xi - \int \tau \left(\frac{\partial^2 g}{\partial t^2} + 2u \frac{\partial^2 g}{\partial t \partial x} + u^2 \frac{\partial^2 g}{\partial x^2} \right) \psi \, d\Xi = 0 \tag{4.5}$$

The Navier-Stokes equations are obtained from equation 4.5, and in 1-D for a monatomic gas they are written as the following:

$$\frac{\partial}{\partial t} \begin{pmatrix} \rho \\ \rho U \\ E \end{pmatrix} + \frac{\partial}{\partial x} \begin{pmatrix} \rho U \\ \rho U^2 + p \\ (E + p)U \end{pmatrix} = \frac{\partial}{\partial x} \begin{pmatrix} 0 \\ \frac{4}{3} \mu \frac{\partial U}{\partial x} \\ \frac{5}{4} \mu \frac{\partial}{\partial x} \left(\frac{1}{\lambda} \right) + \frac{4}{3} \mu U \frac{\partial U}{\partial x} \end{pmatrix} \tag{4.6}$$

Here the total energy density is $E = \frac{1}{2}\rho(U^2 + \frac{3}{2\lambda})$, pressure is $p = \rho/2\lambda$, and $\mu = \tau p$ is the dynamic viscosity coefficient. Theoretically, "the physical content in the BGK model is far richer than the Navier-Stokes equations, especially in a rarefied regime [22]." One key benefit of using a BGK formulation is that there are no constitutive relations. The transport properties such as kinematic viscosity and thermal conductivity are derived from kinetic theory rather than empirical algebraic relations.

The finite volume formulation of the fluid equations is given as the following:

$$\frac{\partial}{\partial t} \int \begin{pmatrix} \rho \\ \rho U \\ E \end{pmatrix} d\Omega + \oint \begin{pmatrix} \mathbf{F}_\rho \\ \mathbf{F}_{\rho U} \\ \mathbf{F}_E \end{pmatrix} \cdot \, d\mathbf{A} = 0 \tag{4.7}$$

where Ω is the control volume, A is the surface of the control volume, and $\mathbf{F}$ is the flux. In 1-D, equation 4.7 becomes

$$\frac{\partial}{\partial t} \int \begin{pmatrix} \rho \\ \rho U \\ E \end{pmatrix} dx + \Big(\mathbf{F}(x_{i+\frac{1}{2}}, t) - \mathbf{F}(x_{i-\frac{1}{2}}, t) \Big) = 0 \tag{4.8}$$

where the flux across the $i + 1/2$ cell interface is given by

$$\mathbf{F}(x_{i+1/2}, t) = \begin{pmatrix} F_\rho \\ F_{\rho U} \\ F_E \end{pmatrix} = \int_{-\infty}^{\infty} u \begin{pmatrix} 1 \\ u \\ \frac{1}{2}(u^2 + \xi^2) \end{pmatrix} f(x_{i+1/2}, t, u, \xi)\, d\Xi \tag{4.9}$$

For reference, a schematic of the computational domain is shown in Figure 19. The "L" and "R" represent the left and right of the $i + \frac{1}{2}$ cell-interface, respectively.

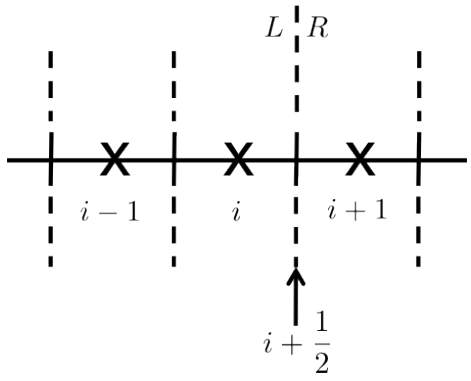

Fig. 19. 1-D computational domain.

Integrating equation 4.8 over a single time step leads to the following equation:

$$\begin{pmatrix} \rho(t + \triangle t) \\ \rho U(t + \triangle t) \\ E(t + \triangle t) \end{pmatrix} - \begin{pmatrix} \rho(t) \\ \rho U(t) \\ E(t) \end{pmatrix} = -\frac{1}{\triangle x} \int_t^{t+\triangle t} \Big(\mathbf{F}(x_{i+\frac{1}{2}}, t) - \mathbf{F}(x_{i-\frac{1}{2}}, t) \Big)\, dt \tag{4.10}$$

For completeness, it can be shown that equation 4.10 is derived by multiplying the BBGK equation by $\psi \equiv [1, u, \frac{1}{2}(u^2 + \xi^2)]^T$ and integrating over velocity space, cell volume, and time, but this is not done here. The semidiscretized form of equation

4.10 is given as follows:

$$\begin{pmatrix} \rho \\ \rho U \\ E \end{pmatrix}_i^{n+1} = \begin{pmatrix} \rho \\ \rho U \\ E \end{pmatrix}_i^{n} - \frac{1}{x_{i+\frac{1}{2}} - x_{i-\frac{1}{2}}} \int_t^{t+\triangle t} \Big(\mathbf{F}(x_{i+\frac{1}{2}}, t) - \mathbf{F}(x_{i-\frac{1}{2}}, t) \Big)\, dt \qquad (4.11)$$

where the subscript i refers to the cell center and the superscript n is the time step.

In general, there are three stages to the GKM. First, in the "reconstruction" stage, a piecewise continuous flow distribution inside each cell is obtained. In other words, the cell-centered values are extrapolated and connected to other cell centers in a piecewise continuous way using special slope techniques called "limiters." An example of a linear reconstruction of density is shown in Figure 20. The current version of the Texas A&M GKM code uses a nonlinear Weighted Essentially Non-Oscillatory (WENO) limiter. Next, in the "gas evolution" stage, a time-dependent flux $\mathbf{F}$ is calculated at cell interfaces. Finally, in the "projection" stage, the cell-centered macroscopic properties are updated according to equation 4.11.

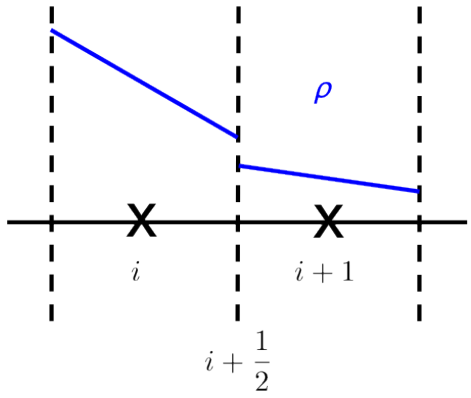

Fig. 20. Piecewise linear reconstruction of density.

The bulk of the computational effort for the GKM numerical scheme is spent calculating the time-dependent fluxes. The first step in obtaining the fluxes is to

examine the formal integral solution to the BBGK equation. This solution defines the nonequilibrium distribution function f, and at a given cell interface it is given as the following:

$$f(x_{i+1/2},t,u,\xi) = \frac{1}{\tau}\int_0^t g(x',t',u,\xi)e^{-(t-t')/\tau}\,dt' + e^{-t/\tau}f_0(x_{i+1/2}-ut) \tag{4.12}$$

The only unknowns in equation 4.12 are g, which is the equilibrium distribution function, and f_0, which is the initial gas distribution at the beginning of each time step. A pictorial representation of a linear reconstruction of f_0 and g is shown in Figure 21. The nonequilibrium distribution function f is a nonlinear combination of f_0 and g. Xu [22] provides details of how to uniquely approximate g and f_0 from the

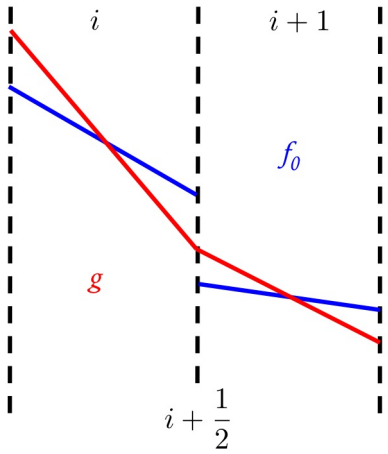

Fig. 21. f_0 and g.

macroscopic quantities, and the end result is the following:

$$f_0(x) = \left\{ \begin{array}{l} g^l\left[1+a^l(x-x_{i+1/2})-\tau(a^lu+A^l)\right];\ x \le x_{i+1/2} \\ g^r\left[1+a^r(x-x_{i+1/2})-\tau(a^ru+A^r)\right];\ x \ge x_{i+1/2} \end{array} \right\} \tag{4.13}$$

$$g(x) = \left\{ \begin{array}{l} g_0 \left[1 + \bar{a}^l (x - x_{i+1/2}) + \bar{A}t)\right];\ x \leq x_{i+1/2} \\ g_0 \left[1 + \bar{a}^r (x - x_{i+1/2}) + \bar{A}t)\right];\ x \geq x_{i+1/2} \end{array} \right\} \tag{4.14}$$

Here g^l, g^r, and g_0 are Maxwellian distributions based on macroscopic quantities left, right, and at the cell interface, respectively. The a^l, a^r, $\bar{a}^l$, and $\bar{a}^r$ variables represent spatial derivatives of a Maxwellian distribution. Similarly, the A^l, A^r, and $\bar{A}$ variables are temporal derivatives of a Maxwellian distribution. Substituting equation 4.13 and 4.14 into equation 4.12 gives the following analytical approximation for f:

$$\begin{aligned} f(x_{i+\frac{1}{2}}, t, u, \xi) &= g_0(1 - e^{-t/\tau}) \\ &+ \left[te^{-t/\tau} + \tau(e^{-t/\tau} - 1)\right] \left(H(u)\bar{a}^l + (1 - H(u))\bar{a}^r\right) g_0 u \\ &+ \tau g_0 \bar{A} \left[t/\tau - 1 + e^{-t/\tau}\right] \\ &+ e^{-t/\tau} g^l H(u) \left[1 - u(t + \tau)a^l\right] \\ &+ e^{-t/\tau} g^r (1 - H(u)) \left[1 - u(t + \tau)a^r\right] \\ &+ e^{-t/\tau} \left[-\tau A^l H(u) g^l - \tau A^r (1 - H(u)) g^r\right] \end{aligned} \tag{4.15}$$

where H is the Heaviside step function. The variable $\bar{A}$ is the only unknown in equation 4.15, but can be found by integrating what Xu calls the "conservation constraint" at $x_{i+1/2}$ over the time step as follows:

$$\int_0^{\triangle t} \int (g - f)\psi \, dt d\Xi = 0 \tag{4.16}$$

Equation 4.16 is just another mathematical representation of the conservation of mass, momentum, and energy.

With the analytical expression for f given by equation 4.15, the fluxes may now be expressed analytically by carrying out the integration in equation 4.9. In the numerical implementation of this flux calculation, it is the analytical expression of the fluxes after integration that is actually written into the code. One final important point is that in the GKM, the distribution function is determined uniquely from the

macroscopic quantities by carrying information at each time step from the previous time step through the variable f_0.

B. Addition of Resistive MHD Physics

Assuming SI units, the resistive MHD equations including the effects of compressibility and viscous dissipation can be written in conservative form as the following (note that $\mathbf{v}$ is now the macroscopic velocity):

Conservation of Mass:

$$\frac{\partial \rho}{\partial t} = -\nabla \cdot (\rho \mathbf{v}) \tag{4.17}$$

Conservation of Momentum:

$$\frac{\partial \rho \mathbf{v}}{\partial t} = -\nabla \cdot \left[\rho \mathbf{v} \otimes \mathbf{v} + \underline{\underline{\Phi}} + \underline{\underline{I}} \left(p + \frac{\mathbf{B}^2}{2\mu_0} \right) - \frac{\mathbf{B} \otimes \mathbf{B}}{\mu_0} \right] \tag{4.18}$$

Conservation of Energy:

$$\frac{\partial E}{\partial t} = -\nabla \cdot \left[\mathbf{v} \left(E + p \right) - k \nabla T + \mathbf{v} \cdot \left(\underline{\underline{\Phi}} + \underline{\underline{I}} \frac{\mathbf{B}^2}{2\mu_0} - \frac{\mathbf{B} \otimes \mathbf{B}}{\mu_0} \right) - \frac{\mathbf{B} \times (\nabla \times \mathbf{B})}{\sigma \mu_0^2} \right] \tag{4.19}$$

Induction Equation:

$$\frac{\partial \mathbf{B}}{\partial t} = \nabla \times \left(\mathbf{v} \times \mathbf{B} - \frac{\nabla \times \mathbf{B}}{\sigma \mu_0} \right) \tag{4.20}$$

Here $\underline{\underline{\Phi}}$ is the viscous stress tensor, k is the thermal conductivity, σ is the electrical conductivity, and E is the total energy density, which is defined as:

$$E = \frac{p}{\gamma - 1} + \frac{\rho \mathbf{v^2}}{2} + \frac{\mathbf{B}^2}{2\mu_0} \tag{4.21}$$

Equations 4.17-4.20 are supplemented by equations of state for internal energy and pressure, and also the divergence of the magnetic field constraint, i.e. $\nabla \cdot \mathbf{B} = 0$, from Maxwell's equations of electromagnetism. Equations 4.17-4.20 also implicitly assume

the following form of Ohm's Law:

$$\mathbf{j} = \sigma \left(\mathbf{E} + \mathbf{v} \times \mathbf{B} \right) \tag{4.22}$$

which relates the electromagnetic field quantities to the current density and bulk fluid velocity. The induction equation is derived by taking the curl of equation 4.22, and substituting the following two of Maxwell's equations (neglecting displacement current):

$$\nabla \times \mathbf{B} = \mathbf{j}\mu_0; \qquad \nabla \times \mathbf{E} = -\frac{\partial \mathbf{B}}{\partial t} \tag{4.23}$$

In the absence of $\mathbf{B}$, equations 4.17-4.21 reduce to the more familiar Navier-Stokes equations. In the original GKM code, the BGK formulation of the Navier-Stokes equations is solved in its conservative form as was shown in Section A (cf. equation 4.6). Xu [25] and later Tang [24] have shown that it is possible to extend the gas-kinetic scheme for the ideal MHD equations, i.e. neglecting resistivity and viscous dissipation. However, as mentioned in the introduction, there is no clear solution to extending this work by including non-ideal MHD effects. The core advantage to the GKM scheme is in its use of moments of the particle distribution function to obtain rich macroscopic information. There is no such physical moment of a particle distribution function to give the magnetic field. Dellar [41] used a semi-empirical method to obtain a separate vector distribution function for calculating the components of the magnetic field in LBM-MHD. However, this method is not based on any physical laws of kinetic theory, though it does give encouraging results.

The approach of this thesis to solving the resistive MHD equations is to separate them into "hydrodynamic" and "magnetic" parts. The logic of this approach is to ensure that the current GKM algorithm that solves the hydrodynamic equations, which has already been parallelized and thoroughly tested, needs no major modification.

Instead, it only needs to be supplemented by adding magnetic source terms and an evolution equation. Fuchs et al. [31] approached solving the ideal MHD equations in a similar manner. They remarked that "the MHD equations can be thought of as a combination of fluid dynamics coupled with magnetic fields." In their work, they use the "physical" splitting of the ideal MHD equations into a "hydrodynamic and a magnetic" part. This splitting gives them the freedom to compare different combinations of finite volume schemes for the mass, momentum, and energy equations and the induction equation independently.

In splitting the resistive MHD equations, the mass conservation equation (4.17) remains the same. The momentum equation (4.18) is already in a form that is naturally separable and can be rearranged to give the following:

$$\frac{\partial \rho \mathbf{v}}{\partial t} + \nabla \cdot \left[\rho \mathbf{v} \otimes \mathbf{v} + \underline{\underline{\Phi}} + \underline{\underline{I}} p \right] = \mathbf{j} \times \mathbf{B} \tag{4.24}$$

The energy equation (4.19) requires more work to rearrange. First, note that the magnetic field terms in the energy equation can be written in a more general form:

$$\frac{\partial E}{\partial t} = -\nabla \cdot \left[\mathbf{v} \left(\frac{\rho \mathbf{v^2}}{2} + \frac{p}{\gamma - 1} + p \right) - k \nabla T + \mathbf{v} \cdot \underline{\underline{\Phi}} + \frac{\mathbf{E} \times \mathbf{B}}{\mu_0} \right] \tag{4.25}$$

Substituting Ohm's law (4.22) into equation 4.25 returns it to the form given in equation 4.19. Next, examining the terms that only involve the electromagnetic fields in equation 4.25, and temporarily ignoring the fluid terms, gives the following:

$$\frac{\partial}{\partial t} \left(\frac{\mathbf{B}^2}{2\mu_0} \right) = -\nabla \cdot \left[\frac{\mathbf{E} \times \mathbf{B}}{\mu_0} \right] \tag{4.26}$$

Using a vector identity and taking the derivative of the left-hand-side gives:

$$\frac{\mathbf{B}}{\mu_0} \cdot \frac{\partial \mathbf{B}}{\partial t} = -\frac{\mathbf{B}}{\mu_0} \cdot (\nabla \times \mathbf{E}) + \mathbf{E} \cdot \frac{(\nabla \times \mathbf{B})}{\mu_0} \tag{4.27}$$

Now substituting both Ohm's law and equation 4.23 gives the following:

$$\frac{\mathbf{B}}{\mu_0}\cdot\frac{\partial\mathbf{B}}{\partial t}=-\frac{\mathbf{B}}{\mu_0}\cdot\left(-\frac{\partial\mathbf{B}}{\partial t}\right)+\left[\frac{\nabla\times\mathbf{B}}{\mu_0\sigma}-\mathbf{v}\times\mathbf{B}\right]\cdot\frac{(\nabla\times\mathbf{B})}{\mu_0} \tag{4.28}$$

It is now clear that the time dependence of the magnetic field is no longer explicit in the energy equation by the cancelation of the left-hand-side term with the first term on the right-hand-side of equation 4.28. This just means that the energy equation is no longer in its purely conservative form, and after more work it can be shown that the remaining terms can be rewritten as follows:

$$\left[\frac{\nabla\times\mathbf{B}}{\mu_0\sigma}-\mathbf{v}\times\mathbf{B}\right]\cdot\frac{(\nabla\times\mathbf{B})}{\mu_0}=\mathbf{j}\cdot\left(\frac{\mathbf{j}}{\sigma}-\mathbf{v}\times\mathbf{B}\right) \tag{4.29}$$

or

$$\left[\frac{\nabla\times\mathbf{B}}{\mu_0\sigma}-\mathbf{v}\times\mathbf{B}\right]\cdot\frac{(\nabla\times\mathbf{B})}{\mu_0}=\mathbf{j}\cdot\mathbf{E} \tag{4.30}$$

Now the final form of the energy equation with the separated hydrodynamic and magnetic parts is given as the following:

$$\frac{\partial E_h}{\partial t}+\nabla\cdot\left[\mathbf{v}\left(E_h+p\right)-k\nabla T+\mathbf{v}\cdot\underline{\underline{\Phi}}\right]=\frac{\mathbf{j}^2}{\sigma}+\mathbf{v}\cdot(\mathbf{j}\times\mathbf{B}) \tag{4.31}$$

where now E_h is the total hydrodynamic energy density $E_h=\dfrac{p}{\gamma-1}+\dfrac{\rho\mathbf{v^2}}{2}$.

C. Current Implementation

The resistive MHD equations implemented into the existing GKM code were given in the last section but are summarized here for clarity:

$$\begin{aligned}
\frac{\partial \rho}{\partial t} + \nabla \cdot (\rho \mathbf{v}) &= 0 \\
\frac{\partial (\rho \mathbf{v})}{\partial t} + \nabla \cdot \left[\rho \mathbf{v} \otimes \mathbf{v} + \underline{\underline{\Phi}} + \underline{\underline{I}} p \right] &= \frac{\nabla \times \mathbf{B}}{\mu_0} \times \mathbf{B} \\
\frac{\partial E_h}{\partial t} + \nabla \cdot \left[\mathbf{v} \left(E_h + p \right) - k \nabla T + \mathbf{v} \cdot \underline{\underline{\Phi}} \right] &= \frac{(\nabla \times \mathbf{B})^2}{\sigma \mu_0^2} + \mathbf{v} \cdot \left(\frac{\nabla \times \mathbf{B}}{\mu_0} \times \mathbf{B} \right) \\
\frac{\partial \mathbf{B}}{\partial t} &= \nabla \times \left(\mathbf{v} \times \mathbf{B} - \frac{\nabla \times \mathbf{B}}{\sigma \mu_0} \right)
\end{aligned} \tag{4.32}$$

In this form, the magnetic field terms are treated as source terms in the momentum and energy equations and evolved in time by the induction equation. A new MHD subroutine was added to the code to calculate the right-hand-side terms of the above equations by a second-order central-difference scheme. The magnetic field is evolved in time by a first-order forward-difference scheme, which is the same time-marching scheme currently in place for the other conserved variables. Thus, given the initial and boundary values of density, momentum, energy, and total magnetic field, the GKM-MHD code marches forward in time explicitly to give the new values of these variables.

D. Extension to Hall MHD

For the inclusion of Hall effect physics in addition to resistivity, the only change to the MHD equations is through an additional term in Ohm's law, which is the following:

$$\mathbf{j} = \sigma \left(\mathbf{E} + \mathbf{v} \times \mathbf{B} - \frac{\nabla \times \mathbf{B}}{n_e e \mu_0} \times \mathbf{B} \right) \tag{4.33}$$

where n_e is the electron number density ($n_e \approx \rho/m_i$) and e is the electron charge. The inclusion of the Hall term in Ohm's law results in the following resistive Hall MHD equations:

$$\begin{aligned}
\frac{\partial \rho}{\partial t} + \nabla \cdot (\rho \mathbf{v}) &= 0 \\
\frac{\partial (\rho \mathbf{v})}{\partial t} + \nabla \cdot \left[\rho \mathbf{v} \otimes \mathbf{v} + \underline{\underline{\Phi}} + \underline{\underline{I}} p \right] &= \mathbf{j} \times \mathbf{B} \\
\frac{\partial E_h}{\partial t} + \nabla \cdot \left[\mathbf{v} \left(E_h + p \right) - k \nabla T + \mathbf{v} \cdot \underline{\underline{\Phi}} \right] &= \mathbf{j} \cdot \left[\frac{\mathbf{j}}{\sigma} - \mathbf{v} \times \mathbf{B} + \frac{\mathbf{j} \times \mathbf{B}}{n_e e} \right] \\
\frac{\partial \mathbf{B}}{\partial t} &= \nabla \times \left[\mathbf{v} \times \mathbf{B} - \frac{\mathbf{j}}{\sigma} - \frac{\mathbf{j} \times \mathbf{B}}{n_e e} \right]
\end{aligned} \tag{4.34}$$

The above equations are solved in the same manner as described for the resistive MHD equations. The only difference is that there are additional source terms that need to be calculated by the central difference scheme.

E. Chapter Summary

In this chapter, the numerical scheme used in the GKM Navier-Stokes code was derived and extended to include resistive MHD physics. The magnetic terms are effectively included as source terms by splitting the conservative system of equations into its physical hydrodynamic and magnetic parts. The new magnetic terms, in-

cluding the magnetic evolution equation, are solved by a new MHD subroutine in the code that calculates derivatives by central finite differences. The new GKM-MHD code includes scalar resistivity, but is flexible enough to include Hall physics with an additional term from the generalized Ohm's Law. The validation results for this new resistive MHD flow solver are presented in the next chapter.

CHAPTER V

CHANNEL FLOW SIMULATIONS

In this chapter and the next, several resistive MHD flows of increasing complexity are simulated using the GKM-MHD code introduced in Chapter IV. One goal of this chapter is to benchmark changes to the code by comparing computational results with known analytical MHD solutions. Another aim is to demonstrate the capability of the code to produce known MHD phenomena such as the effects of varying magnetic Reynolds number and Hartmann number on canonical channel flows. All simulations in this chapter assume weak compressibility (i.e. Mach number $<< 1$) in order to match known analytical solutions that assume incompressible flow. The GKM-MHD code is a fully compressible code. However, to limit the scope of this work, no attempt was made to examine compressible MHD flows.

A. High Performance Computing

The GKM-MHD code was successfully tested for up to 512 cores (1024 on Pleiades) using resources at the following High Performance Computing (HPC) facilities:

1. The NASA SGI ICE cluster known as "Pleiades." This system currently has a total of 111,104 processing cores and a theoretical peak performance of 1.3 PetaFLOPS (1.3×10^{15} Floating Point Operations Per Second). Specifically, the "Harpertown" nodes were used for this thesis research. Each Harpertown node has two 3GHz quad-core Intel Xeon E5472 (Harpertown) processors with 1GB of memory per core.

2. The Texas Advanced Computing Center (TACC) Sun constellation Linux Cluster known as "Ranger." This machine currently has 62,976 processing cores

that are divided into 16-core nodes. Each node has four 2.3 GHz quad-core AMD Opteron processors that share 32 GB of memory. It has a theoretical peak performance of 579 TeraFLOPS.

3. The National Institute for Computational Sciences (NICS) Cray XT5 Linux Cluster called "Kraken." This system has a theoretical peak performance of 1.17 PetaFLOPS with 112,896 processing cores that are divided into 12-core nodes. Each node has two 2.6 GHz hex-core AMD Opteron processors (Istanbul) and 16 GB of memory.

The success of testing on these machines at least demonstrates the code's portability and potential for performing very large computations. However, no attempt was made to optimize performance of the code on any of the machines. Unless otherwise stated, the computational results presented in this thesis were obtained from simulations on Pleiades.

B. 1-D MHD Couette Flow

The first benchmark is a simple 1-D channel flow problem called MHD Couette flow and is taken from Sutton [40]. This channel flow is a modified version of the classical Couette flow[42] but for an electrically conducting fluid with a constant magnetic field applied to it. The linear velocity profile for the steady state solution of the classical Couette problem is depicted in Figure 22. Here a shear flow between two infinitely wide parallel walls is maintained by a moving top wall and a stationary bottom wall, both with no-slip boundary conditions. The problem is considered 1-D because changes to the flow occur only in the z direction and are self-similar in both the y and x directions.

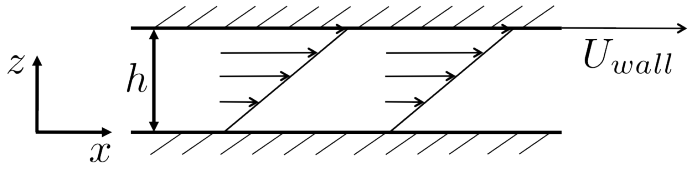

Fig. 22. Steady-state Couette flow.

If the flow is assumed to be electrically conducting, and a uniform magnetic field B_0 is applied to it in the z direction, then an analytical steady state solution exists for the resistive MHD equations that govern the flow. Assuming that the walls are perfectly insulated, the steady state analytical solution for the velocity ($\mathbf{v} = [u(z), 0, 0]$) and the magnetic field ($\mathbf{B} = [b_x(z), 0, B_0]$) are given by the following equations:

$$u(z) = U_w \left[1 - \frac{sinh\left(Ha\left(1 - \frac{z}{h}\right)\right)}{sinh(Ha)} \right] \tag{5.1}$$

$$b_x(z) = B_0 Re_m \left[\frac{coth(Ha)}{Ha} - \frac{cosh\left(Ha\left(1 - \frac{z}{h}\right)\right)}{Ha\ sinh(Ha)} \right] \tag{5.2}$$

where Re_m is the magnetic Reynolds number and Ha is the Hartmann number:

$$Ha^2 = \frac{\sigma B_0^2 h^2}{\mu}; \qquad Re_m = \mu_0 \sigma U_w h$$

The top (moving) wall velocity is U_w, h is the channel height, σ is the electrical conductivity, and μ is the dynamic viscosity. Also, note that $0 \leq z \leq h$.

The transient MHD Couette problem is solved by the GKM-MHD code with the initial conditions provided in Table II. The computational grid is 64 x 4 x 128, which represents the number of uniformly distributed cells in the cartesian x, y, and z directions, respectively. Periodic boundary conditions are assumed in the x and y directions and no-slip in the z direction. Additionally, the boundary conditions for the induced magnetic field are $b_x(x, y, 0) = 0$ and $db_x/dz(x, y, h) = 0$. The nondi-

mensional parameters introduced in Table II are the Mach number, M, Reynolds number, Re, and interaction parameter, N. These parameters are defined for the MHD Couette flow as the following:

$$M = \frac{U_w}{\sqrt{\gamma RT}}; \qquad Re = \frac{\rho U_w h}{\mu}; \qquad N = \frac{Ha^2}{Re}$$

Table II. MHD Couette flow simulation parameters.

Case	M	Re	N	Re_m	Ha
C1	0.1	40	10	10	20
C2	0.1	40	10	20	20
C3	0.1	40	10	40	20

Figures 23(a)-23(d) show the time evolution of u and b_x for case C1. The magnetic damping time [43] is given as $\tau = \rho/\sigma B_0^2$. As time progresses, the numerical solution converges toward the analytical result as expected. Compared to the classical Couette solution, there is a notable steep increase in the velocity gradient near the bottom wall. Figure 24 shows the time evolution of the volume-averaged magnetic and kinetic energy density for case C1. In Figure 24, it appears that there is a correlation between the kinetic and magnetic energies, which seem to decay to an equilibrium analogous to the motion of an underdamped harmonic oscillator.

The results for cases C2 and C3 are shown in Figures 25-28. These results show that increasing the magnetic Reynolds number increases the magnitude of the induced magnetic field. Comparing Figures 24, 26, and 28, it is evident that increasing the magnetic Reynolds number also changes how the kinetic and magnetic energies approach equilibrium. In Figure 24, the energies decay to equilibrium similar to an underdamped harmonic oscillator, and in Figure 28 the oscillations seem critically damped.

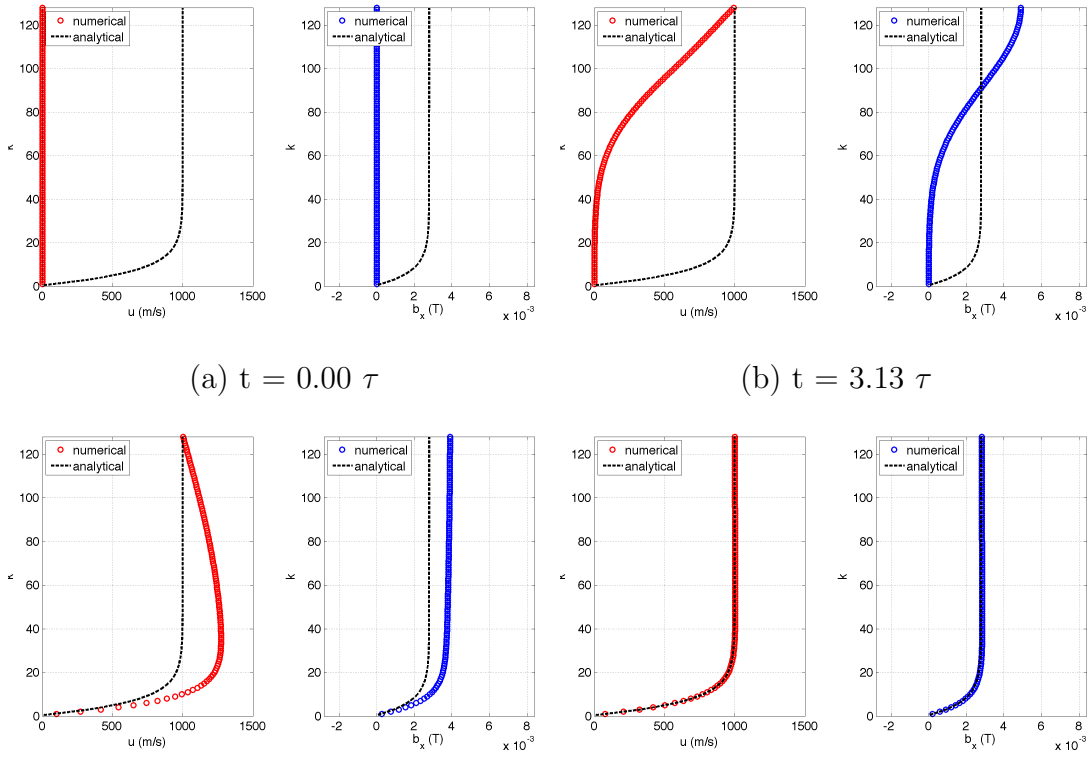

(a) t = 0.00 τ (b) t = 3.13 τ

(c) t = 18.75 τ (d) t = 68.75 τ

Fig. 23. Case C1, time evolution of MHD Couette flow.

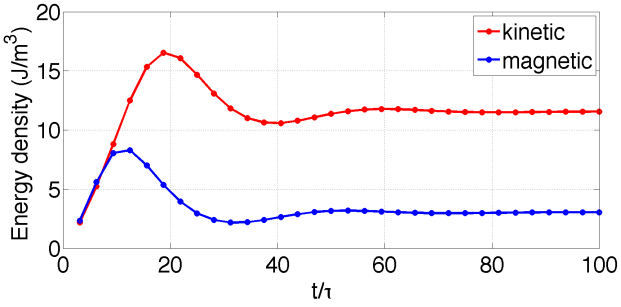

Fig. 24. Case C1, time evolution of energy density.

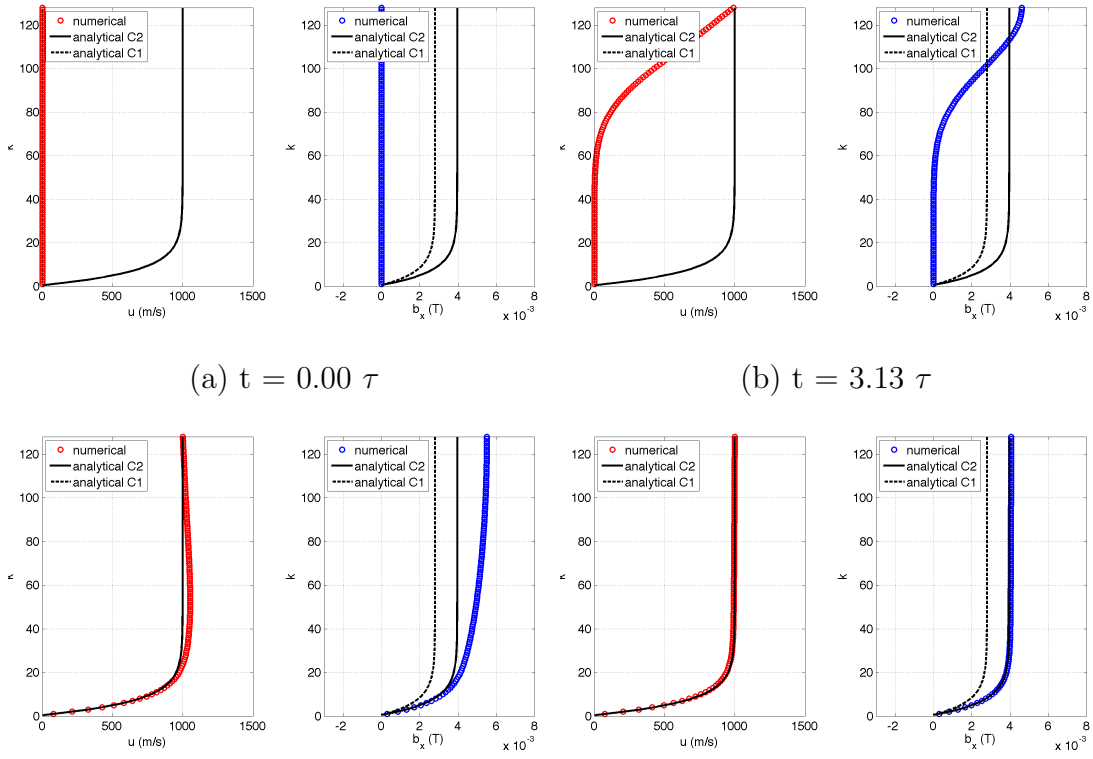

(a) t = 0.00 τ (b) t = 3.13 τ

(c) t = 18.75 τ (d) t = 68.75 τ

Fig. 25. Case C2, time evolution of MHD Couette flow.

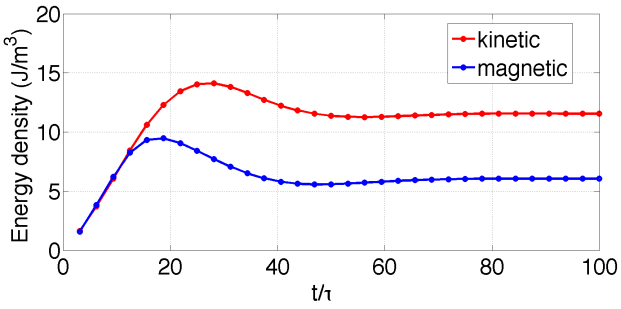

Fig. 26. Case C2, time evolution of energy density.

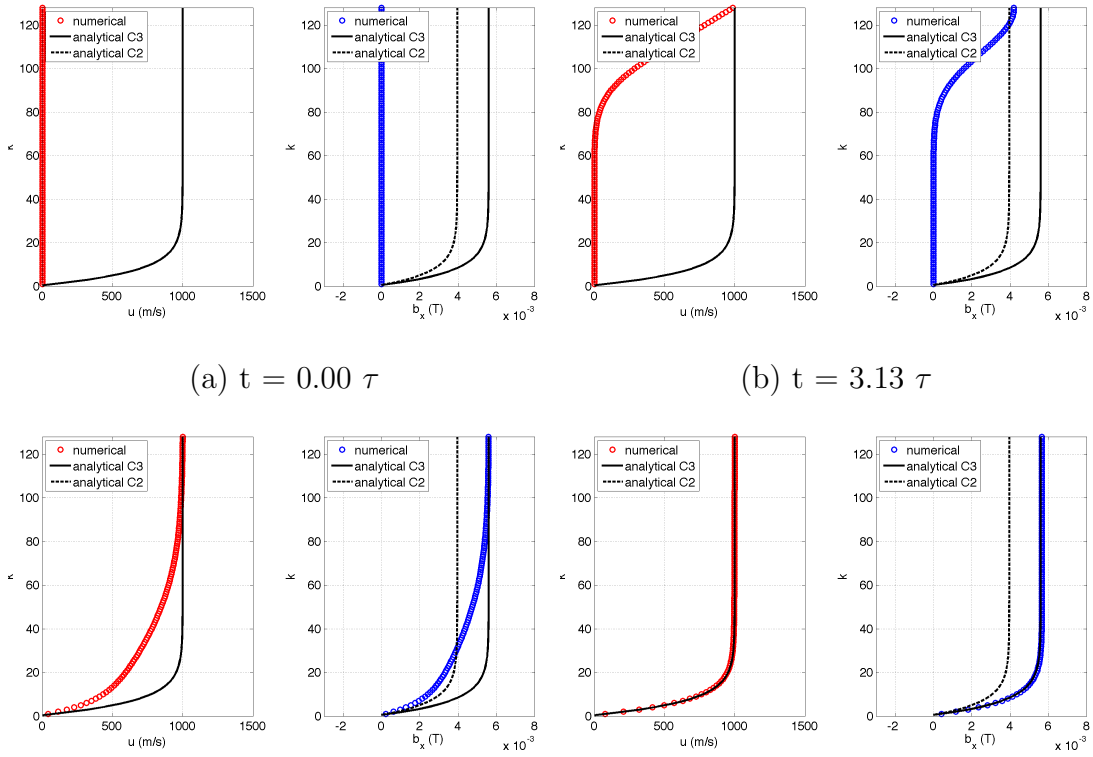

(a) t = 0.00 τ (b) t = 3.13 τ

(c) t = 18.75 τ (d) t = 68.75 τ

Fig. 27. Case C3, time evolution of MHD Couette flow.

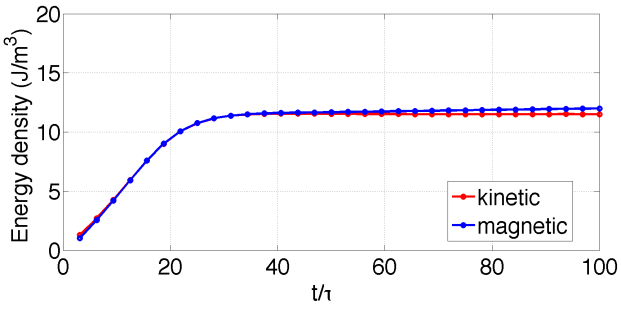

Fig. 28. Case C3, time evolution of energy density.

C. 2-D Hartmann Flow

Another MHD channel flow problem with an analytical solution is called Hartmann flow. This channel flow is a modified version of the classical Poiseuille flow [42], but for an electrically conducting fluid with a constant magnetic field applied perpendicular to the flow. The parabolic velocity profile for the steady state, fully-developed Poiseuille flow is depicted in Figure 29. Here a shear flow between two infinitely wide parallel walls is maintained by a constant pressure gradient in the x direction and no-slip boundary conditions in the z direction. For steady state and fully-developed conditions, both the Hartmann and Poiseuille flows can be considered 1-D because changes to the flow occur only in the direction perpendicular to the walls. However, the developing flow problem is 2-D with changes occurring in both the x and z directions. In this section, it is the transient, developing Hartmann flow problem that is solved using the GKM-MHD code.

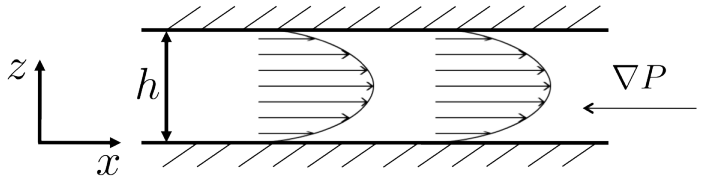

Fig. 29. Steady-state, fully-developed Poiseuille flow.

To reduce computational time, the simulations start from a fully-developed Poiseuille velocity profile with $U_{max} = 4m/s$. This is equivalent to having a very long channel divided into two sections: an upstream section without an applied magnetic field where the fluid develops into Poiseuille flow, and a downstream section with an applied magnetic field where the Poiseuille flow develops into Hartmann flow. An illustration of this is shown in Figure 30 with the computational domain

represented inside the dotted lines. Assuming the same initial density, starting from the same Poiseuille profile while increasing the Hartmann number also ensures that the mass-flow-rate is constant between simulations.

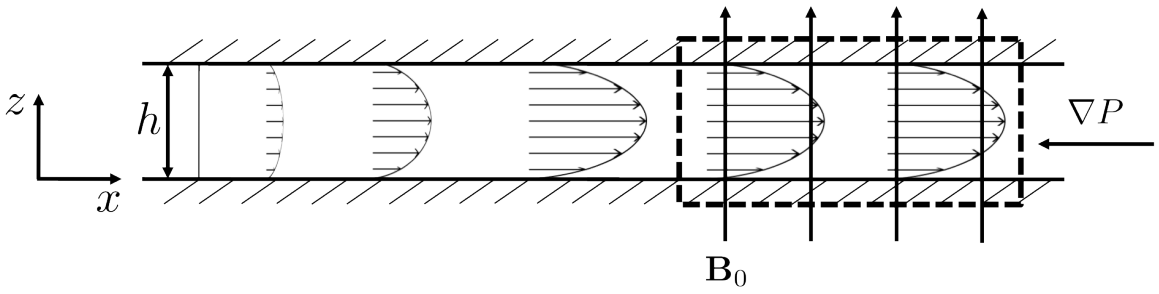

Fig. 30. Physical illustration of Hartmann simulations.

The computational grid is 512 x 4 x 64, which represents the number of cells in the x, y, and z directions, respectively. The boundary conditions are periodic in the y direction, Dirichlet inlet and zero-gradient outlet in the x direction, and no-slip, insulated walls in the z direction. The boundary conditions for the induced magnetic field are then $b_x(x, y, 0) = 0$ and $b_x(x, y, h) = 0$. The initial conditions for the Hartmann simulations are shown in Table III. The nondimensional parameters for the Hartmann flow are defined as the following:

$$M = \frac{U_{max}}{\sqrt{\gamma RT}}; \qquad Re = \frac{\rho U_{max}(h/2)}{\mu}; \qquad N = \frac{Ha^2}{Re}$$

$$Ha^2 = \frac{\sigma B_0^2 (h/2)^2}{\mu}; \qquad Re_m = \mu_0 \sigma U_{mass}(h/2)$$

where U_{mass} is a constant defined as:

$$U_{mass} = \frac{1}{h}\int_0^h U dz$$

From Sutton [40], the steady state, fully-developed analytical solutions for the velocity ($\mathbf{v} = [u(z), 0, 0]$) and the magnetic field ($\mathbf{B} = [b_x(z), 0, B_0]$) are given by the

Table III. Hartmann flow simulation parameters.

Case	M	Re	N	Re_m	Ha
H1	0.004	16.67	1.5	0.5	5
H2	0.004	66.67	1.5	0.5	10
H3	0.004	416.67	1.5	0.5	25

following equations:

$$u(z) = U_{mass} Ha \left[\frac{cosh(Ha) - cosh\left(Ha \dfrac{z}{(h/2)}\right)}{Ha\ cosh(Ha) - sinh(Ha)} \right] \tag{5.3}$$

$$b_x(z) = B_0 Re_m \left[\frac{sinh\left(Ha \dfrac{z}{(h/2)}\right) - \left(\dfrac{z}{(h/2)}\right) sinh(Ha)}{Ha\ cosh(Ha) - sinh(Ha)} \right] \tag{5.4}$$

where $-h/2 \leq z \leq h/2$.

Figures 31(a)-31(d) show the time evolution of u and b_x for case H1 at the outlet location, i.e. $i = 512$, where i, j, k are the grid locations in the x, y, z directions, respectively. As time progresses, the numerical solution converges toward the analytical result as expected. Figures 32(a) and 32(b) show a slice of u and b_x in the $x - z$ plane corresponding to Figure 31(d). This $x - z$ slice gives a picture of the spatial development of the Hartmann flow. The velocity and induced magnetic field profiles for cases H2 and H3 are shown in Figures 33 - 36(b). For case H3, the number of grid points in the z direction was increased to 128, keeping h the same, to achieve convergence. Cases H1-H3 demonstrate the effects of increasing the Hartmann number, which are to impede the flow near the center of the channel and steepen the gradients of both the velocity and induced magnetic field near the walls.

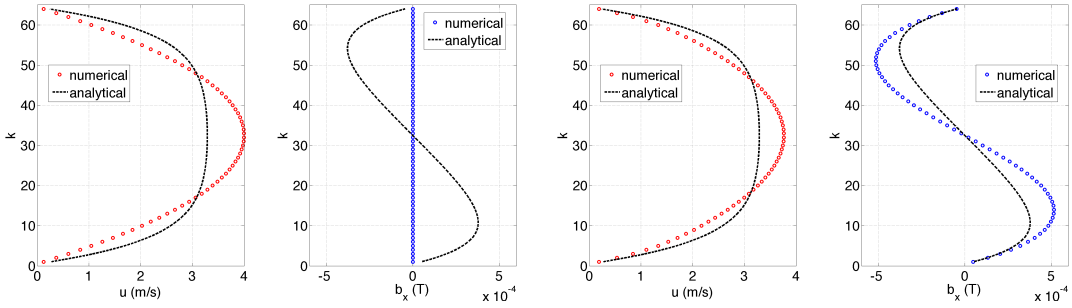

(a) $t = 0.00\tau$ (b) $t = 0.34\tau$

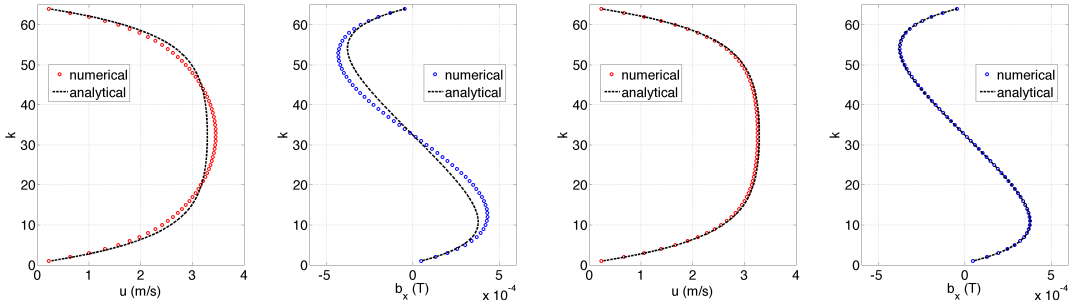

(c) $t = 0.84\tau$ (d) $t = 3.36\tau$

Fig. 31. Case H1, time evolution of Hartmann flow at outlet ($i = 512, j = 1$).

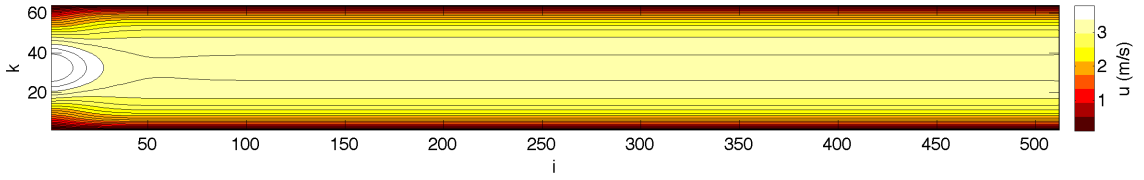

(a) Velocity, u

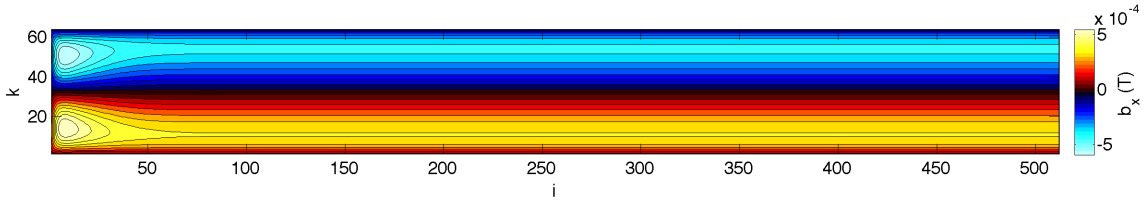

(b) Induced magnetic field, b_x

Fig. 32. Case H1, contour plots in the $x - z$ plane, $t = 3.36\tau, j = 1$.

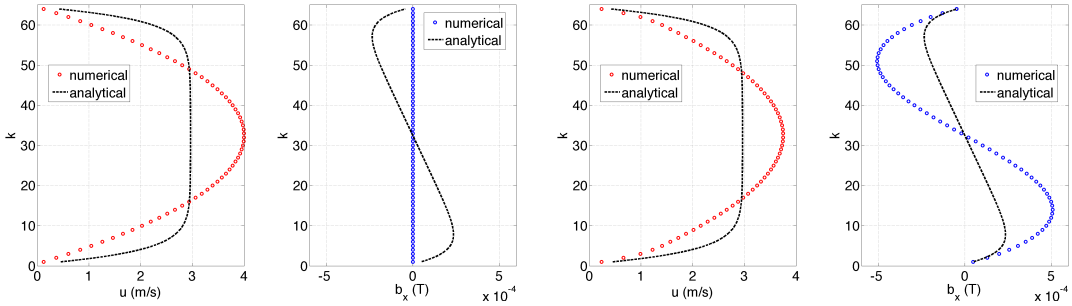

(a) $t = 0.00\tau$ (b) $t = 0.34\tau$

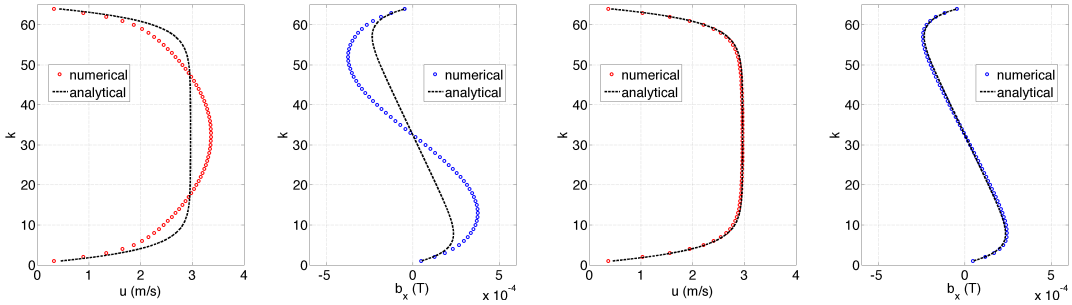

(c) $t = 0.84\tau$ (d) $t = 3.36\tau$

Fig. 33. Case H2, time evolution of Hartmann flow at outlet ($i = 512, j = 1$).

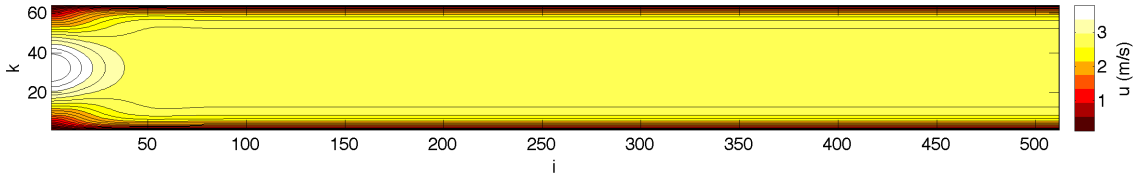

(a) Velocity, u

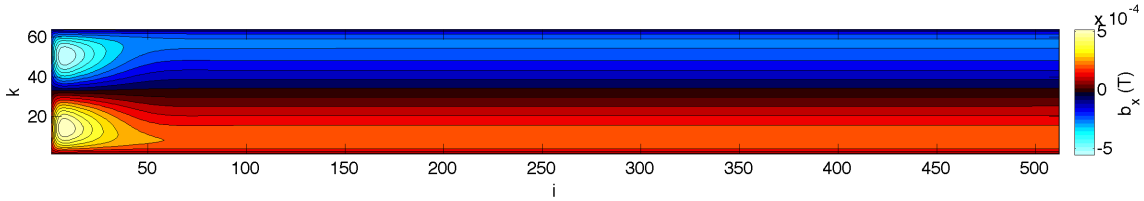

(b) Induced magnetic field, b_x

Fig. 34. Case H2, contour plots in the $x - z$ plane, $t = 3.36\tau, j = 1$.

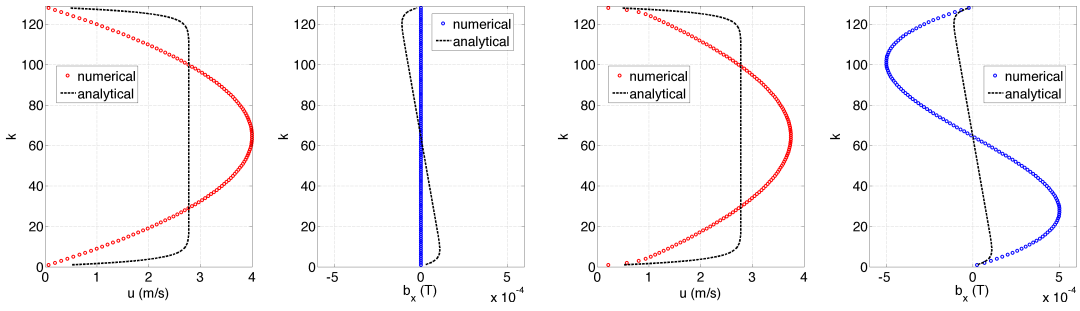

(a) $t = 0.00\tau$ (b) $t = 0.34\tau$

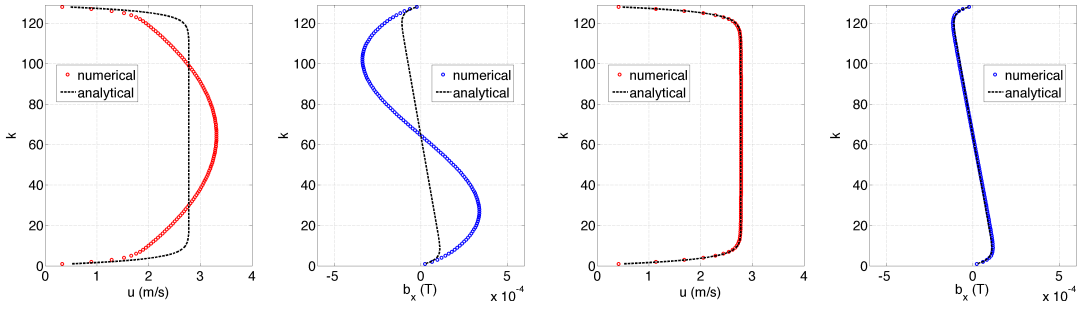

(c) $t = 0.84\tau$ (d) $t = 5.04\tau$

Fig. 35. Case H3, time evolution of Hartmann flow at outlet ($i = 512, j = 1$).

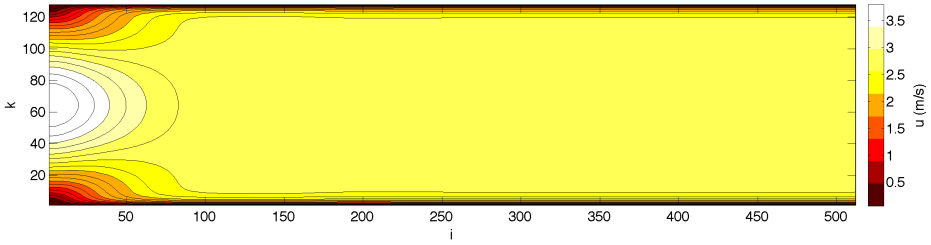

(a) Velocity, u

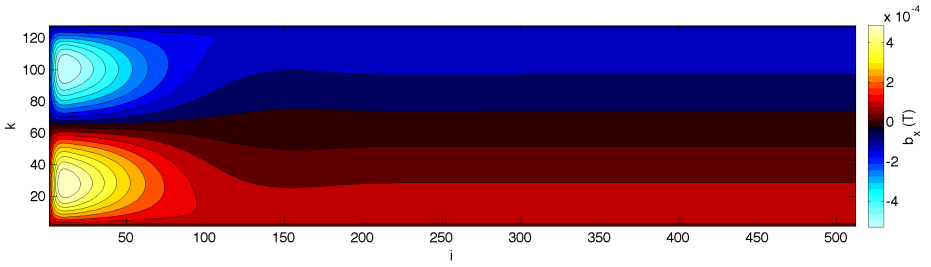

(b) Induced magnetic field, b_x

Fig. 36. Case H3, contour plots in the $x - z$ plane, $t = 5.04\tau, j = 1$.

D. Lorentz Force Discussion

For both the MHD Couette and Hartmann channel flows, the applied magnetic field in some way distorts the shape of the velocity profile. This effect can be understood more clearly by examining the Lorentz force acting on each flow. From Sutton [40], examples of the current distribution for the MHD Couette and Hartmann flows simulated in this chapter are illustrated in Figures 37(a) and 37(b), respectively. This current is driving the distortion of the flow by the Lorentz force, which is $\mathbf{F}_L = \mathbf{j} \times \mathbf{B_0}$, and is shown acting on the classical Couette and Poiseuille profiles in Figures 37(c) and 37(d).

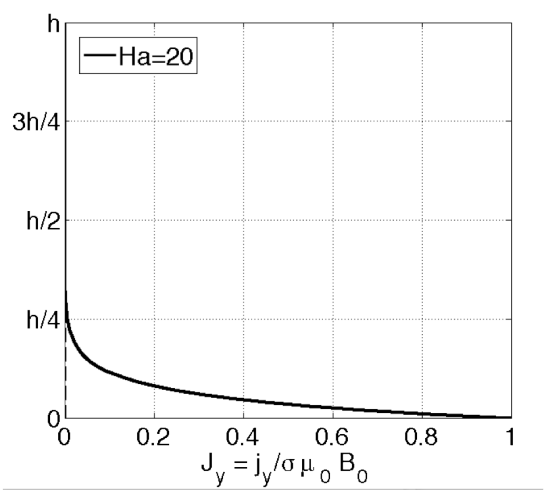

(a) MHD Couette induced current.

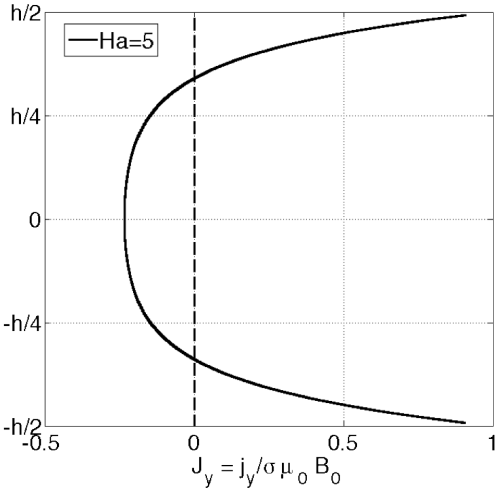

(b) Hartmann induced current.

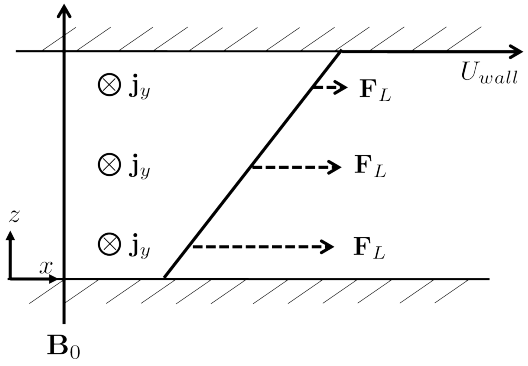

(c) Lorentz force in Couette flow.

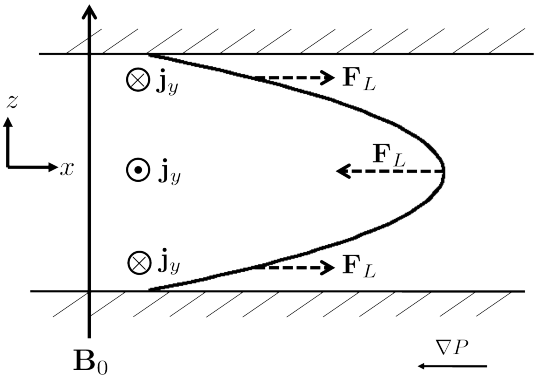

(d) Lorentz force in Poiseuille flow.

Fig. 37. Action of the Lorentz force on channel flows.

E. Chapter Summary

The results of this chapter have demonstrated the capability of the new GKM-MHD code to simulate flows with simple geometry on massively parallel machines. There is excellent agreement between the GKM-MHD simulations of transient MHD Couette and Hartmann flows and their steady state analytical solutions. The simulations also demonstrated the effects of varying the magnetic Reynolds number and Hartmann number. In the MHD Couette flow simulations, increasing the magnetic Reynolds number resulted in an increase of the magnitude of the induced magnetic field and also increased the damping of kinetic and magnetic energies approaching equilibrium. In the Hartmann flow simulations, increasing the Hartmann number resulted in a flattening of the velocity profile near the center of the channel and a steepening of the gradients for the velocity and induced magnetic fields near the walls. In the next chapter, results for three-dimensional MHD jet simulations are presented, where closed-form analytical solutions for exact comparison are no longer available.

CHAPTER VI

LAMINAR ROUND JET SIMULATIONS

In this chapter, results for three-dimensional simulations of a laminar round jet are presented using the GKM-MHD code. The jet is restricted here to being laminar for simplicity and to help isolate steady state hydrodynamic behavior from transient or steady state magnetic effects.

A. Schlichting Self-Similar Solution

The starting point for all simulations in the next two sections is a steady state, laminar round jet. This jet is obtained by "sidewall injection" of one fluid into another of the same density that is initially at rest. The jet of fluid eventually develops into an axisymmetric steady state flow, which far downstream exhibits a self-similar region. This self-similar region was described analytically by Schlichting [44] who examined an asymptotic solution of the jet momentum originating from a point source, as illustrated in Figure 38.

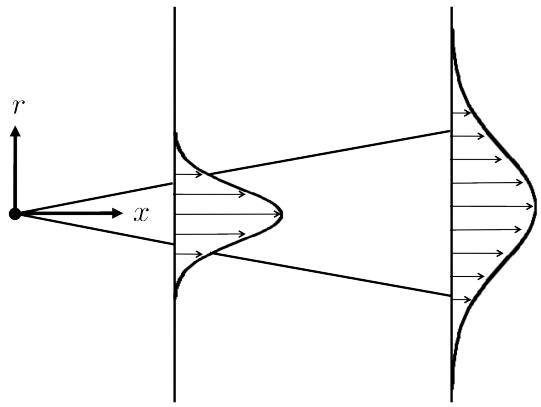

Fig. 38. Schematic of Schlichting's axisymmetric jet.

A result of Schlichting's analysis is the following equation for the u velocity component of the jet:

$$u(r,x) = \frac{3K}{8\pi\nu x}\left[1 + \frac{3K}{64\pi\nu^2}\left(\frac{r}{x}\right)^2\right]^{-2} \tag{6.1}$$

where ν is the kinematic viscosity and K is the momentum supplied by the point source. The numerical simulation of this flow starts from the initial conditions given in Table IV; an illustration of the computational domain is shown in Figure 39.

Table IV. Schlichting jet flow initial conditions.

	$u(m/s)$	$\rho(kg/m^3)$	$T(K)$	$\mu(kg/m\ s)$	M	Re
Inlet	41.094	1	353.05	0.013698	0.129	600
Background	0	1	353.05	0.013698	0	0

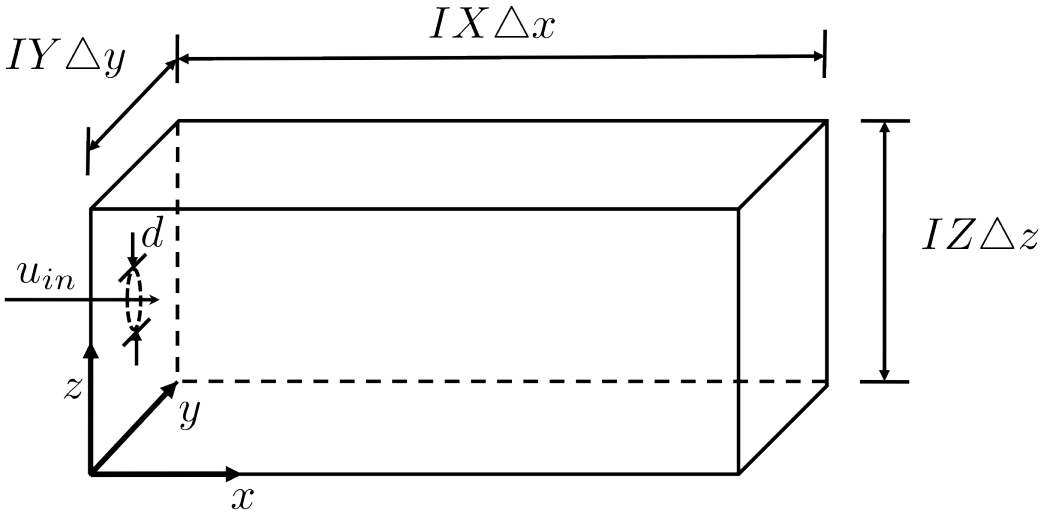

Fig. 39. Computational domain for round jet simulations.

In Figure 39, all boundaries of the box, except the inlet side, have zero-gradient boundary conditions. At the circular inlet, Dirichlet boundary conditions are speci-

fied, as well as no-slip and zero heat flux everywhere else on the inlet sidewall. The grid is Cartesian with a uniform cell size of $\triangle x = \triangle y = \triangle z = 0.0125m$. The number of grid points is ($IX = 400$) x ($IY = 128$) x ($IZ = 128$), and the inlet diameter is $d = 0.2m$. Contour slices in the $x - z$ mid-plane are shown in Figures 40(a)-40(b) illustrating the early time evolution of the flow as it begins to develop. The $u - v$ velocity streamlines are superposed on top of these contour plots for more insight into the structure of the flow. This flow occurs very early in the simulation and is a clear example of a starting vortex propagating downstream. The vortex is generated by the initial jet impacting the static background fluid. Several images taken from the experimental work of Auerbach [45] are shown in Figure 41. The comparison is to show that the vortex is not an artifact of the computation but a physical process. This visualization of transient vortical flow has relevance for a later simulation in this chapter.

After some time, the flow settles to a steady state and is shown in Figure 42. The streamline patterns shown in Figure 43(a) agree well with those published by Babu et al. [46] in Figure 43(b). Figure 44 shows comparisons between the numerical results and the analytical self-similar solution given by equation 6.1 for the half-width u velocity at four different x locations. There is excellent agreement between the numerical results and the analytical solution at the furthest downstream location shown in Figure 44(e). The slight under prediction by the numerical simulation near the edge of the computational domain can be attributed to the upstream no-slip boundary conditions as discussed by Babu et al. [46]. However, no attempt was made to use other upstream boundary conditions because of the desire to directly compare with theoretical predictions for the MHD jet presented in the next section.

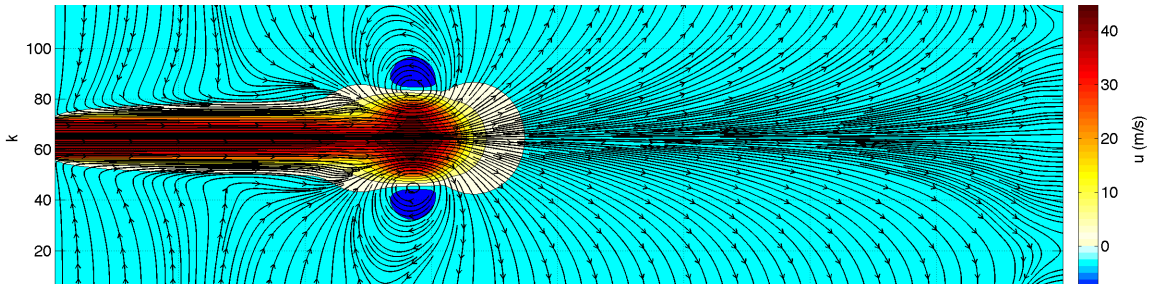

(a) $t_1 = 0.05s$.

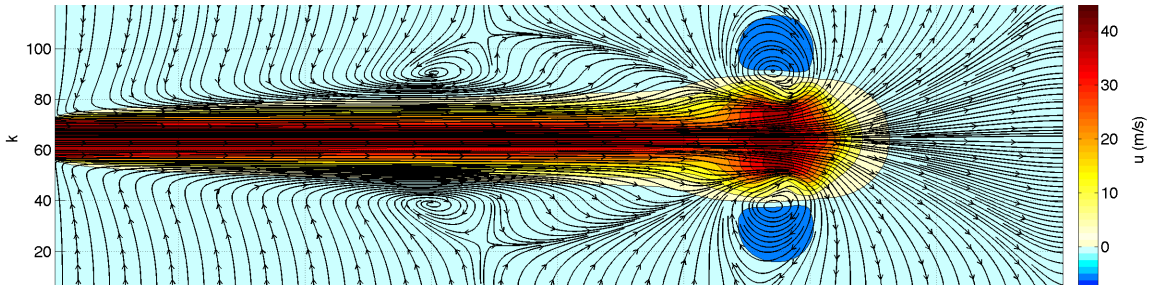

(b) $t_2 = 0.10s$.

Fig. 40. Early time evolution of laminar round jet simulation.

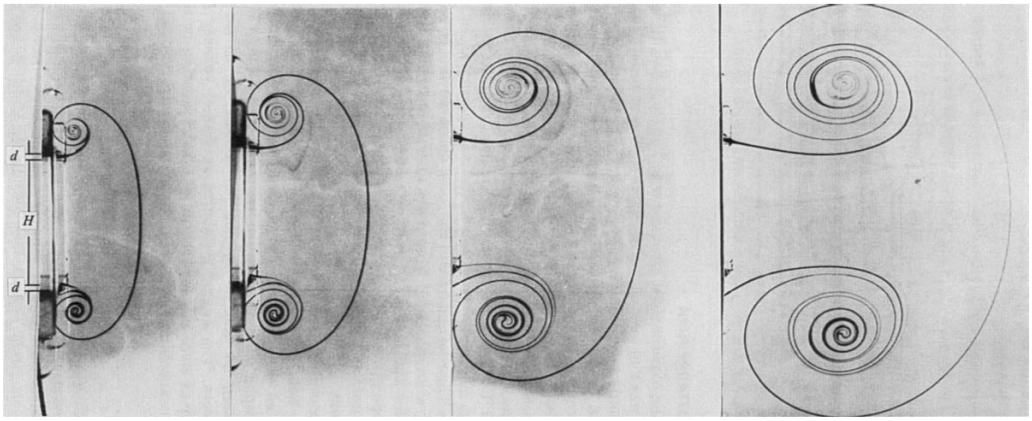

Fig. 41. Experimental flow visualization of starting vortex roll-up [45].

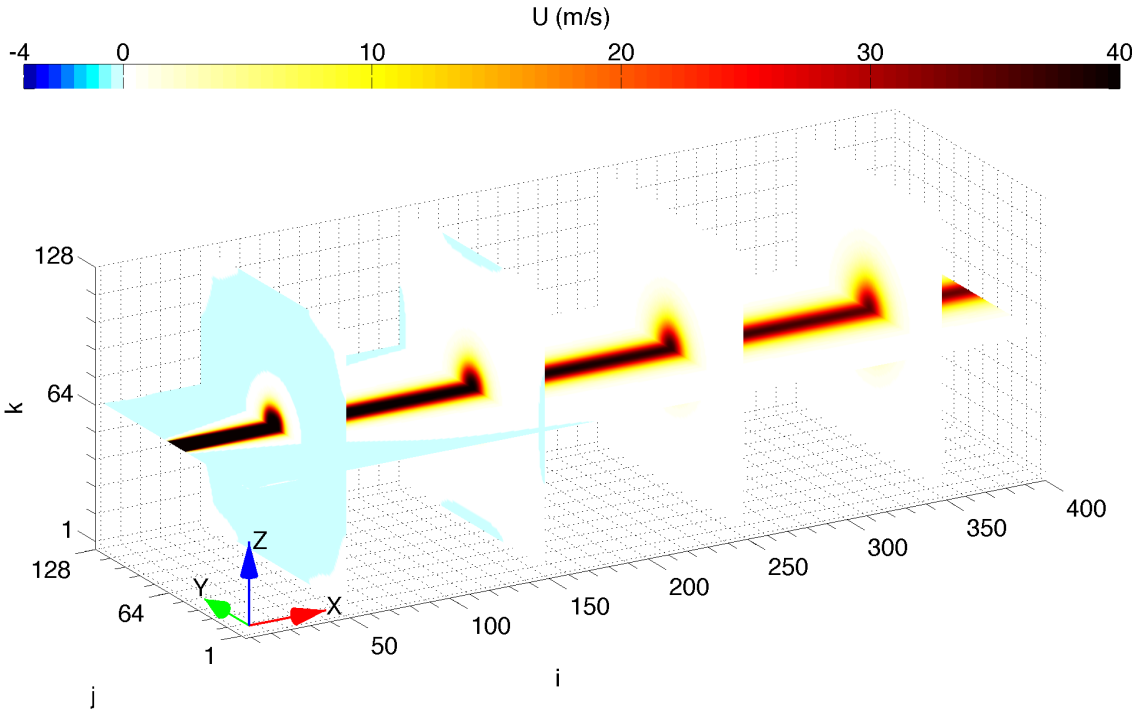

Fig. 42. Contour slices of steady state laminar round jet.

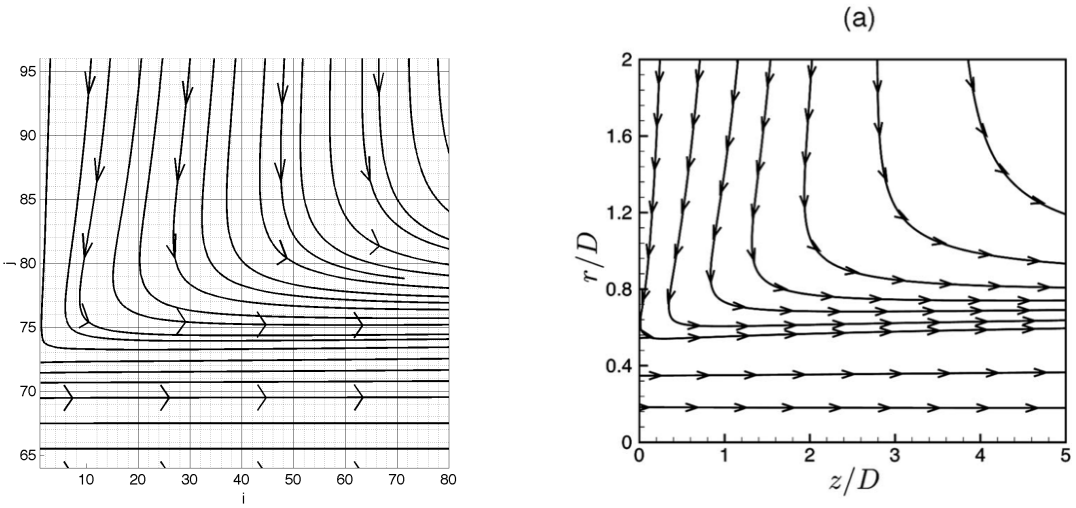

(a) GKM-MHD results. (b) Published results[46].

Fig. 43. Streamline pattern for steady state laminar round jet.

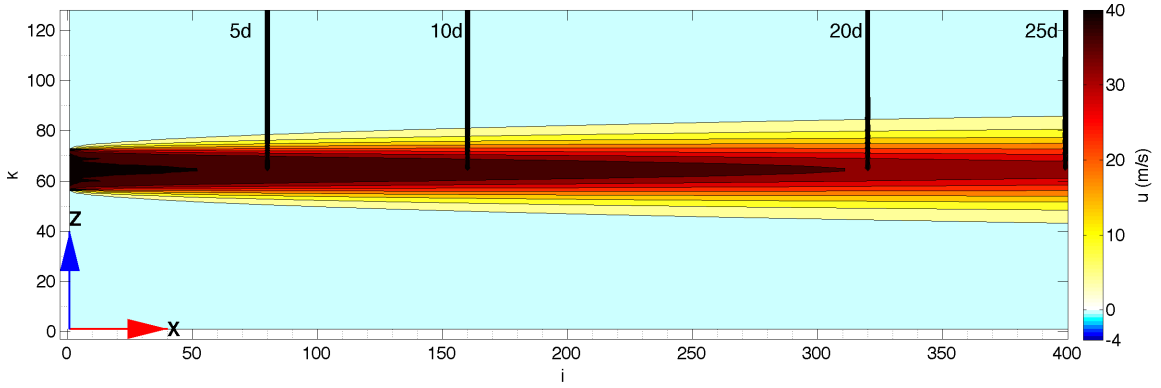

(a) $j = 64$.

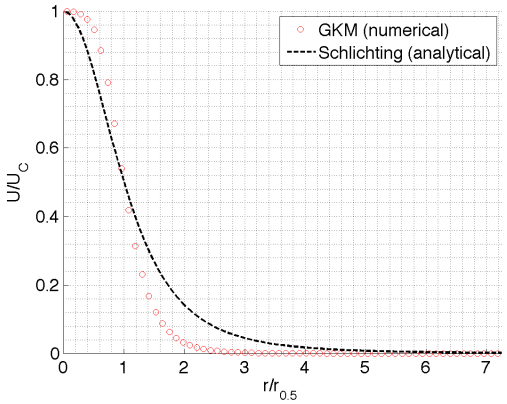

(b) $x/d = 5$.

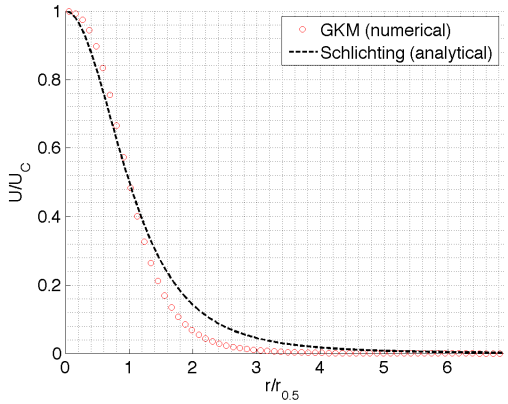

(c) $x/d = 10$.

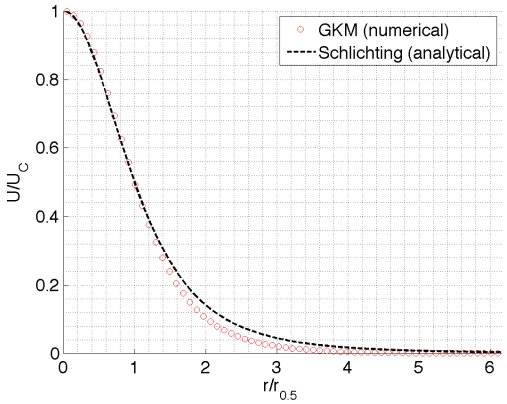

(d) $x/d = 20$.

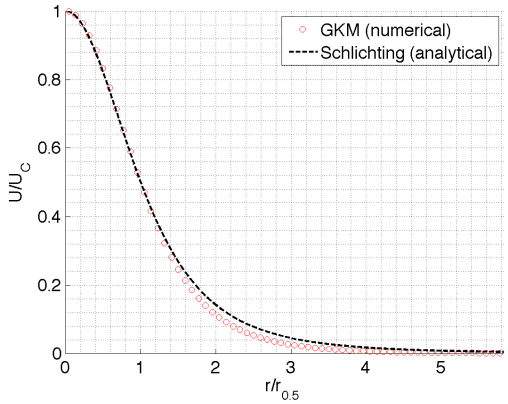

(e) $x/d = 25$.

Fig. 44. GKM numerical results vs. Schlichting solution at different x locations.

B. Laminar Round Jet With a Constant Applied Field.

With the steady state laminar jet solution obtained from the last section, the goal of the next two sections is to observe changes to the flow when an applied magnetic field is imposed. Very little analytical work has been done for these types of flows because of their mathematical complexity. However, the simplest case of a constant applied magnetic field has been examined by Davidson [32]. Specifically, he looks at the magnetic damping of liquid metal flows where the Reynolds number is large and the magnetic Reynolds number is small. The specific assumptions outlined in Davidson's theoretical work are summarized in Table V.

Table V. Davidson's theoretical assumptions.

Davidson Assumption	**Interpretation**
1. $\tau << \frac{\delta^2}{\alpha}; \qquad \tau = \frac{\rho}{\sigma B^2}; \quad \alpha = \frac{\nu}{Pr}$	diffusive time scale >> Lorentz force time scale
2. $\frac{\delta}{u} << \tau \qquad \text{or} \qquad N = \frac{\sigma u B^2}{\rho u^2/\delta} << 1$	Inertial forces >> Lorentz forces
3. $Re = \frac{u\delta}{\nu} >> \frac{1}{N} >> 1$	Lorentz forces >> Viscous forces
4. $Re_m = \mu_0 \sigma u \delta << 1$	Applied magnetic field >> Induced magnetic field

The jet simulation parameters, based on inlet conditions, were carefully selected to match these assumptions and are summarized in Table VI. The initial conditions for density, momentum, and energy for the MHD jet simulation are taken from the final solution in the Schlichting jet simulation. The applied magnetic field is

$B_z = 0.03T$ and the scalar conductivity is $\sigma = 1 \times 10^4 \Omega^{-1} m^{-1}$ everywhere. The boundary conditions are the same as in the Schlichting jet simulation with the additional condition on the induced magnetic field, which is assumed to be zero gradient everywhere except at the inlet sidewall where $\mathbf{b}_{induced} = 0$. Specifying zero induced magnetic field on the inlet boundary is an approximation that is justified for low magnetic Reynolds number (i.e., small induced currents). A similar argument is made by Luo et al. [47].

Table VI. Simulation parameters to match Davidson's assumptions.

Davidson Assumption	**GKM-MHD simulation**
1. $\tau << \frac{\delta^2}{\alpha}; \quad \tau = \frac{\rho}{\sigma B^2}; \quad \alpha = \frac{\nu}{Pr}$	$\tau = 0.111s << \frac{\delta^2}{\alpha} = 2.044s$
2. $\frac{\delta}{u} << \tau \quad$ or $\quad N = \frac{\sigma u B^2}{\rho u^2/\delta} << 1$	$\frac{\delta}{u} = 0.00487s << \tau = 0.111s$
3. $Re = \frac{u\delta}{\nu} >> \frac{1}{N} >> 1$	$Re = 600 >> \frac{1}{N} = 22.83 >> 1$
4. $Re_m = \mu_0 \sigma u \delta << 1$	$Re_m = 0.103 << 1$

Davidson makes three key qualitative predictions about the structure of the flow that results when the constant magnetic field is applied. The first prediction is that the jet stretches along the direction parallel to the applied field. This is illustrated schematically in Figure 45. The numerical results for the laminar round jet with and without a constant applied field are shown in Figures 46-48. Note that Figures 46-48 are zoomed-in views of the domain to show the details more clearly. The second qualitative prediction is the presence of reversed flow in the horizontal plane ($z = 0$, $x - y$ plane) and outward flow near the wall. This second prediction is illustrated by Davidson in Figure 49 and agrees well with the GKM-MHD numerical results in Figures 46-50. Finally, an illustration of the current density from Davidson is shown

in comparison with the numerical results in Figure 51. All of these numerical results show very good agreement with the qualitative predictions made by Davidson.

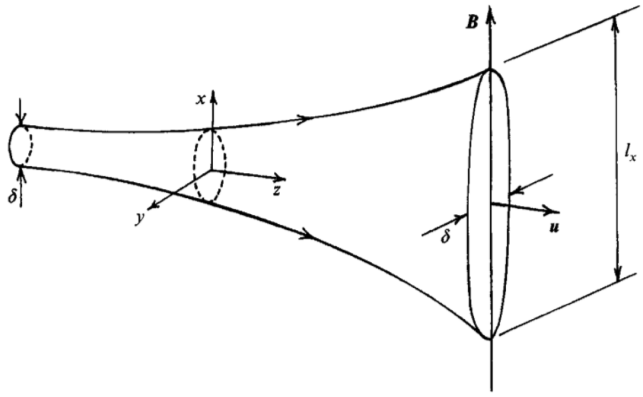

Fig. 45. Schematic of MHD jet stretching [32].

For a quantitative comparison, a 2-D steady state, similarity solution exists for the axial velocity in the symmetry plane, i.e. $y = 0$ or $j = 64$. This solution is only valid when $\alpha_B = \delta^2/\tau = constant$, and is given as the following:

$$u(x,0,z) = \left(\frac{3M^2}{32\alpha_B x}\right)^{1/3} sech^2\left[z\left(\frac{48\alpha_B^2 x^2}{M}\right)^{-1/3}\right] \tag{6.2}$$

where M is the momentum evaluated on the z-axis only. With this equation, the same half-width velocity plots that were done for the Schlichting solution can be obtained for this MHD jet and are shown in Figure 52. There is excellent agreement of the numerical results with the analytical solution near the core of the jet. However, due to the limitations on the size of computational domain and time for the simulation, the outside edge of the jet has not yet reached steady state. Figure 53 shows a time evolution of the half-width profile at a constant x location, which shows the solution slowly converging toward the analytical result.

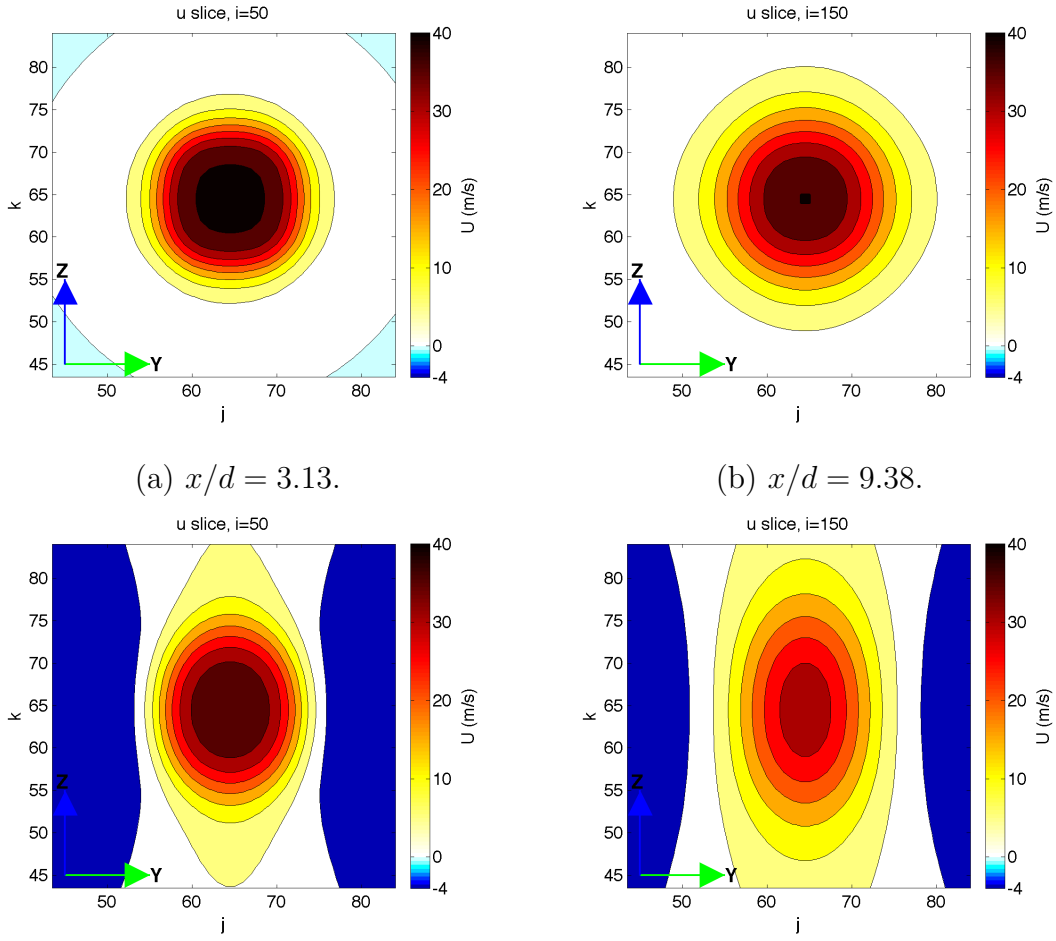

(a) $x/d = 3.13$.

(b) $x/d = 9.38$.

(c) $x/d = 3.13$.

(d) $x/d = 9.38$.

Fig. 46. Numerical results without (a,b) and with (c,d) constant B_z applied.

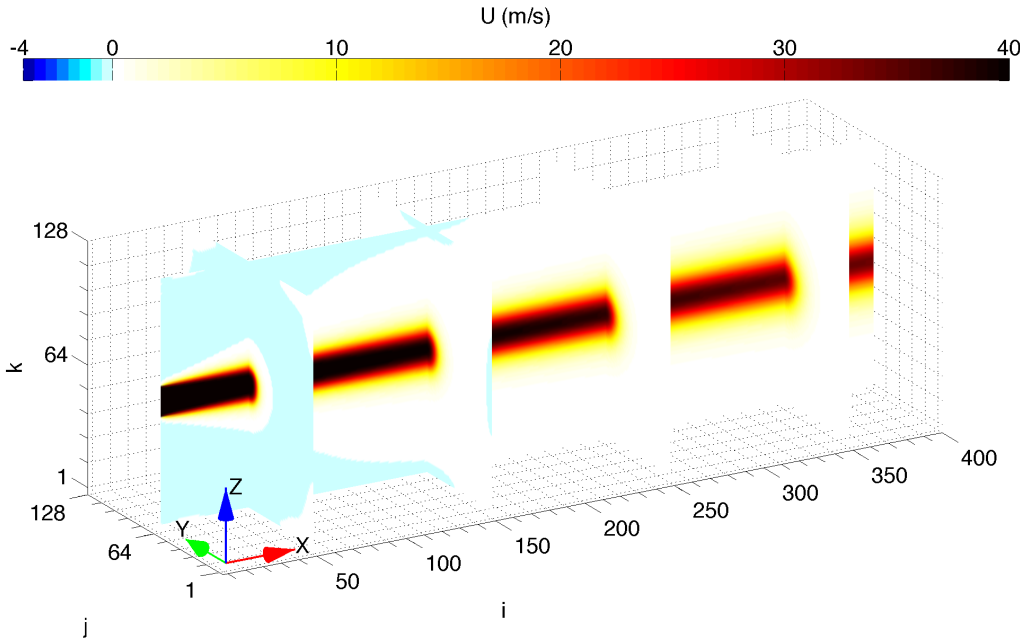

(a) $x-z$ and $y-z$ volume slices (without applied field).

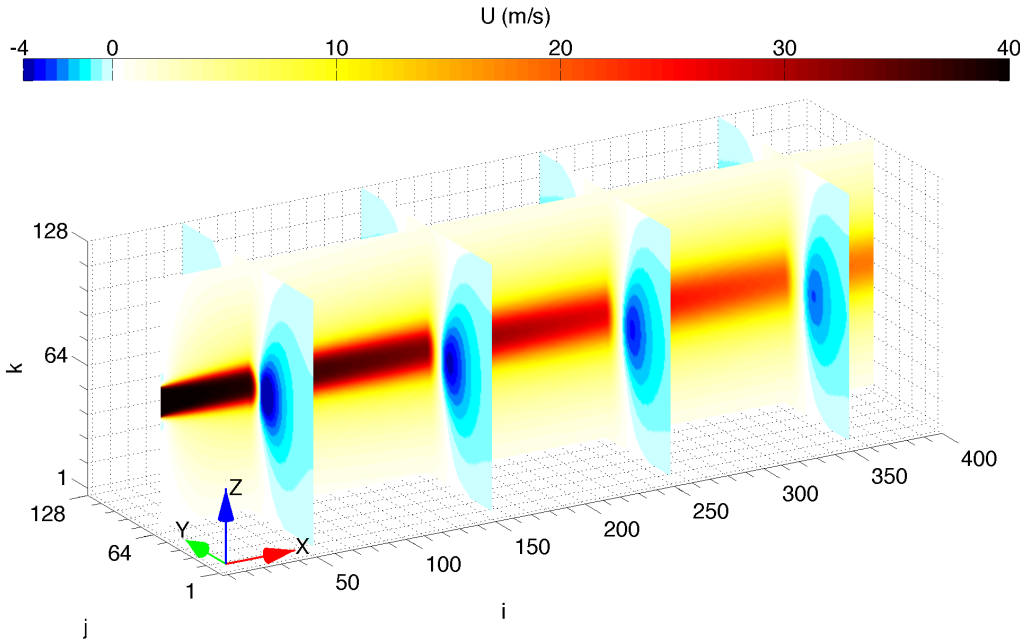

(b) $x-z$ and $y-z$ volume slices (constant B_z applied).

Fig. 47. Jet stretching and reversed flow for constant applied B_z.

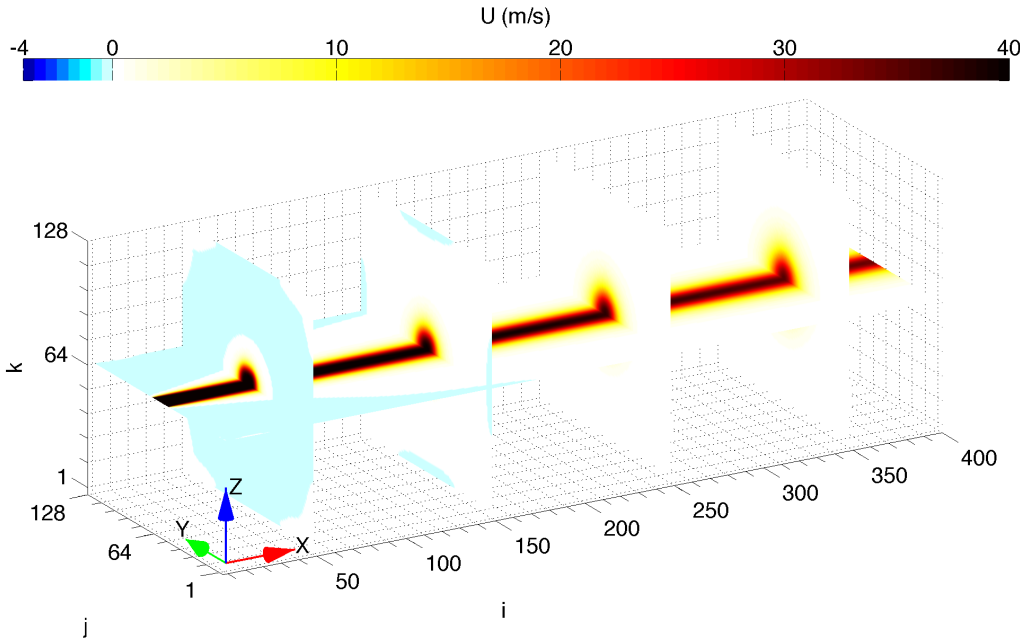

(a) $x-y$ and $y-z$ volume slices (without applied field).

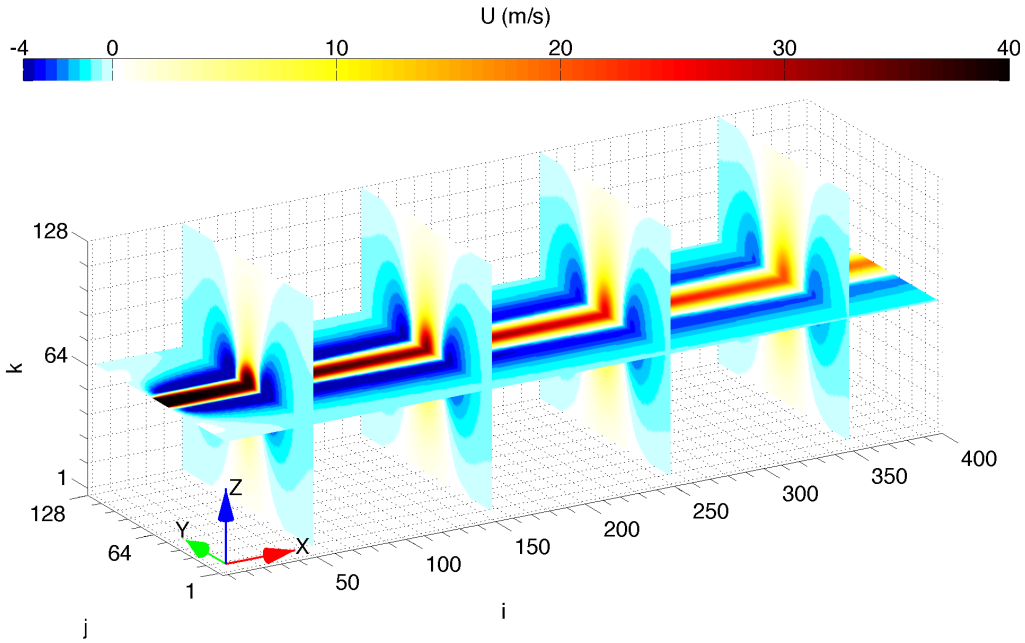

(b) $x-y$ and $y-z$ volume slices (constant B_z applied).

Fig. 48. Jet stretching and reversed flow for constant applied B_z continued.

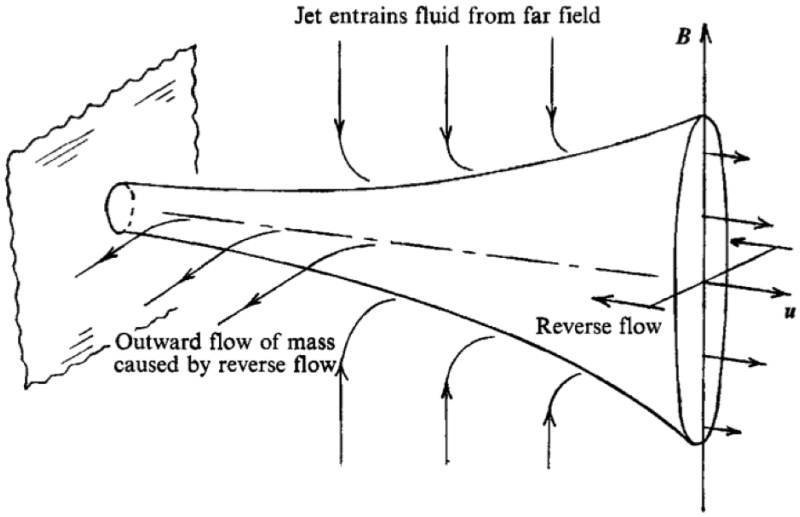

Fig. 49. Schematic of MHD jet outflow near the wall [32].

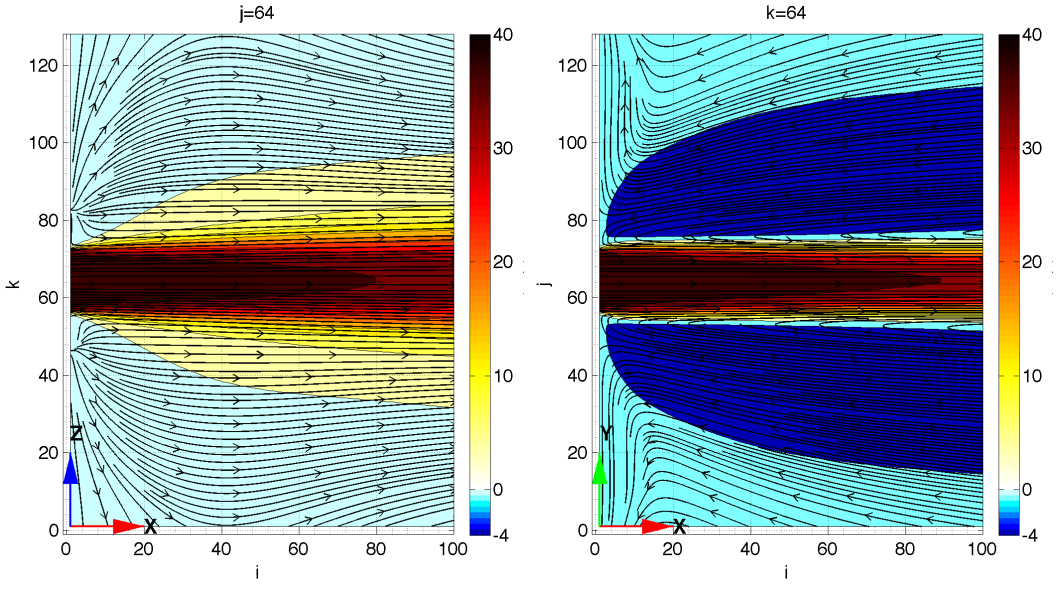

(a) u contours, $u - w$ streamlines. (b) u contours, $u - v$ streamlines.

Fig. 50. Near-wall flow (Constant B_z applied).

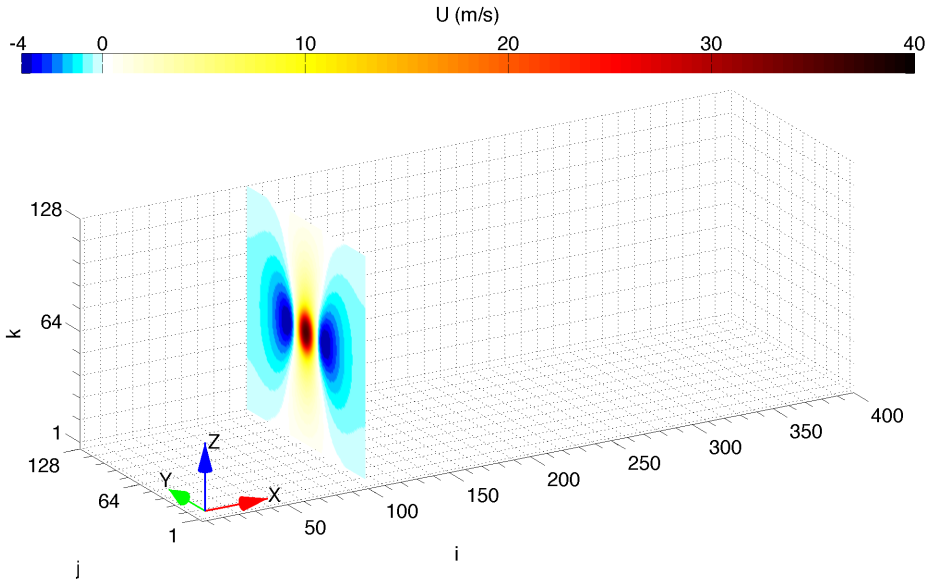

(a) Volume slice, $i = 100$.

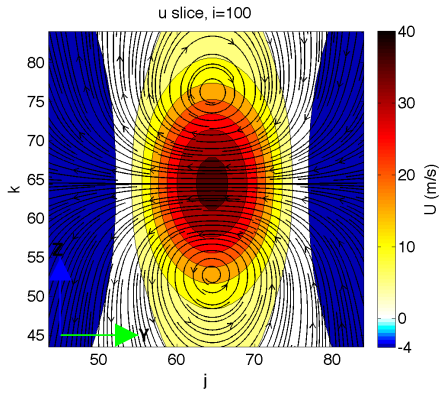

(b) GKM-MHD result.

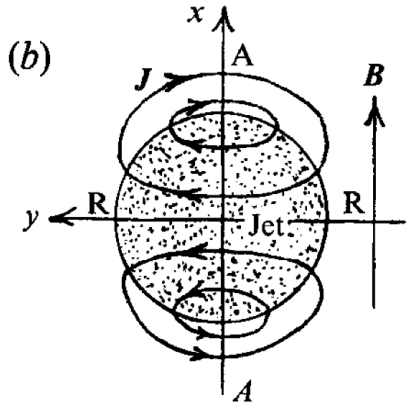

(c) Theoretical schematic[32].

Fig. 51. Current density streamlines.

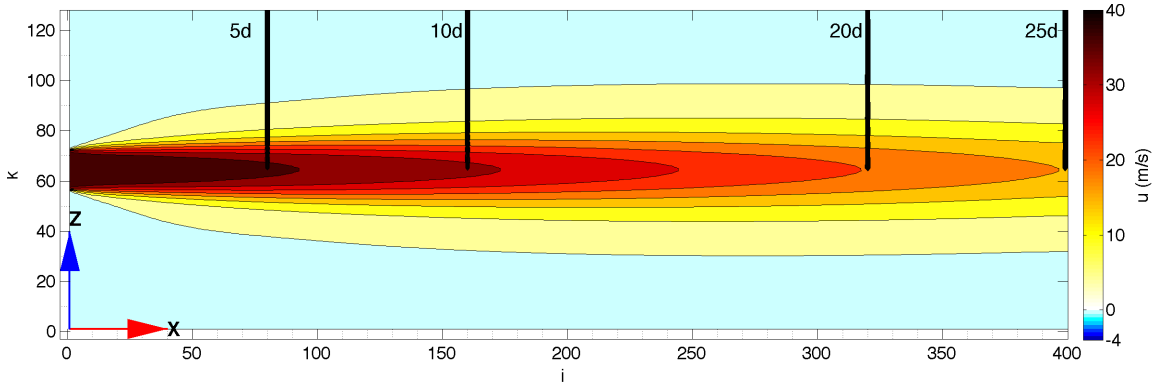

(a) $j = 64$.

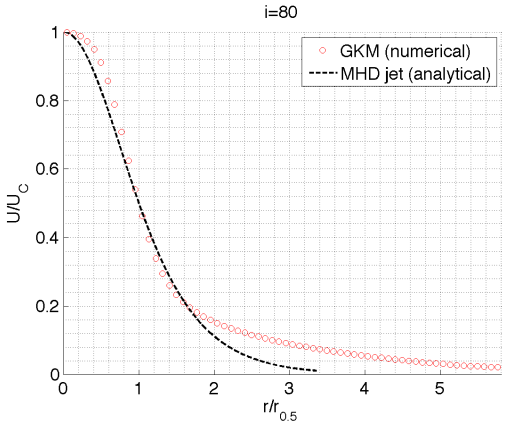

(b) $x/d = 5$.

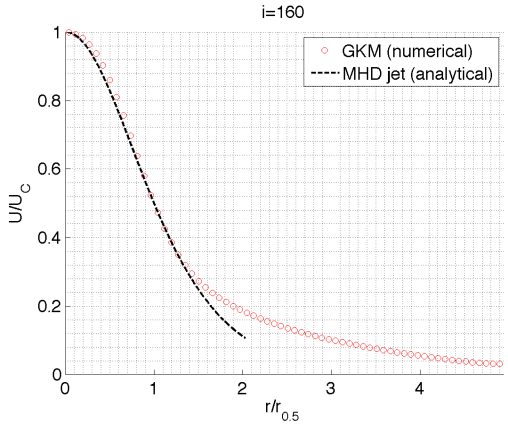

(c) $x/d = 10$.

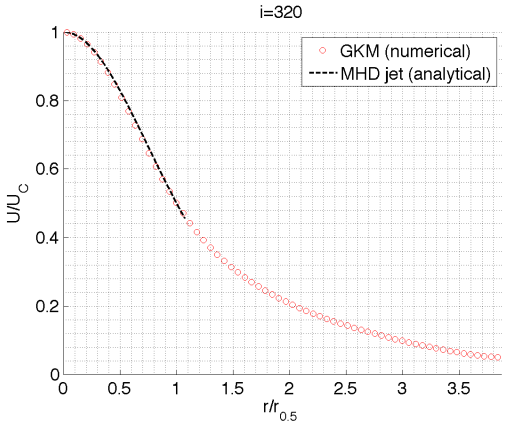

(d) $x/d = 20$.

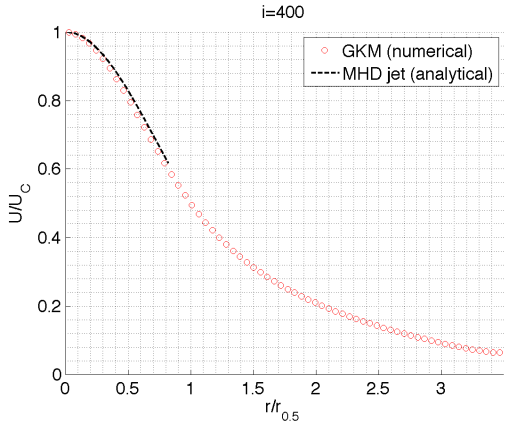

(e) $x/d = 25$.

Fig. 52. Half-width profiles for symmetry plane, $j = 64$.

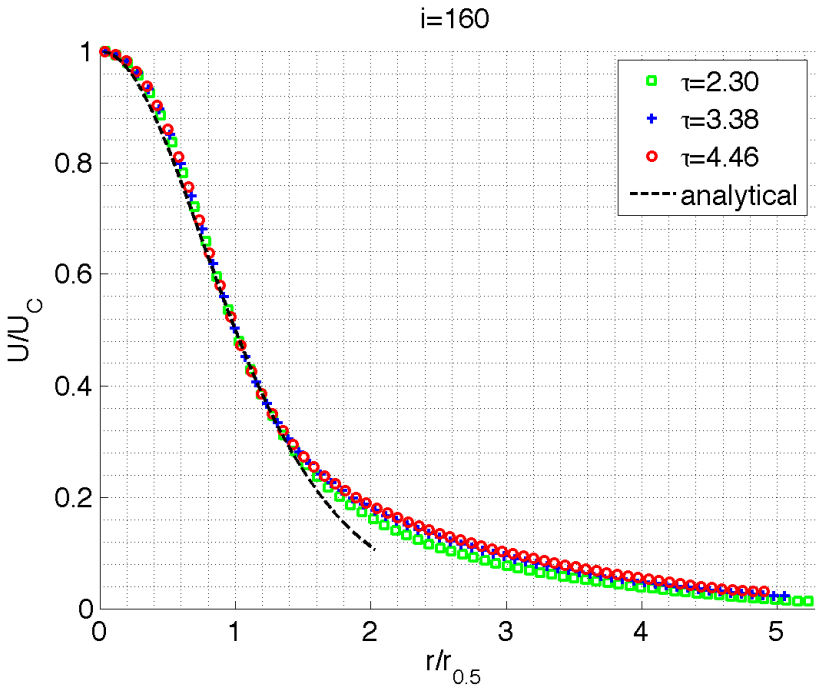

Fig. 53. Time evolution of half-width profile for $j = 64$ and $x/d = 10$.

C. Laminar Round Jet With a Current Loop

As a final test case, the GKM-MHD code is used to simulate a laminar round jet subject to the applied magnetic field generated by a current loop. The current loop configuration is shown in Figure 54 and the magnetic field is given by Biot-Savart's law, which is the following:

$$\mathbf{B}(\mathbf{r}) = \frac{\mu_0}{4\pi} \int \frac{\mathbf{j}(\mathbf{r}') \times (\mathbf{r} - \mathbf{r}')}{|\mathbf{r} - \mathbf{r}'|^2} dx'dy'dz' \tag{6.3}$$

where $\mathbf{r}(x, y, z)$ is any point in space and $\mathbf{r}'(x', y', z')$ is the distance to a point on the current loop. An Octave script freely available from the internet [48] was modified for use in MatLab and used to generate the applied magnetic field. The script was verified with analytical expressions given by Simpson et al. [49].

The strategy of this section is to first set up the same initial flow conditions as

in the Davidson jet except to replace the constant applied field for the current loop field and make note of any changes to the flow. The initial conditions for density, momentum, and energy for this jet simulation are again input from the final solution in the Schlichting jet simulation. In the first case, the current is chosen so that the maximum magnitude of the magnetic field is 0.03T at the inlet. Then, the current is increased for the second case so that the maximum magnitude of the magnetic field is 0.3T at the inlet. In both cases, the diameter of the current loop is the same as the inlet diameter and aligned axially one diameter upstream of the inlet. The initial conditions at the inlet for the two current loop cases are summarized in Table VII.

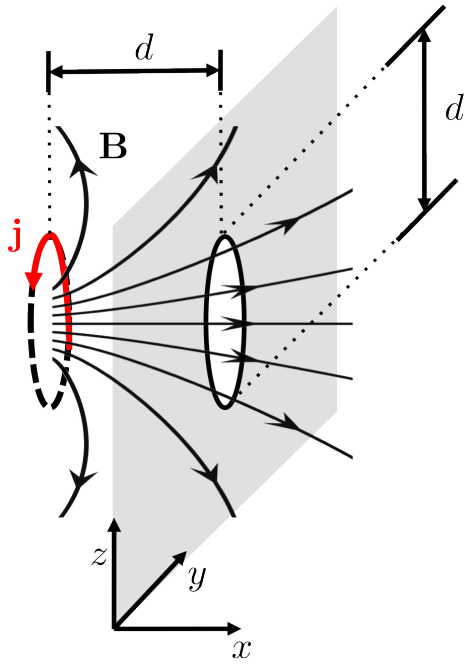

Fig. 54. Current loop simulation configuration.

First, the initial temporal evolution of the flow is observed in Figures 55-57 with and without the magnetic field for cases L1 and L2. The $u - w$ streamlines are superposed onto the u velocity contours to give insight into the flow structure. From

Table VII. Current loop jet flow initial conditions.

Case	$\|\mathbf{B}\|(T)$	$\sigma(\Omega^{-1}m^{-1})$	Re_m	Ha	N	M	Re
L1	0.03	1×10^4	0.1	5.13	0.04	0.129	600
L2	0.30	1×10^4	0.1	51.26	4.38	0.129	600

these figures, it is evident that there is an initial traveling vortex created by the flow reacting to the imposed solenoid magnetic field. Once the vortex has left the domain, the flow continues to slowly evolve on a time scale similar to the Davidson jet. Figures 58 - 60 show several cross sections of the jet for the last time instant taken in the simulations of case L2. Interestingly, the jet appears to begin forming into a diamond shape near the inlet. Samulyak et al.[50] observed a similar shape change for computations of a liquid mercury jet entering a high strength solenoid magnetic field, as shown in Figure 61.

One possible explanation for the change in the jet profile comes from observing the current density in the simulations. Figure 62(a) shows the u velocity contours superposed with streamlines for the current density at the last time instant at the $x/d \approx 1$ location. The alignment of the closed current loops with the stretching of the jet appears to be directly analogous to the one shown in the example with the constant applied magnetic field. For direct comparison, the current density from the Davidson jet at the same x location is shown in Figure 62(b). Another possible explanation is that the diamond shape is simply an artifact of the square boundaries of the computational domain. The jet system is assumed to be axisymmetric, but the current code is restricted to a Cartesian grid. Therefore, if the square boundaries are not far enough away from the jet, numerical errors could be introduced. Due to the limitations of computational resources, no attempt was made to try any alternative

boundary condition setup at this time.

Finally, Figure 63 shows two $y-z$ cross sections of the flow near the wall at the last time instant for case L2. In these figures, the $v-w$ streamlines are superposed onto the u velocity contours. There are distinct recirculation regions that are axisymmetric about the jet centerline and flowing away from the jet inlet. By mass conservation, it is possible that this outflow is accounted for by the observed deceleration of the jet, in conjunction with the continuous flow from the inlet.

D. Lorentz Force Discussion

As a final point to conclude this chapter, the action of the Lorentz force is discussed in an attempt to explain the observations presented in the last section. A similar discussion was presented in the chapter on channel flows and helped to solidify the physical interpretation of the results.

Figure 64 shows an idealization of what is called a "theta pinch" in fusion literature [51, 43] and even some space propulsion concepts [52]. An azimuthal diamagnetic current and an axially aligned magnetic field results in a Lorentz force, $\mathbf{F}_L = \mathbf{j} \times \mathbf{B}$ that is directed radially inward, compressing the column of plasma. Though it is not found to be called anything in the literature, for illustrative purposes, the opposite effect could be called a "theta pull." This is illustrated in Figure 65 and occurs when the azimuthal current is in the opposite direction to the theta pinch configuration.

In case L2 of the jet with the current loop, it is interesting to note that the traveling vortex is generated as soon as the solenoid magnetic field is turned on. A close up of the vortical flow is shown in Figure 66. The three-dimensional flow in this jet simulation is quite complex. However, a simple idealization of the flow is proposed in Figure 67. The direction of the azimuthal current was taken from Figure 62(a).

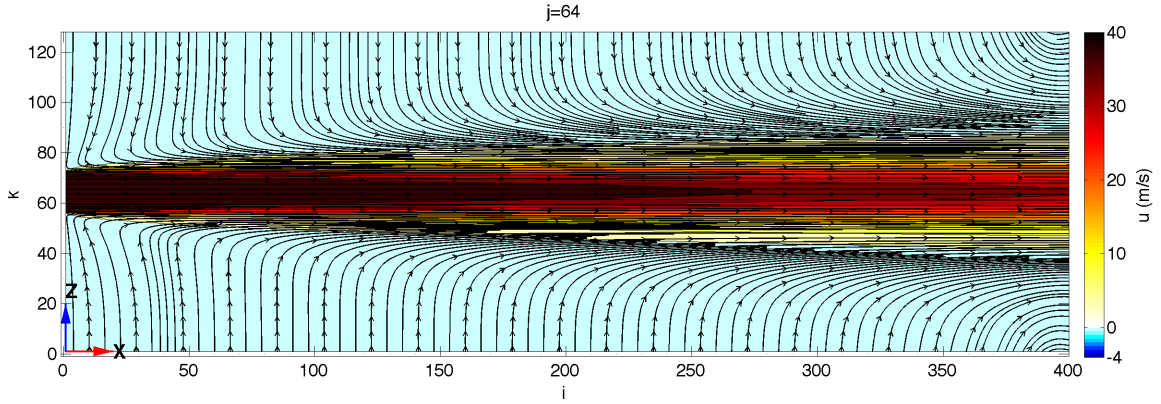

(a) Current loop off.

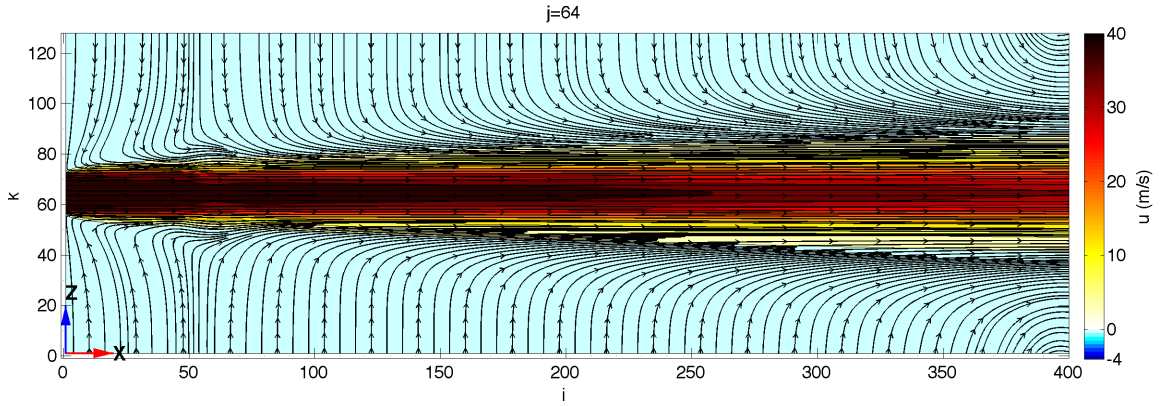

(b) Case L1.

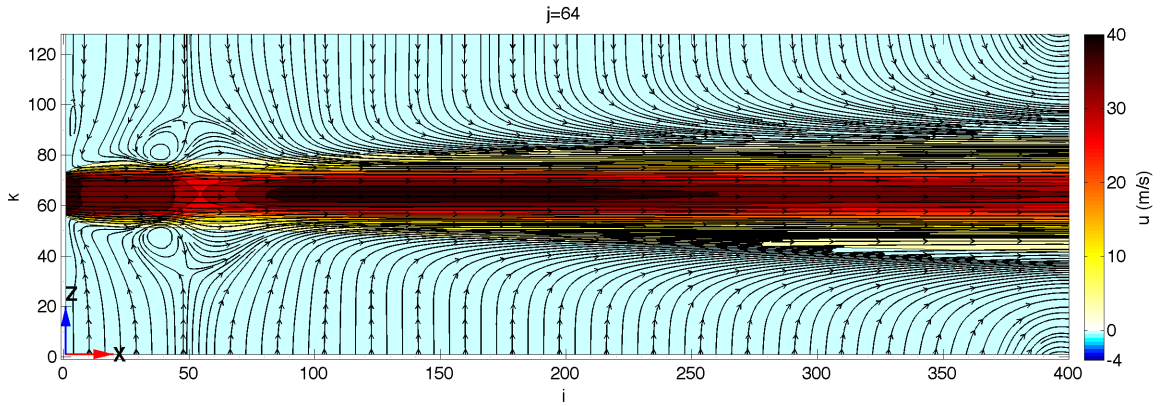

(c) Case L2.

Fig. 55. Laminar round jet with a current loop, $t = 0.03s$.

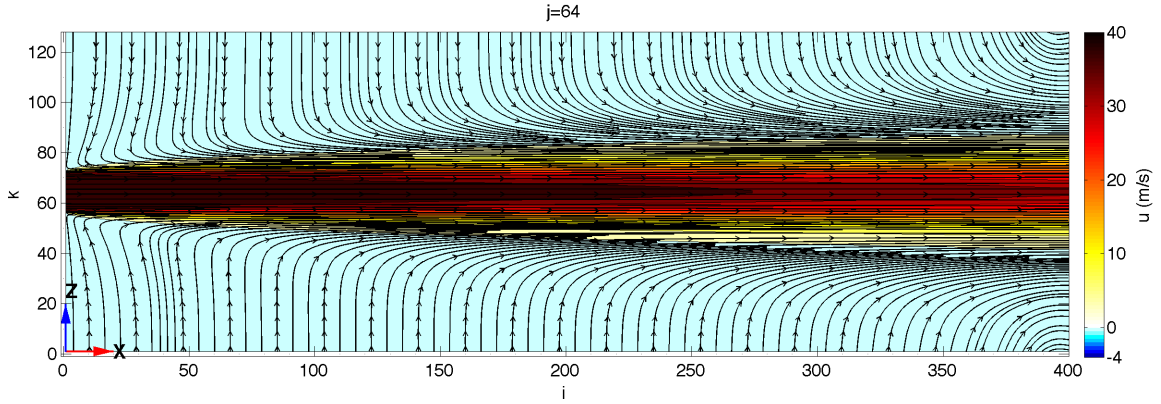

(a) Current loop off.

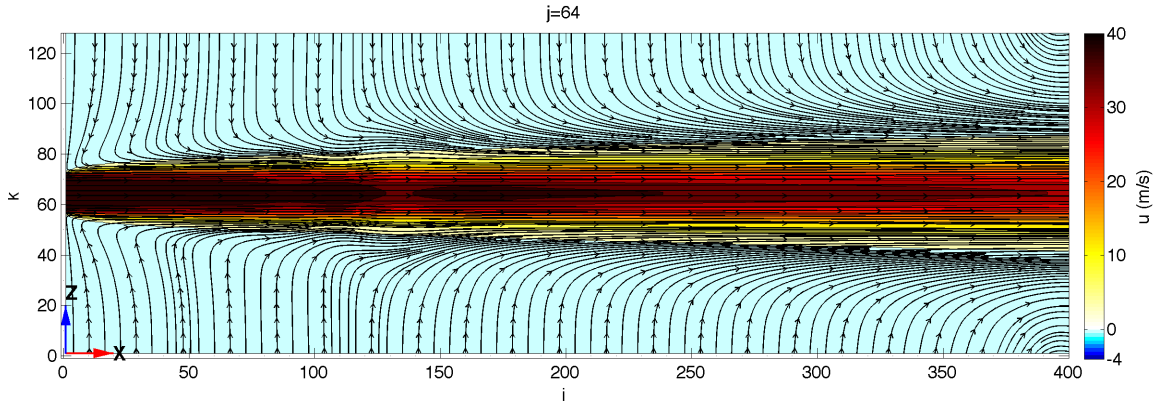

(b) Case L1.

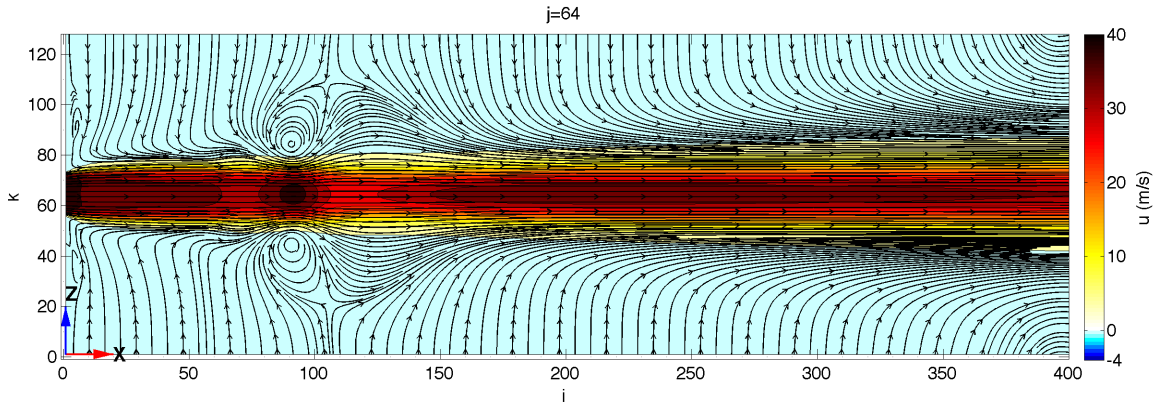

(c) Case L2.

Fig. 56. Laminar round jet with a current loop, $t = 0.06s$.

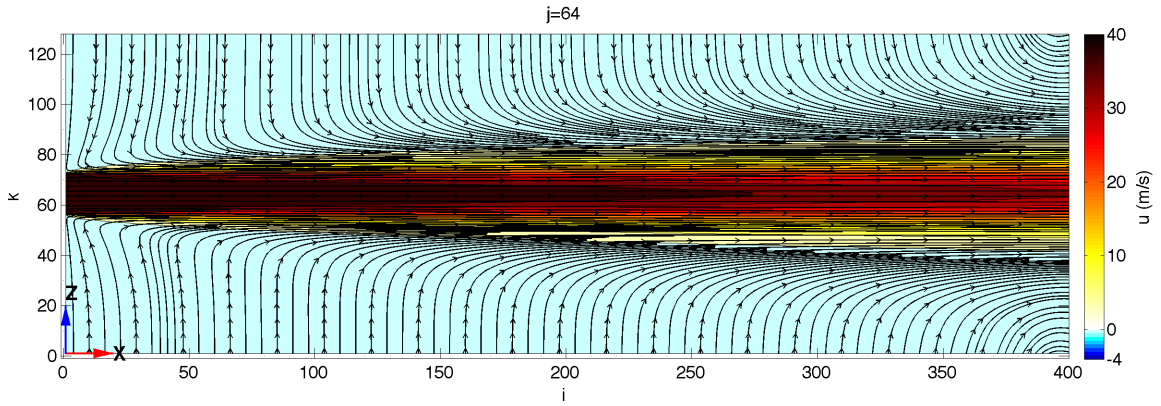

(a) Current loop off.

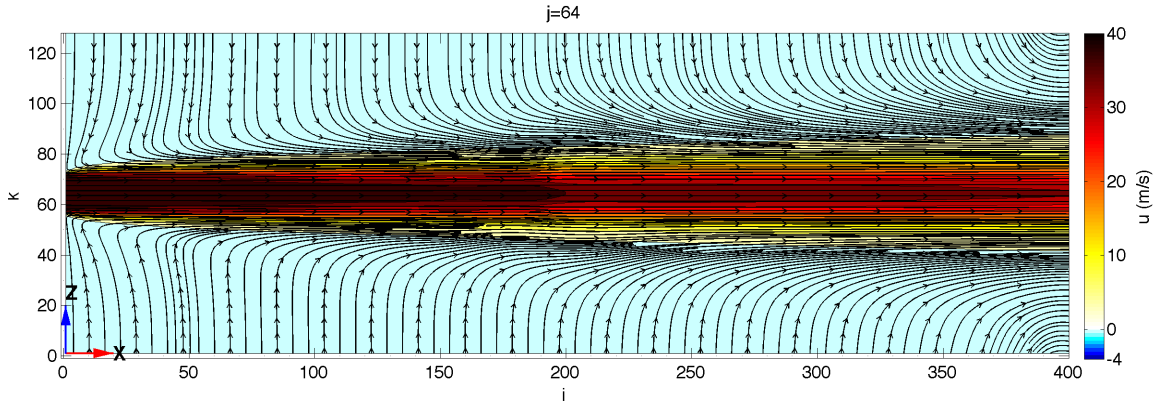

(b) Case L1.

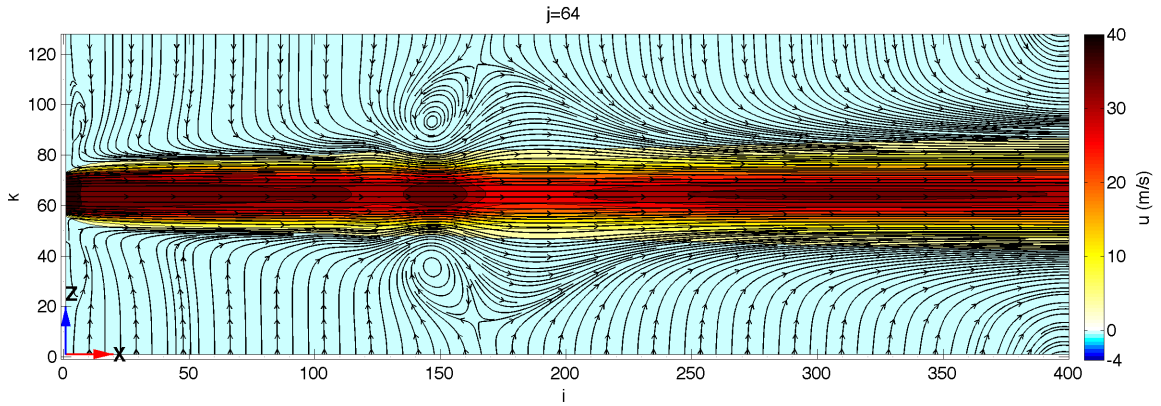

(c) Case L2.

Fig. 57. Laminar round jet with a current loop, $t = 0.09s$.

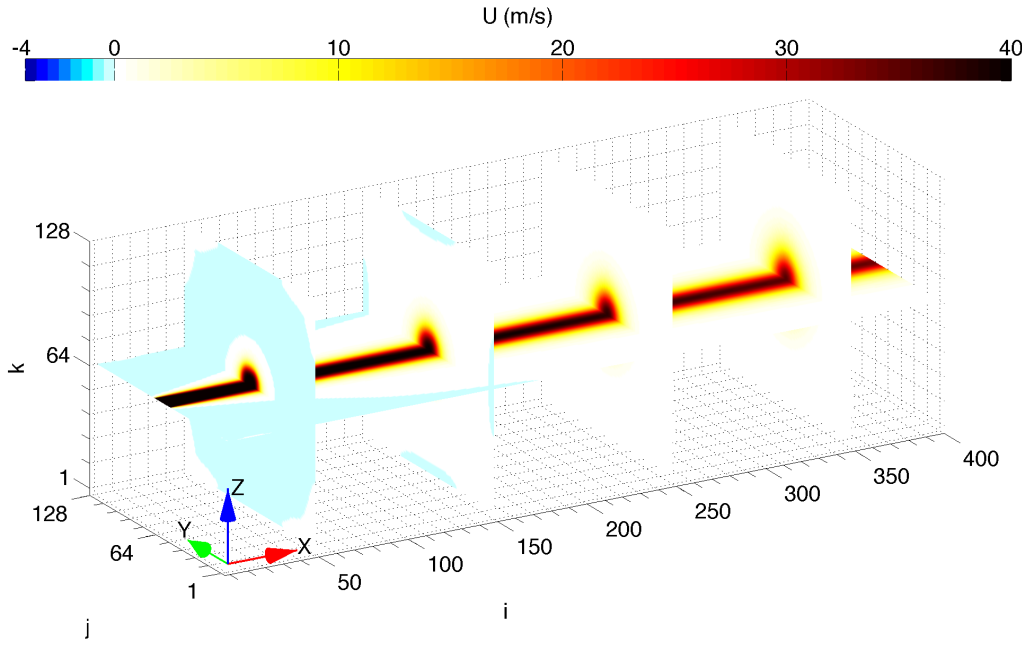

(a) $x-y$ and $y-z$ volume slices (current loop off).

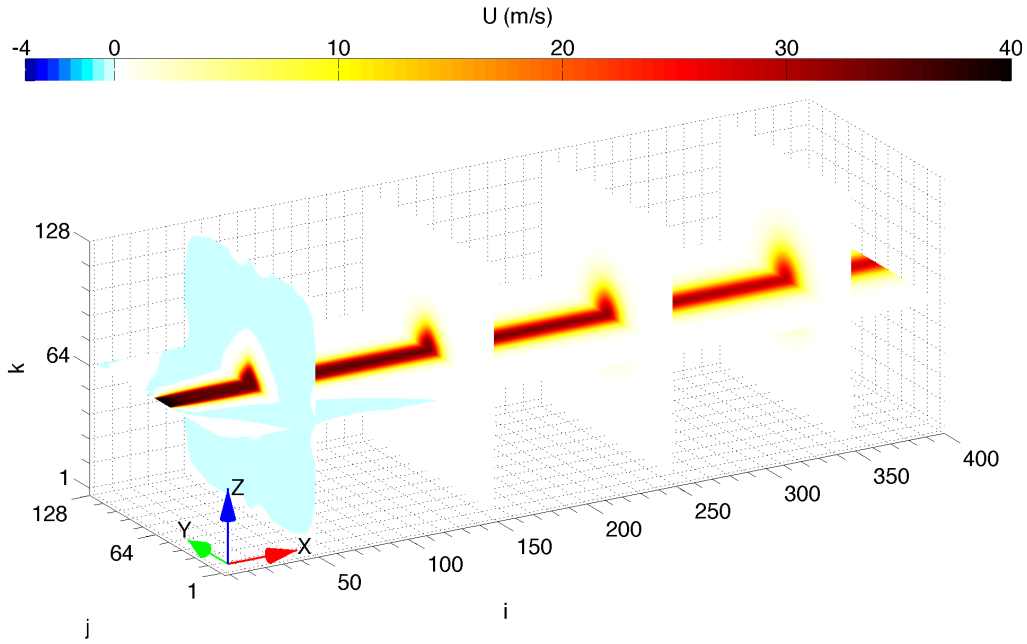

(b) $x-y$ and $y-z$ volume slices (current loop on).

Fig. 58. Volume slices ($x-y$ and $y-z$), case L2.

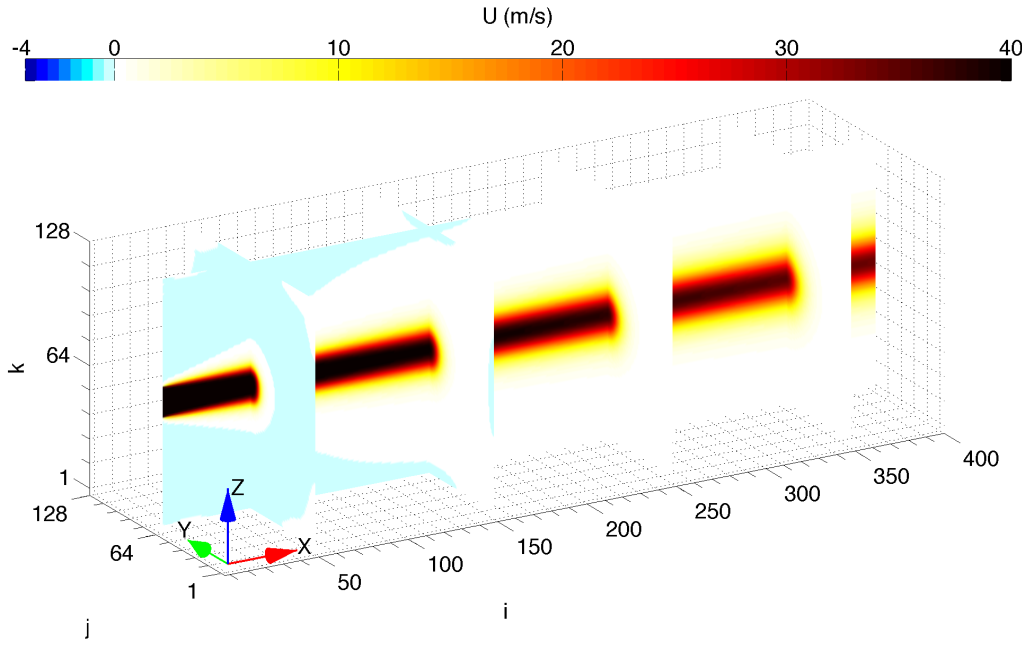

(a) $x-z$ and $y-z$ volume slices (current loop off).

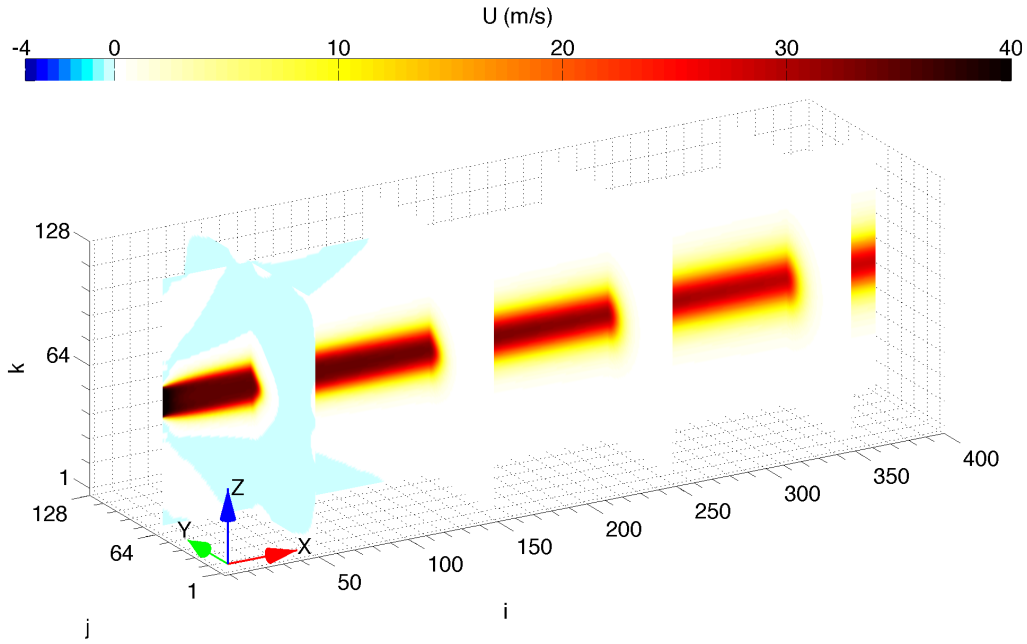

(b) $x-z$ and $y-z$ volume slices (current loop on).

Fig. 59. Volume slices ($x-z$ and $y-z$), case L2.

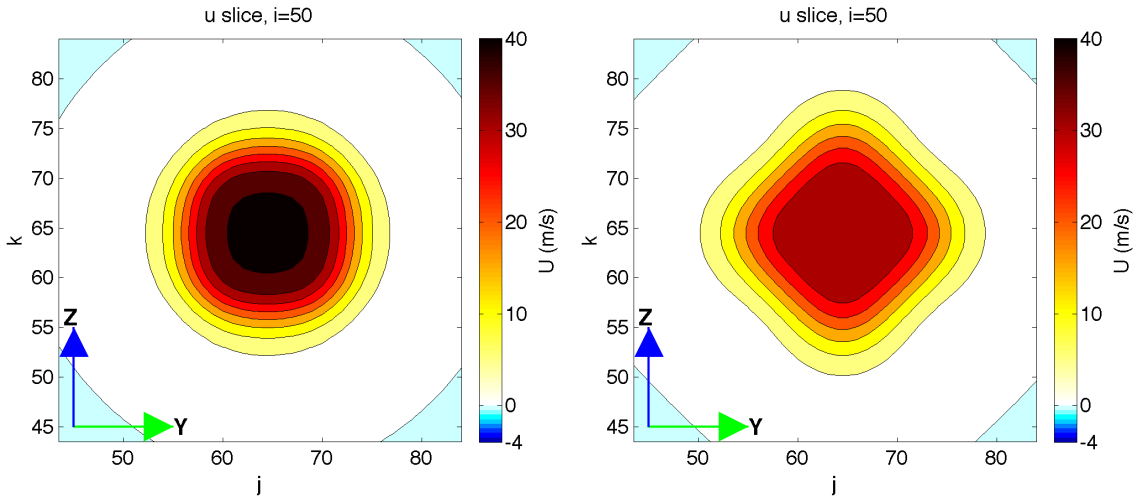

(a) $x/d = 3.125$. (b) $x/d = 3.125$.

Fig. 60. Case L2 results without (a) and with (b) applied magnetic field.

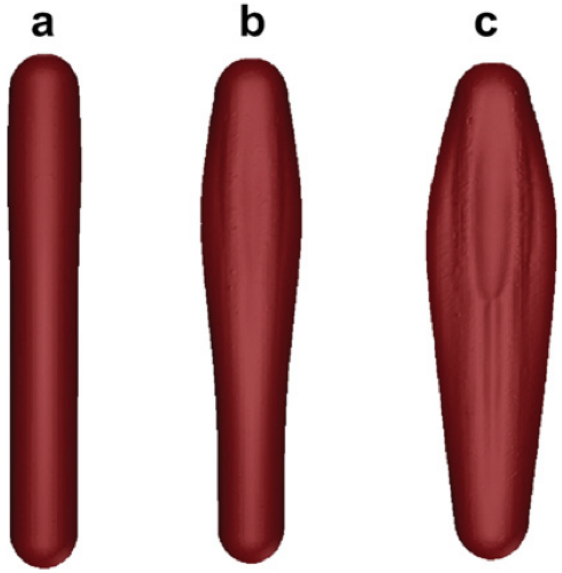

Fig. 61. Change of mercury jet shape as it enters a strong diverging magnetic field: (a) initial time, (b) $t = 1.0ms$, (c) $t = 1.5ms$ [50].

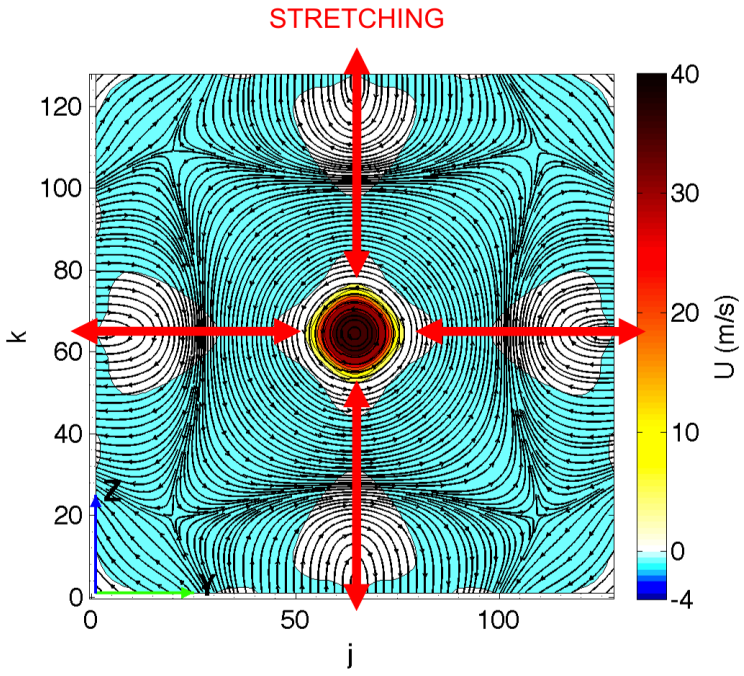

(a) Current loop applied field ($x/d \approx 1$), $j_y - j_z$ streamlines.

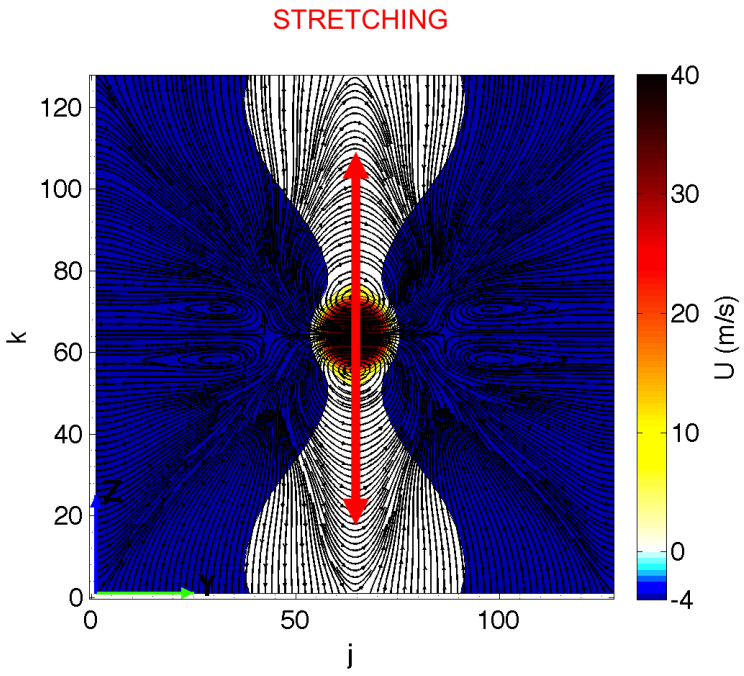

(b) Constant B_z applied field ($x/d \approx 1$), $j_y - j_z$ streamlines.

Fig. 62. Jet stretching aligned with current density streamlines.

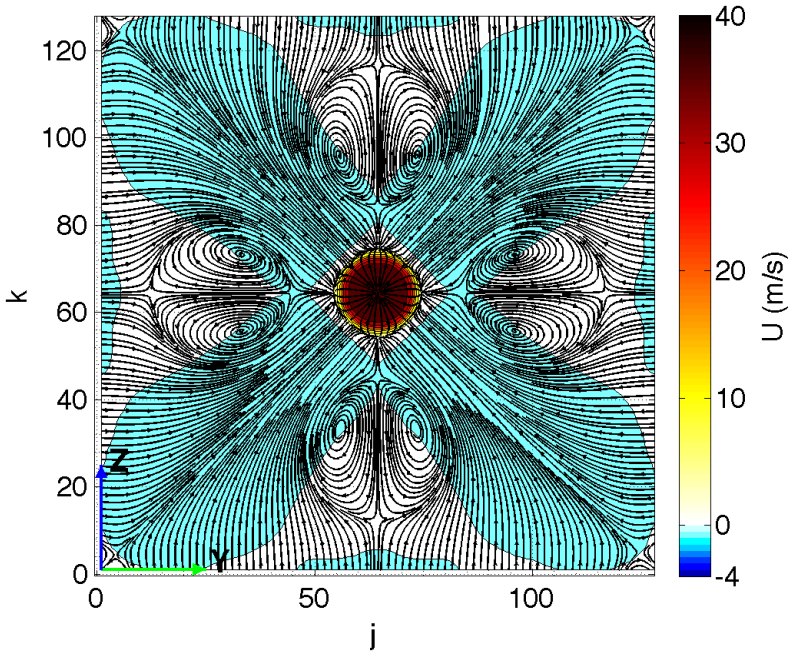

(a) $i = 5$.

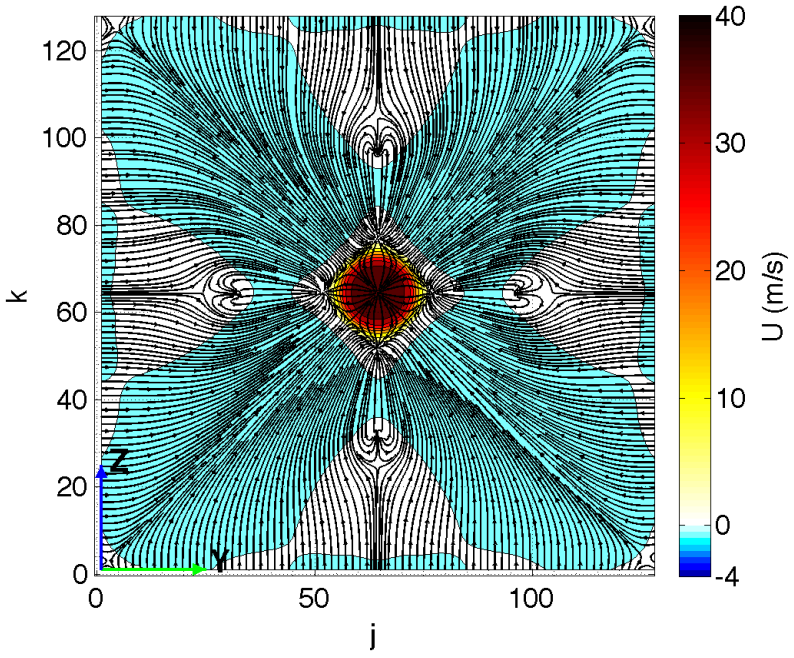

(b) $i = 10$.

Fig. 63. Axisymmetric recirculation near the wall for case L2, $v - w$ streamlines.

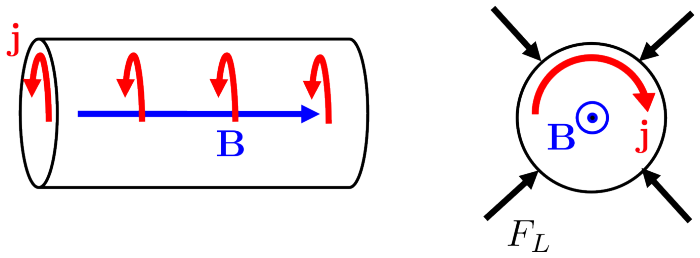

Fig. 64. Theta pinch.

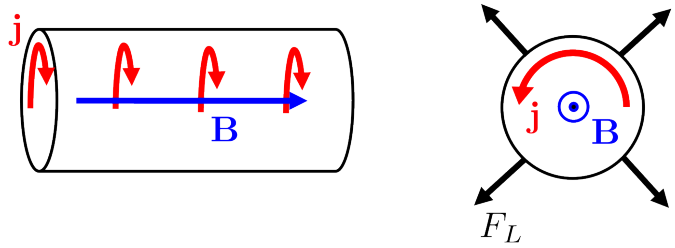

Fig. 65. Theta "pull".

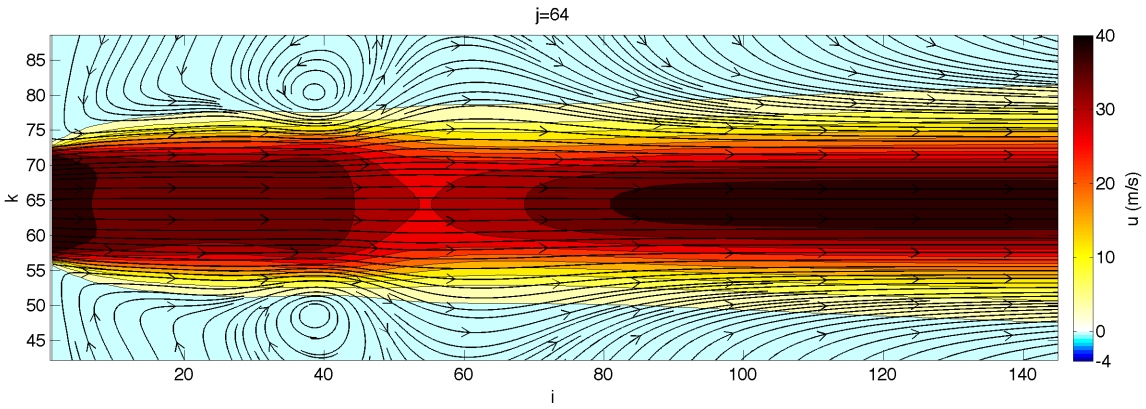

Fig. 66. Close-up of $u - w$ streamlines from Figure 55(c).

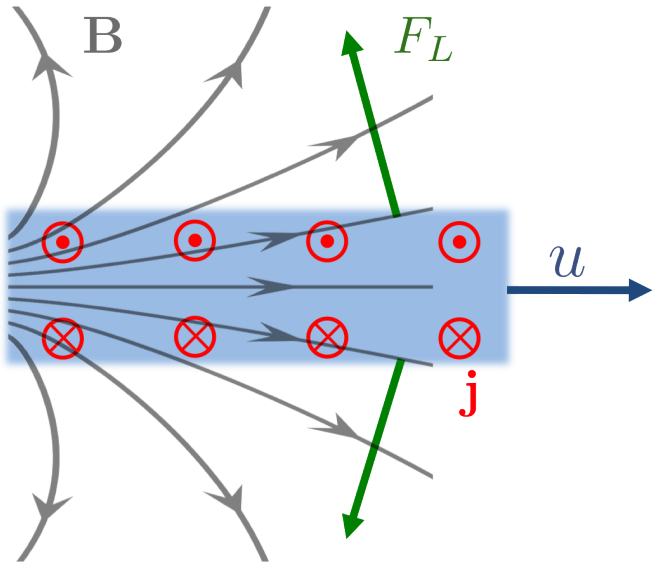

Fig. 67. Transient theta "pull" on jet with a current loop.

Figure 67 demonstrates that there is an outward directed Lorentz force on the jet at the first time instant. This force decreases radially outward as well as downstream. Along with the transient outward Lorentz force, there is fluid entraining from the far field boundaries as can be observed in Figures 55-57. In case L1, though there was no observed propagating vortex, the velocity streamlines do appear to be slightly perturbed outward, indicating the same transient effect of the outward Lorentz force. When the applied magnetic field is strong enough, such as in case L2, the combined effect of the fluid entrainment and the transient outward Lorentz force is perhaps enough to cause the observed vortex roll-up near the inlet.

It should be emphasized that the currents are aligned to cause this outward Lorentz force only as an initial transient effect in the simulation. The propagating vortex was only observed in case L2 and did not occur periodically, instead disappearing from the domain similar to the starting vortex described in the Schlichting simulation. Furthermore, the jet simulated in case L2 did not reach a steady state,

nor is it guaranteed to do so. A time progression of the total magnetic field is shown in Figure 68. The early time shows that the field is relatively unperturbed by the flow as would be expected for very low magnetic Reynolds number flows. However, as time progresses, the field lines appear to bend inwards about four diameters downstream of the inlet. This bending of the field lines could eventually lead to magnetic reconnection in the axial direction, which would be relevant to the study of the physics of detachment. However, more study is needed to more conclusively examine these results.

E. Chapter Summary

In this chapter, the GKM-MHD code was used to simulate round jets subject to different applied magnetic fields. Schlichting's self-similar, axisymmetric jet is first simulated by the code and validated against the analytical solution. This steady state jet is then used as the input for simulations with a constant applied magnetic field and a spatially diverging magnetic field generated by a current loop. The results for the jet simulated with the constant applied magnetic field show excellent agreement with the theoretical predictions published by Davidson [32]. For the jet with the current loop, the results indicate that a transient vortical flow is perhaps generated by an initially outward pointing Lorentz force along with fluid entrainment from the far field boundaries. Additionally, aligned currents similar to the Davidson jet appear to direct the stretching of the jet profile, but could also be due to numerical errors introduced by the square boundaries. More work is needed to more conclusively examine the results.

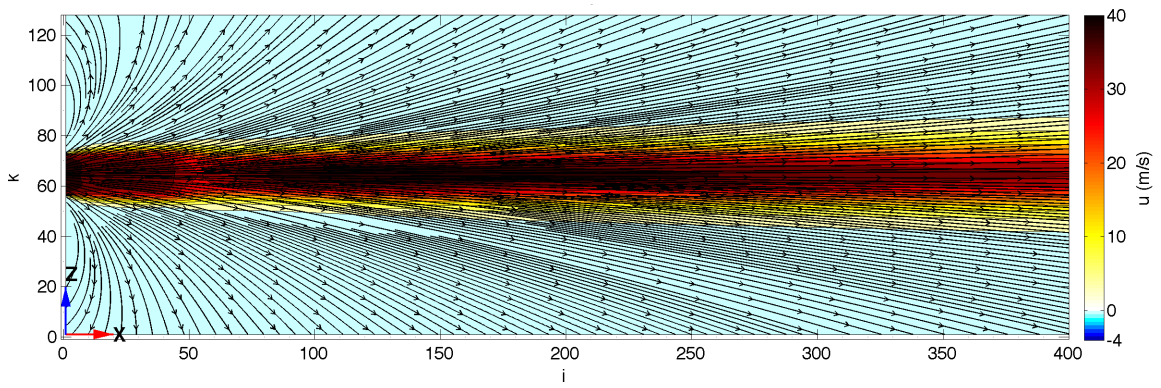

(a) B_xBz streamlines,$j = 64$, $t = 0.03s$.

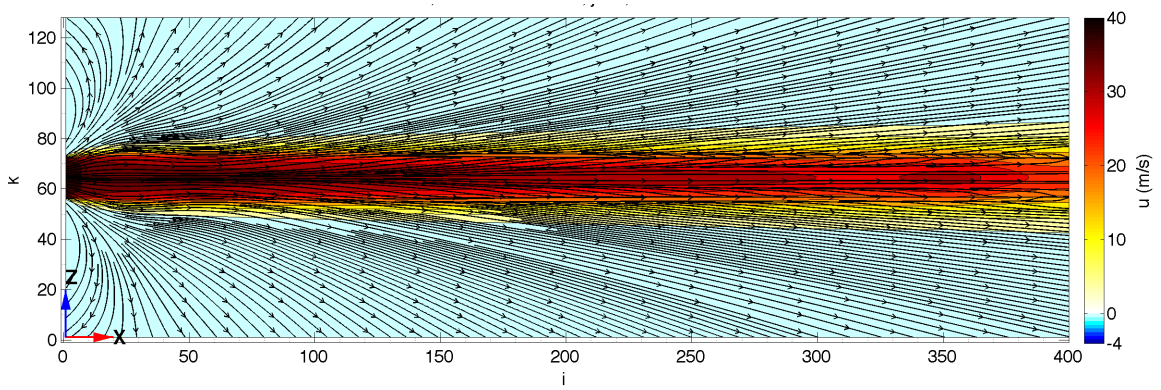

(b) B_xBz streamlines,$j = 64$, $t = 0.195s$.

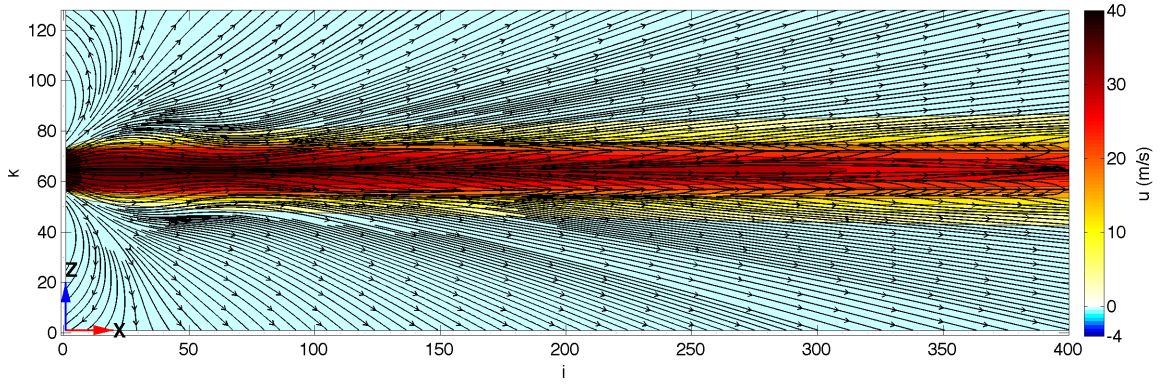

(c) B_xBz streamlines,$j = 64$, $t = 0.345s$.

Fig. 68. Magnetic field lines bending as time progresses for case L2.

CHAPTER VII

SUMMARY

This thesis investigates fundamental MHD flows by a new numerical tool based on the gas-kinetic method. The work presented here serves as an introductory step to developing a robust numerical flow solver capable of simulating magnetic nozzle flows and other plasmas that cannot be easily replicated in ground facilities.

The specific contributions of this thesis are the following:

1. A parametric map was created for the VX-200 rocket that outlines appropriate conditions required when using a fluid model for magnetic nozzle flows.

2. The previous gas-kinetic BGK continuum flow solver was extended to include resistive MHD physics by a splitting of hydrodynamic and magnetic terms.

3. The new GKM-MHD code was benchmarked against incompressible MHD Couette and Hartmann flows as well as a laminar round jet subject to a constant applied magnetic field.

4. New numerical experiments were performed and results obtained for a laminar round jet subject to the nonuniform magnetic field of a current loop.

The jet with the current loop provides an idealization of the VX-200 magnetic nozzle configuration examined in Chapter III, which was the original motivation for this work. The simulated jet flow is far from realizing the true characteristics of the VX-200 plume, but is an initial step toward the goal of studying detachment from a magnetic nozzle. The results of this work show great potential for the use of this code in studying complex plasma flows. However, there are several items to consider for future work to improve the current code. These improvements, listed in no particular

order, are the following:

- Adding the Hall physics as outlined in Chapter IV is one possible extension of this work. To benchmark this change, there exists a modified Hartmann problem for Hall physics given in Sutton [2].

- Currently the time integration scheme is only first-order accurate. Extending this to perhaps second-order Runge-Kutta could increase the stability of the scheme overall to allow for larger time step sizes.

- Second-order central difference schemes are known to have problems with oscillations when steep gradients are present in the flow field, such as from shocks. Though all of the flows tested in this thesis were weakly compressible, the main goal is to eventually have a working code for compressible MHD flows. Therefore, upwinding for the magnetic field terms should be added if finite differencing is still used.

- For a divergence-free initial magnetic field configuration, the current central difference scheme is guaranteed to conserve the divergence of the magnetic field as published by Tóth [53]. However, small numerical errors do accumulate for long iterations or for imperfectly specified fields. Therefore, clean up of the divergence of the magnetic field should also be added to continue to ensure physical results.

- Another liquid metal jet problem that is supported by experiments [54] exists in the literature. This flow is a free surface jet flowing into a non-uniform magnetic field and would serve as another good benchmark for the code.

- Extension of the code to multi-component flows will allow for solving the expansion to vacuum problem mentioned in the introduction. Additionally, this

could serve as the basis for a higher fidelity two-fluid plasma code.

- Work has recently been completed to extend the GKM code for a nonuniform grid. For incorporating this change into the current GKM-MHD code, care must be taken to use nonuniform central differencing. This change would allow more flexibility in the setup of the computational domain and also potentially reduce the computational resources required for large physical domains.

It is clear that significant advances in space propulsion technology are needed in order to achieve human spaceflight missions deep into space beyond the Earth. Plasma propulsion technology offers a promising route for achieving this goal but still has multiple technological and scientific challenges to overcome. The work of this thesis contributes a small part to reaching a much larger goal by expanding the capabilities for numerical simulations of magnetic nozzle flows.

REFERENCES

[1] R. G. Jahn, *Physics of Electric Propulsion*. New York: Dover Publications, Inc., 2006.

[2] G. P. Sutton and O. Biblarz, *Rocket Propulsion Elements*, 7th ed. New York: John Wiley & Sons, Inc., 2001.

[3] A. V. Arefiev and B. N. Breizman, "Theoretical components of the VASIMR plasma propulsion concept," *Physics of Plasmas*, vol. 11, no. 5, pp. 2942–2949, 2004.

[4] F. R. Chang-Diaz, J. P. Squire, T. Glover, A. J. Petro, E. A. Bering *et al.*, "The VASIMR engine: Project status and recent accomplishments," in *42nd Aerospace Sciences Meeting and Exhibit*, no. 2004-149, Reno, NV, January 2004.

[5] T. W. Glover, F. R. Chang-Diaz, J. P. Squire, V. P. Jacobson, D. G. Chavers *et al.*, "Principal VASIMR results and present objectives," in *AIP Conference Proceedings*, vol. 746, Albuquerque, NM, February 2005, pp. 976–982.

[6] J. P. Squire, F. R. Chang-Diaz, M. D. Carter, L. D. Cassady, W. J. Chancery *et al.*, "High power VASIMR experiments using deuterium, neon and argon," in *30th International Electric Propulsion Conference*, no. 2007-181, Florence, Italy, September 2007.

[7] A. V. Arefiev and B. N. Breizman, "Magnetohydrodynamic scenario of plasma detachment in a magnetic nozzle," *Physics of Plasmas*, vol. 12, no. 043504, 2005.

[8] E. Hooper, "Plasma detachment from a magnetic nozzle," *Journal of Propulsion and Power*, vol. 9, no. 5, pp. 757–763, 1993.

[9] D. A. Kaufman and D. G. Goodwin, "Plasma separation from magnetic field lines in a magnetic nozzle," in *31st Aerospace Sciences Meeting & Exhibit*, no. 93-0817, Reno, NV, January 1993.

[10] R. W. Moses, R. A. Gerwin, and K. F. Schoenberg, "Resistive plasma detachment in nozzle based coaxial thrusters," in *AIP Conference Proceedings*, vol. 246, Albuquerque, NM, January 1992, pp. 1293–1303.

[11] P. F. Schmit and N. J. Fisch, "Magnetic detachment and plume control in escaping magnetized plasma," *Journal of Plasma Physics*, vol. 75, no. 3, pp. 359–371, 2009.

[12] F. N. Gesto, B. D. Blackwell, C. Charles, and R. W. Boswell, "Ion detachment in the helicon double-layer thruster exhaust beam," *Journal of Propulsion and Power*, vol. 22, no. 1, pp. 24–30, 2006.

[13] A. V. Ilin, F. R. Chang Diaz, J. P. Squire, A. G. Tarditi, B. N. Breizman *et al.*, "Simulations of plasma detachment in VASIMR," in *40th AIAA Aerospace Sciences Meeting & Exhibit*, no. 2002-0346, Reno, NV, January 2002.

[14] K. Sankaran and K. A. Polzin, "Development of numerical tools for the investigation of plasma detachment from magnetic nozzles," in *38th AIAA Plasmadynamics and Lasers Conference*, no. 2007-4386, Miami, FL, June 2007.

[15] A. G. Tarditi and J. V. Shebalin, "Magnetic nozzle plasma exhaust simulation for the VASIMR advanced propulsion concept," in *28th International Electric Propulsion Conference*, Toulouse, France, March 2003.

[16] B. N. Breizman, M. R. Tushentsov, and A. V. Arefiev, "Magnetic nozzle and plasma detachment model for a steady-state flow," *Physics of Plasmas*, vol. 15,

no. 057103, 2008.

[17] W. Chancery, "Investigation of plasma detachment from a magnetic nozzle," Master's thesis, Auburn University, Auburn, AL, 2007.

[18] D. G. Chavers, C. Dobson, J. Jones, M. Lee, A. Martin *et al.*, "Status of magnetic nozzle and plasma detachment experiment," in *AIP Conference Proceedings*, vol. 813, Albuquerque, NM, January 2006, pp. 465–473.

[19] C. A. Deline, R. D. Bengtson, B. N. Breizman, M. R. Tushentsov, J. E. Jones *et al.*, "Plume detachment from a magnetic nozzle," *Physics of Plasmas*, vol. 16, no. 033502, 2009.

[20] M. D. West, C. Charles, and R. W. Boswell, "Testing a helicon double layer thruster immersed in a space-simulation chamber," *Journal of Propulsion and Power*, vol. 24, no. 1, pp. 134–141, 2008.

[21] C. Sovinec, A. Glasser, T. A. Gianakon, D. Barnes, R. Nebel *et al.*, "Nonlinear magnetohydrodynamics simulation using high-order finite elements," *Journal of Computational Physics*, vol. 195, no. 1, pp. 355–386, 2004.

[22] K. Xu, "A gas-kinetic BGK scheme for the Navier-Stokes equations and its connection with artificial dissipation and godunov method," *Journal of Computational Physics*, vol. 171, no. 1, pp. 289–335, 2001.

[23] J. Kerimo and S. S. Girimaji, "Boltzmann-BGK approach to simulating weakly compressible 3D turbulence: comparison between lattice boltzmann and gas kinetic methods," *Journal of Turbulence*, vol. 8, no. 46, 2007.

[24] H. Tang, K. Xu, and C. Cai, "Gas-kinetic BGK scheme for three dimensional magnetohydrodynamics," *Numer. Math. Theor. Meth. Appl.*, vol. 3, no. 4, pp.

387–404, 2010.

[25] K. Xu, "Gas-kinetic theory based flux splitting method for ideal magnetohydrodynamics," ICASE, NASA Langley Research Center, Hampton, VA, Tech. Rep. 98-53, November 1998.

[26] B. M. Riley, J. C. Richard, and S. S. Girimaji, "Assessment of magnetohydrodynamic lattice boltzmann schemes in turbulence and rectangular jets," *International Journal of Modern Physics C*, vol. 19, no. 8, pp. 1211–1220, 2008.

[27] B. M. Riley, S. S. Girimaji, J. C. Richard, and K. Lee, "Magnetic field effects on axis-switching and instabilities in rectangular plasma jets," *Flow, Turbulence and Combustion*, vol. 82, no. 3, pp. 375–390, 2009.

[28] C.-L. Tian, "An extension of gas-kinetic BGK Navier-Stokes scheme to multidimensional astrophysical magnetohydrodynamics," October 2010, preprint submitted to Journal of Computational Physics.

[29] K. Xu, "BGK-based scheme for multicomponent flow calculations," *Journal of Computational Physics*, vol. 134, pp. 122–133, 1997.

[30] J. V. Shebalin, "Pseudospectral simulation of compressible turbulence using logorithmic variables," ICASE, NASA Langley Research Center, Hampton, VA, Tech. Rep. 92-61, March 1993.

[31] F. G. Fuchs, S. Mishra, and N. H. Risebro, "Splitting based finite volume schemes for ideal MHD equations," *Journal of Computational Physics*, vol. 228, pp. 641–660, 2009.

[32] P. Davidson, "Magnetic damping of jets and vortices," *Journal of Fluid Mechanics*, vol. 299, pp. 153–185, 1995.

[33] F. F. Chen, *Plasma Physics and Controlled Fusion*, 2nd ed. New York: Springer, 2006.

[34] C. Birdsall and A. Langdon, *Plasma Physics via Computer Simulation*. Philadelphia: Institute of Physics Publishing, 1991.

[35] P. M. Bellan, *Fundamentals of Plasma Physics*. New York: Cambridge University Press, 2006.

[36] A. R. Kantrowitz and H. E. Petschek, "An introductory discussion of magnetohydrodynamics," in *Magnetohydrodynamics*, R. K. M. Landshoff, Ed. Palo Alto, CA: Stanford University Press, 1957.

[37] E. A. Bering, B. Longmier, J. P. Squire, T. W. Glover, L. D. Cassady *et al.*, "Performance measurements and technology demonstration of the VASIMR VX-200," in *AIAA Space 2010 Conference and Exposition*, no. 2010-8673, Anaheim, CA, August 2010.

[38] D. B. Araya, S. S. Girimaji, M. D. Carter, and C. S. Olsen, "Parameterization of magnetic nozzle flow physics for an in-space propulsion application," in *42nd AIAA Plasmadynamics and Lasers Conference in conjunciton with the 18th International Conference on MHD Energy Conversion*, no. 2011-4010, Honolulu, Hawaii, June 2011.

[39] G. Schmidt, *Physics of High Temperature Plasmas*, 2nd ed. New York: Academic Press, 1979.

[40] G. W. Sutton and A. Sherman, *Engineering Magnetohydrodynamics*. New York: Dover Publications, Inc., 2006.

[41] P. J. Dellar, "Lattice kinetic schemes for magnetohydrodynamics," *Journal of Computational Physics*, vol. 179, pp. 95–126, 2002.

[42] J. D. Anderson, *Fundamentals of Aerodynamics*, 4th ed. New York: McGraw-Hill, 2007.

[43] P. A. Davidson, *An Introduction to Magnetohydrodynamics*. New York: Cambridge University Press, 2001.

[44] H. Schlichting and K. Gersten, *Boundary-Layer Theory*, 8th ed. New York: Springer, 2000.

[45] D. Auerbach, "Experiments on the trajectory and circulation of the starting vortex," *Journal of Fluid Mechanics*, vol. 183, pp. 185–198, 1987.

[46] P. C. Babu and K. Mahesh, "Upstream entrainment in numerical simulations of spatially evolving round jets," *Physics of Fluids*, vol. 16, no. 10, pp. 3699–3705, 2004.

[47] X.-Y. Luo, A. Ying, and M. Abdou, "Numerical study of MHD effect on liquid metal free jet under complex magnetic fields," *Fusion Engineering and Design*, vol. 81, pp. 1451–1458, 2006.

[48] I. Mandre. (2011) Octave scripts for the magnetic field due to a current loop. [Online]. Available: http://www.mare.ee/indrek/octave/

[49] J. C. Simpson, J. E. Lane, C. D. Immer, and R. C. Youngquist, "Simple analytic expressions for the magnetic field of a circular current loop," Dynacs, Inc., Kennedy Space Center, FL, Tech. Rep. NAS10-98001, February 2001.

[50] R. Samulyak, J. Du, J. Glimm, and Z. Xu, "A numerical algorithm for MHD of free surface flows at low magnetic reynolds numbers," *Journal of Computational Physics*, vol. 226, no. 2, pp. 1532–1549, October 2007.

[51] J. Kane, M. Rhodes, G. Loosmore, J. Latkowski, J. Koning *et al.*, "Modeling of the LIFE minichamber Xe theta pinch experiment," in *High Power Lasers for Fusion Research*, A. A. Awwal, A. M. Dunne, H. Azechi, and B. E. Kruschwitz, Eds., vol. 7916, no. 791605, San Francisco, CA, January 2011.

[52] M. R. LaPointe, "Primary propulsion for piloted deep space exploration: NASA institute for advanced concepts phase I final report," Horizon Technologies Development Group, Cleveland, OH, Tech. Rep. NIAC Grant 07600-022, December 1999.

[53] G. Toth, "The $\nabla \cdot \mathbf{B} = 0$ constraint in shock-capturing magnetohydrodynamics codes," *Journal of Computational Physics*, vol. 161, pp. 605–652, 2000.

[54] S. Oshima, R. Yamane, Y. Mochimaru, and T. Matsuoka, "The shape of a liquid metal jet under a non-uniform magnetic field," *JSME*, vol. 30, no. 261, pp. 437–448, 1987.

VITA

Daniel Borsodi Araya has lived in Texas all of his life. He began his undergraduate studies at Texas A&M University in August 2003 and received his Bachelor of Science degree in Aerospace Engineering on December 2008. From February until June of 2009 he was a volunteer teacher of english and physics in a rural village outside of Arusha, Tanzania. He began his graduate studies at Texas A&M University in August of 2009 under the advisement of Dr. Sharath Girimaji. This thesis is the culmination of his graduate research and has been submitted in partial fulfillment of the requirements for a Master of Science degree in Aerospace Engineering. Mr. Araya worked at the NASA Johnson Space Center as a co-operative education student during his undergraduate and graduate years. His research interests are in the areas of fluid dynamics, plasma physics, and propulsion. In September 2011 he will continue toward earning his Ph.D. at the California Institute of Technology.

Contact Information: Dr. Sharath Girimaji, Department of Aerospace Engineering, Texas A&M University, College Station, TX 77843-3141.